Electrical Properties of Metal-Molecular Nanoparticle Networks: Modeling and Experiment

by

Po Zhang
B. Sc., University of Science and Technology of China, 2012

A Thesis Submitted in Partial Fulfillment
of the Requirements for the Degree of

MASTER OF APPLIED SCIENCE

in the Department of Electrical and Computer Engineering

Supervisory Committee

Electrical Properties of Metal-Molecular Nanoparticle Networks: Modeling and Experiment

by

Po Zhang
B. Sc., University of Science and Technology of China, 2012

Supervisory Committee

Dr. Chris Papadopoulos, (Department of Electrical and Computer Engineering)
Supervisor

Dr. Mihai Sima, (Department of Electrical and Computer Engineering)
Departmental Member

Abstract

Supervisory Committee

Dr. Chris Papadopoulos, (Department of Electrical and Computer Engineering)
Supervisor

Dr. Mihai Sima, (Department of Electrical and Computer Engineering)
Departmental Member

The electrical properties of metal-molecular nanoparticle networks are studied both theoretically and experimentally. Benzenedithiol-aluminum cluster linear chains, Y-shaped and H-shaped networks are modeled with semi-empirical methods to study the electronic properties of such structures. The HOMO (highest occupied molecular orbital)-LUMO (lowest unoccupied molecular orbital) gaps of the benzenedithiol-Al cluster networks decrease several eV compared to the isolated benzenedithiol molecule. Frontier energy levels become more closely spaced as the size of the molecular networks increase, accompanied with an increased HOMO energy and decreased LUMO energy, indicating a decreased energy barrier to electron transport. Delocalized spatial distribution of the frontier orbitals indicates a high probability for electron transmission and corresponds well with peaks near the HOMO-LUMO gap in the electronic density of states.

Self-assembled molecular networks consisting of dithiol/thiol molecules and 30 nm colloidal gold nanoparticles are fabricated with a solution-based method. Electrical measurements performed on these nanostructures show a typically linear current-voltage characteristic while nonlinear *I-V* curves are also observed for networks built of benzenedithiol or hexane/octanethiol molecules. Further analysis with atomic force

microscopy shows that the network's conductance is determined by the molecule's conductivity and network dimensions. Circuit model consisting of networked molecular resistors is applied to study the interconnections between the particles within the network and the simulated values of the network's conductance is consistent with the measured values.

Theoretical and experimental study on the electrical properties of metal-molecular nanoparticle networks reveals the influence of molecules and metallic particles on determining the network's conductivity. Such self-assembled networks can be used to implement several circuit elements, such as resistors, diodes, etc., and more complicated computation components such as nanocells, memristors, etc. The electrical properties of the networks can be tuned by proper choice of molecules, metallic particles and network geometry making them promising for future molecular electronic circuits.

Table of Contents

List of Tables

List of Figures

Acknowledgments

First, I would like to express my greatest gratitude to Dr. Chris Papadopoulos for his guidance and help through my entire program. Without his help, it would not be possible to make this research as exciting and rewarding as it is.

I would also thank Dr. Mihai Sima for the time and effort spent being a member of my supervisory committee.

I would like to thank my fellow lab member Anusha Venkataraman for her assistance with research tasks and also both Anusha, Raju Sapkota, and Teng Hu for their friendship and support in the lab.

Above all, I am greatly thankful to my parents for their constant support and encouragement during my graduate program.

Chapter 1 Introduction

Nanotechnology concerns the design, characterization and production of structures, systems and devices roughly from 1 nm to 100 nm [1, 2] in extent. The idea of manipulating materials at the nanoscale was first discussed by the celebrated physicist and Nobel Laureate Richard Feynman in his talk entitled “There is plenty of room at the bottom” at the annual meeting of the American Physical Society in 1959. In his talk, he laid out several consequences of measuring and manipulating materials at near-atomic scales and pointed out the incredible difference, such as the quantum phenomenon in devices, between the nanoscale world and the macroscopic world around us.

During the last half century, the rapid development of nanotechnology was spurred by the improved ability to detect and control matters at the nanoscale. The scanning tunnelling microscope (STM) [3], invented Heine Rohrer in 1981, largely improves the ability of imaging and manipulation of nanoscale structures. The invention of the atomic Force microscope (AFM) [4] addressed STM’s limitation of imaging only conducting materials and could be used onto insulated materials. The ability to image and manipulate atomic scale structures stimulated the invention and development of novel methods of detecting and controlling the fabrication of devices at the nanoscale. Photolithography [5] has prompted the exponential growth in the semiconductor industry for over 50 years.

Different from top-down methods such as photolithography, bottom-up assembly methods can make complex nanoscale structures from their constituent elements directly.

Examples include self-assembled molecular monolayers [6] where the self-assembly process happens when attaching molecule onto surfaces, synthesis of nanowires [7] and quantum dots [8], and the use of DNA in making complex nanoscale systems [9].

Today nanotechnology is a group of diverse technologies that is revolutionizing technological advancements and brings physicists, chemists, biologists and engineers together to build extremely novel and advanced structures for applications.

1.1 Origins of Nanoelectronics

Silicon has been the primary material in manufacturing electronics devices for more than 50 years, spurred by the invention of the first bipolar transistor by Bardeen and Brattain in 1947 [10] (Figure 1.1 (a)), which marked the beginning of modern electronics era, the first integrated circuit (IC) was made by Kilby in 1958 [11], which simply consisted of one bipolar transistor, three resistors, and one capacitor (Figure 1.1 (b)). In 1959, Noyce reported the first monolithic IC with all devices fabricated on a single semiconductor substrate using oxide isolation and aluminum metallization [12] (Figure 1.1 (c)). In 1960, Kahng and Atalla fabricated the first enhanced mode metal oxide semiconductor field effect transistor (MOSFET) with a 25 μm silicon channel length and 1000 Å silicon oxide gate thickness [13]. The complementary metal oxide semiconductor (CMOS) technique largely increased the complexity of IC with its ease to implement logic gates and is still the main standard technique in integrated circuits. The continuing improvement of the circuits' performance can be achieved by scaling down the channel length of MOSFETs and, as predicted by the famous Moore's law [14, 15, 16], the

density of components in integrated circuits are doubled every 18 months, as illustrated in Figure 1.2 (a). Nowadays, extremely advanced integrated circuits can be designed and fabricated by engineers and scientists. The CPUs running on a personal computer are extremely complicated with memories, peripheral interfaces and other devices embedded on chip and can perform calculation at frequencies of several GHz.

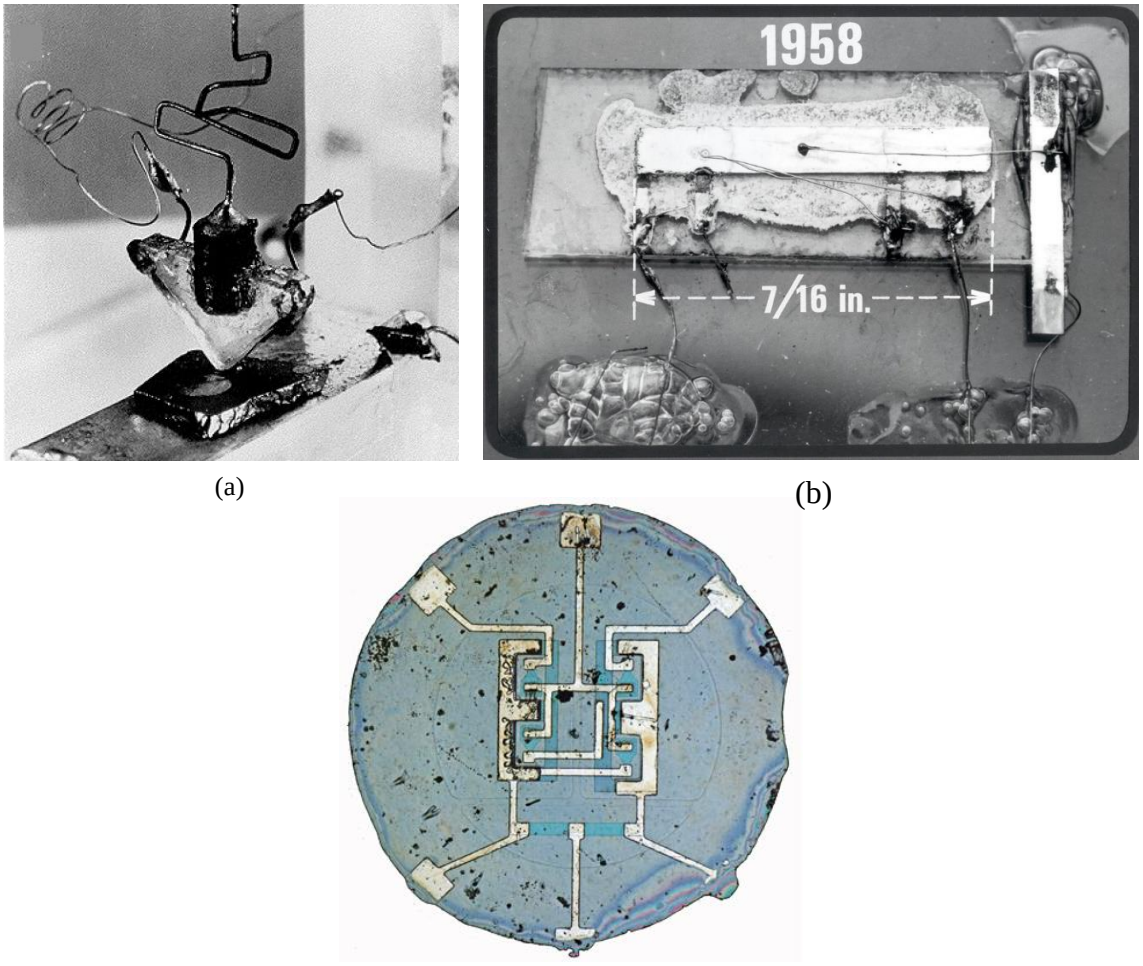

(a) (b)

(c)

Figure 1.1 (a) First bipolar transistor by Bardeen and Brattain (Bell Labs); (b) first integrated circuit by Kilby (Texas Instruments); (c) first monolithic integrated circuit by Noyce (Fairchild Semiconductor). All figures adapted from Ref. 17

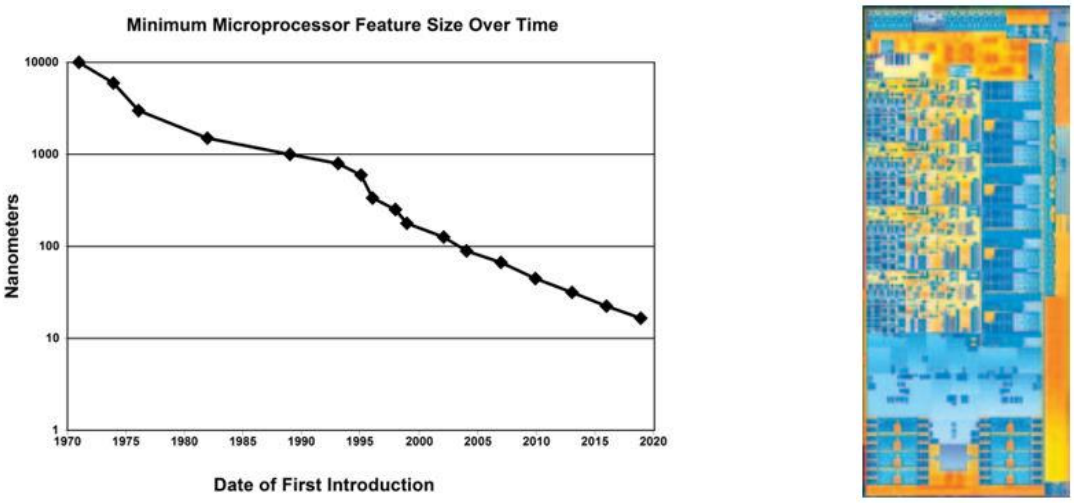

(a) (b)

Figure 1.2 (a) Feature size of transistors on IC versus time (adapted from Tech Pro Communications); (b) 3rd generation Intel Core processor consisting of 1.4 billion transistors manufactured with 22 nm technology (adapted from Intel).

However, it is widely assumed that the miniaturization progress of integrated circuits will soon reach its physical limits perhaps within 10 years. Conventional lithography is approaching its resolution limit to fabricate smaller components [18], and, especially, below the 5 nm scale, very short channel MOSFETs are unable to turn on or off properly [19].

Inspired by the demand to continue the miniaturization trend of electronic devices into the deep nanometer scale, researchers have investigated and proposed several novel nanometer-scale electronic (nanoelectronic) devices as alternatives to or in support of the transistors in current ultra-dense IC circuitry to continue the miniaturization trend of Moore's Law. Unlike today's field effect transistors, these new devices can take advantage of quantum effects that emerge at the nanometer scale, which may lead to very

different operating principles from conventional integrated circuits. One example of a quantum effect nanoscale device is the resonant tunneling transistor, which makes use of the electron tunneling behaviour at the nanoscale [20] (Figure 1.3 (a)). The operation of resonant tunneling transistors is achieved by adjusting the energy of the quantum states in the potential well relative to the bands in the source and drain. The quantum well in the resonant tunneling transistor is turned on when the states inside the well are aligned with the energies of the source, controlled by the bias potential. And then current is able to flow through the island and to the drain. As another example, a quantum dot confines a collection of free electrons in a small region of semiconductor material, which can be coupled to the nearby macroscopic areas via tunnel barriers [21]. One common type of quantum dot is created with patterned metal electrodes on a surface of a two-dimensional electron gas (2DEG) heterostructure such as AlGaAs/GaAs, as shown in Figure 1.3 (b). By applying proper bias on the electrodes, the underlying electron gas is depleted and a small region of electrons is confined in the center of the structure, which can be used for devices such as single electron transistors or memory [22, 23].

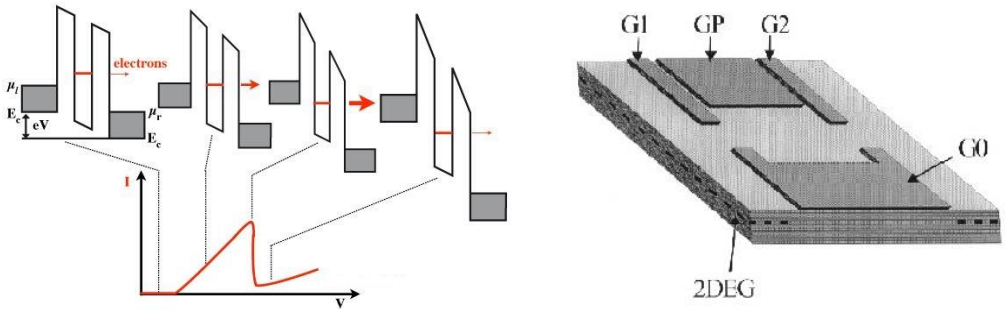

(a) (b)

Figure 1.3 (a) Operating principle and *I-V* curve for a resonant tunneling device (adapted from Semiconductor Device Group of University of Glasgow); (b) Schematic of a quantum dot consisting of a GaAs heterostructure with a 2DEG near the surface (adapted from Ref. 21).

Molecular electronics is a relatively new category of nanoelectronics. In molecular electronics, molecules can act as individual nanometer-scale components in circuitry and this idea radically changes the operating principles and the materials used for electronic devices. Molecules and their nanoscale structures can be made in large numbers cheaply and easily and the great variety in organic chemistry provides many options of molecules for designing and constructing nanoscale devices and networks.

1.2 Molecular Electronics

The idea of single-molecule electronics was first proposed by Aviram and Ratner in their work of a kind of electron donor acceptor molecule [24] that could behave as a molecular rectifier in 1974 [25]. The molecule in Figure 1.4 (a) consists of a modified donor (tetrathiofulvalene) and acceptor (tetracyanoquinodimethane) interconnected by a weakly-coupled bridge would behave as a conductor when applied a bias above a critical threshold. This work by Aviram and Ratner is a landmark proposal for individual molecular electronic devices.

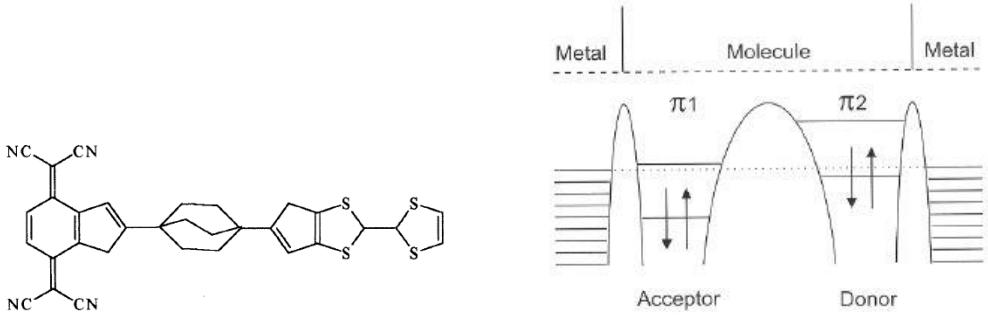

(a) (b)

Figure 1.4 (a) The proposed single-molecule rectifier by Aviram and Ratner; (b) Energy versus distance of the device. (adapted from Ref. 25).

Early experimental work demonstrating an operating molecular electronic device was made by McGinness, Corry and Proctor, also in 1974 [26]: The conduction of biological melanin oligomers was measured and showed switching behaviour, which occurred reversibly at threshold bias as two or three orders of magnitude higher than conventional semiconductor thin films. It was also the first work that reported the observation of negative differential resistance in molecules, which was later observed by J. Chen, J.M. Tour, and their coworkers [27], as shown in Figure 1.5. In the 1970s, Forrest L. Carter proposed the idea of computing at the molecular level, using oligomer or polyacetylene molecular wires, various types of molecular switches, and tunneling devices [28, 29].

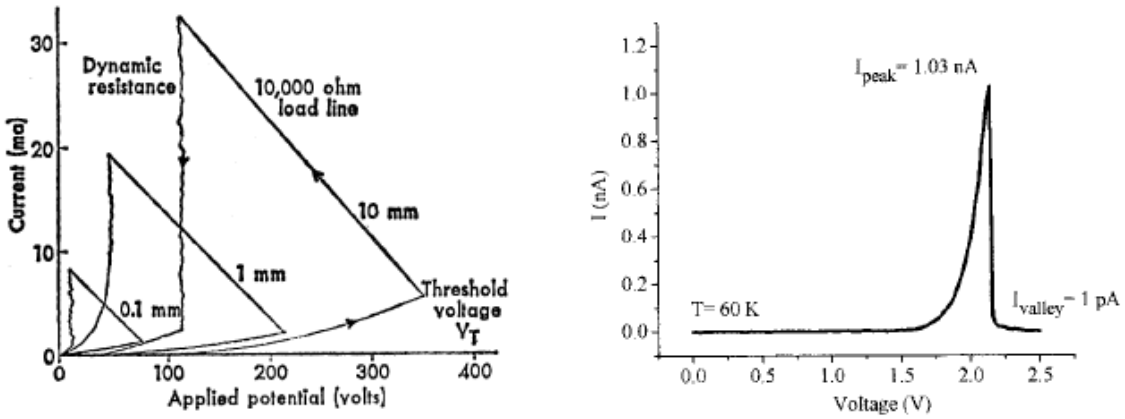

(a) (b)

Figure 1.5 Current-voltage characteristics of (a) melanin of various sample thicknesses (adapted from Ref. 26); (b) Au-(2` -amino-4-ethynylphenyl-4` -ethynylphenyl-5` -nitro-1-benzenethiolate)-Au device at 60 K (adapted from Ref. 27).

The development in molecular electronics couldn't proceed without the invention of efficient tools for observing and characterizing nanoscale structures. The use of STM greatly improved scientists' ability to observe and control structures down to the atomic scale, as shown in Figure 1.6 (a). AFM is another important tool for imaging nanoscale

structures and allows one to image both conducting and insulating materials by detecting the force exerted on the tip from the sample's surface. Modern AFM typically uses an optical deflection scheme to monitor the bending force on a cantilever, as shown in Figure 1.6 (b).

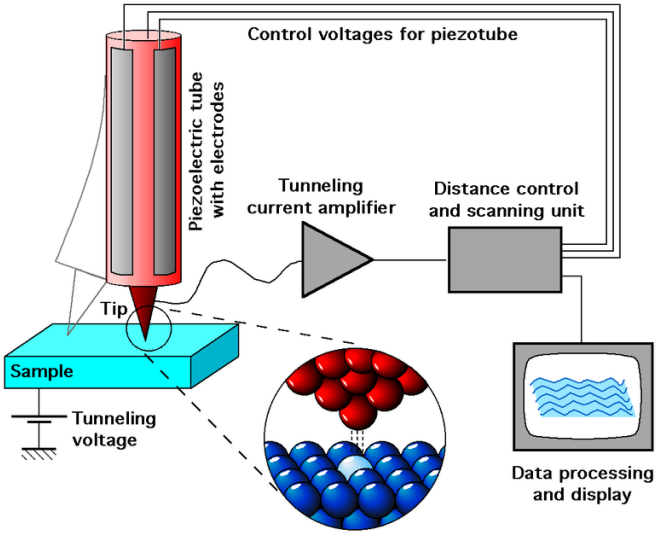

(a)

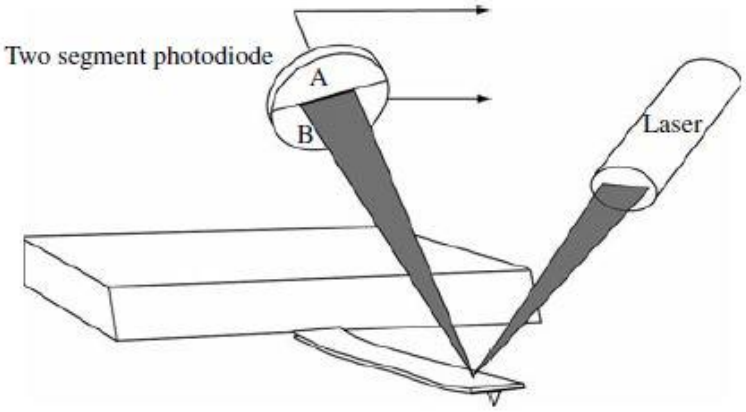

(b)

Figure 1.6 (a) Schematic view of STM (adapted from IAP/TU Wien STM Gallery); (b) Schematic of optical deflection scheme of AFM (adapted from Ref. 2).

For understanding electron transport through molecules, Landauer theory [30] provides a general framework for the calculation of electronic current through molecules that are coupled to quasi-one-dimensional electrodes, which relates the electronic current with the transmission probability for an electron elastically scattering through the molecular junction.

$$I = \frac{2e}{\hbar}\int \frac{dE}{2\pi} T(E)[f_L(E) - f_R(E)] \quad (1.1)$$

where I is current, e is the elementary charge, ħ is the reduced Plank constant, $T(E)$ is the transmission probability, and $f_L(E)$ and $f_R(E)$ are the Fermi functions of the left and right leads. However, more specifically inelastic scattering should be taken into consideration and in many situations it plays an important role in determining molecule's electron transport properties [31]. For example, if a saturated molecule has thermally activated charge transport, higher temperature will increase its conductivity, while for conjugated molecules thermal energy may not increase the conductance as much if it is mainly due to direct tunneling. Generally the conduction mechanisms in molecules usually fall into two distinct categories, based on whether thermal activation is involved: (i) thermionic or hopping conduction which is temperature-dependent, and (ii) Fowler-Nordheim or direct tunneling which is not temperature-dependent [32]:

Thermionic emission	$J \sim T^2 \exp(-\frac{\Phi - q\sqrt{qV/4\pi\varepsilon d}}{kT})$	(1.2)
Hopping conduction	$J \sim V \exp(-\frac{\Phi}{kT})$	(1.3)
Fowler-Nordheim tunneling	$J \sim V^2 \exp(-\frac{4d\sqrt{2m}\Phi^{3/2}}{3q\hbar V})$	(1.4)
Direct tunneling	$J \sim V \exp(-\frac{2d}{\hbar}\sqrt{2m\Phi})$	(1.5)

where J is the tunneling current density, V is the applied bias, Φ is the barrier height, d is the barrier width, m is the electron mass, q is the charge, T is the temperature, k is the Boltzmann constant, and ε is the vacuum permittivity. The exponential decay and temperature independence of saturated molecules suggest that electron tunnelling as the conduction mechanism while for conjugated molecules off-resonance tunneling or hopping is believed to be the conduction mechanism for conjugated molecules [33]

To test the conductivity of molecules, usually molecular electronic devices require at least two contacts to the molecules and thus how to bridge molecules between metal electrodes, i.e, to form metal-molecular junctions has been at the heart of research in molecular electronics. One common method to attach molecules to metal electrodes is to use the S-Au bond to connect to a gold surface. The advantage of this method is that organic systems with thiol end groups can form self-assembled attachment onto the gold electrodes. Based on this property, thiol\dithiol molecules have attracted great interests in the area and is one of the most extensively studied molecular electronic systems, both experimentally and theoretically.

Conducting tip AFM is one straightforward way to make the metal-to-molecule contact required for the study of molecular electronic devices. Engelkes, Beebe and Frisbie studied the length-dependent electronic transport property of alkanethiol and alkanedithiols using this conducting tip AFM method in their work [34], as shown in Figure 1.7. The AFM tips were coated with Au, Pt or Ag and the molecular junctions were formed between the metal-coated conducting tip and self-assembled monolayers

(SAMs) of alkanethiol or alkanedithiol molecules on polycrystalline Au, Pt or Ag substrates. The SAMs were formed by immersing the substrates into solutions of molecules in ethanol for a few hours and the formation of the molecular junctions was formed between the metal-coated AFM tip and the SAM on substrate.

Bias was applied to the tip measure the current-voltage characteristics of the nanoscale junctions. Current-voltage traces showed an exponential attenuation with the length of the molecule according to

$$R = R_0 \exp(\beta n) \qquad (1.6)$$

where R_0 was the effective contact resistance, n was the number of repeat carbon units, and β was the attenuation factor. The length-dependent attenuation factor, β, was measured to be approximately 1.1 per carbon unit and was independent of the applied bias and the type of electrodes, as illustrated in Figure 1.8 (a)(b).

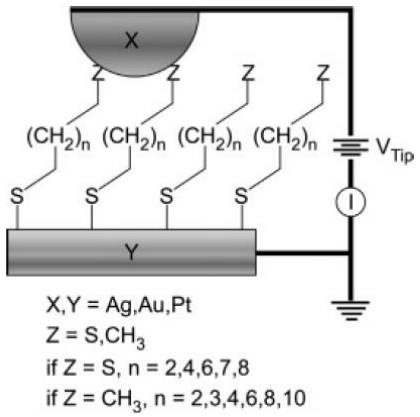

Figure 1.7 Schematic of molecular tunnel junction formed between metal-coated AFM tip and SAM of alkanetihiol or alkanedithiol molecules

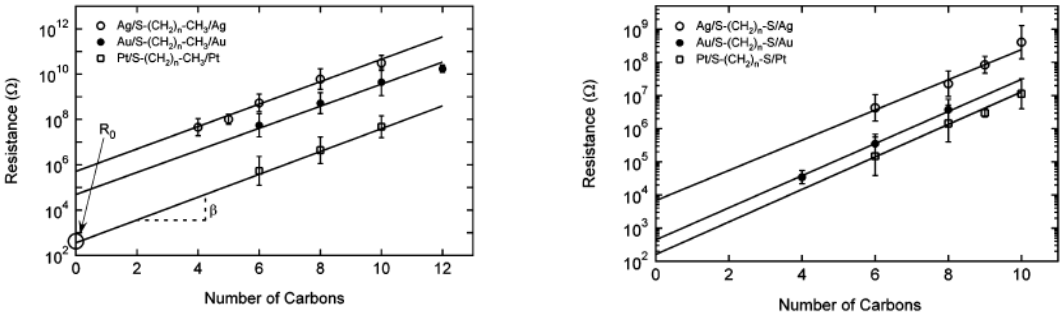

(a) (b)

Figure 1.8 Resistances versus molecule lengths of (a) alkanethiols and (b) alkanedithiols of the nanoscopic junctions (adapted from Ref. 34).

Another method of making metal-to-molecule contacts onto self-assembled monolayers is to deposit a thin film of metal onto thiolate SAM to make a sandwich geometry for the molecular junction, as reported in Wohlfart and his coworkers' work [35]. Here they demonstrated the selective deposition of thin gold films onto self-assembled dithiol molecules formed using the organometallic chemical vapor deposition (OMCVD) technique. SAM of octanedithiol was first formed on mica sheet coated with gold film. The gold vapor from a gold precursor would be only bound to the exposed thiol groups hence the deposited gold films were only formed on the areas covered by the octanedithiol SAMs. AFM images in Figure 1.9 showed that the thiol functionalized surfaces were covered with gold clusters deposited selectively via OMCVD while the other areas were approximate 10 nm lower in height.

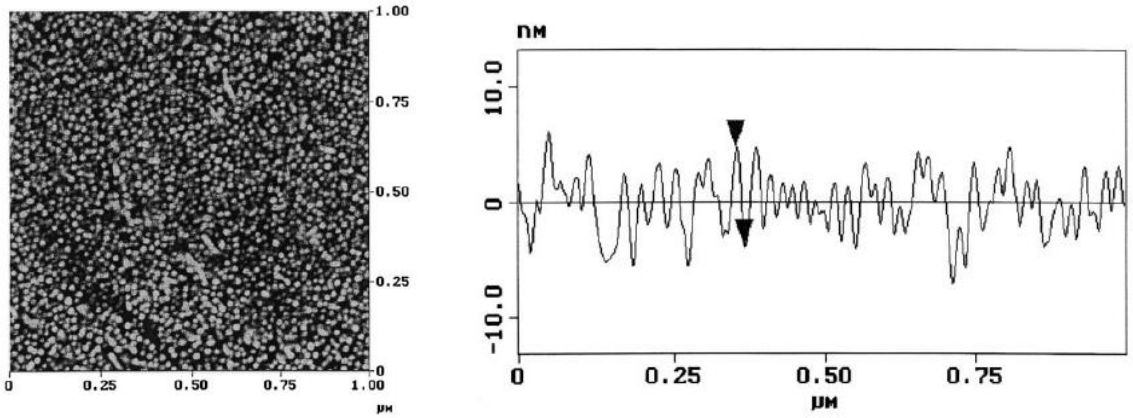

(a) (b)

Figure 1.9 (a) Surface topology of gold substrate covered with dithiol SAM and gold clusters deposited on top. The white dots represent deposited gold clusters; (b) AFM scan plot showing that the clusters are typically 20 nm in diameter and 10 nm in heights (adapted from Ref. 35).

The invention of the break junction technique is another advancement in studying the properties of single molecules bridged between metal electrodes. In the work by Tour and his coworkers [36], they gave an explicit description of their mechanically controllable break junction (MCB) technique and investigated the electrical transport property of a metal/benzenedithiol/metal junction. Figure 1.10 shows the schematic of the MCB system, which consisted of the bending beam, counter supports, notched gold wire, glue contacts, piezoelement and glass tube that contained the benzenedithiol solution. The notched metal wire was connected onto the substrate and bent gradually. After it was fractured, an adjustable tunneling gap could be established.

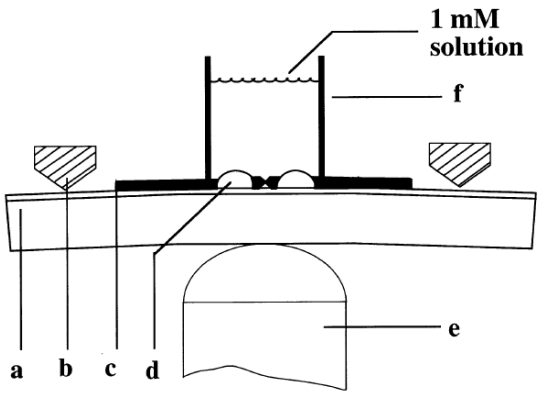

Figure 1.10 Schematic of the mechanically controllable break junction system. (a) The bending beam; (b) the counter support; (c) the notched gold wire; (d) the glue contacts; (e) the piezoelement; (f) the glass tube filled with solution (adapted from Ref. 36).

The benzenedithiol molecules were adsorbed onto the two facing gold electrodes formed by the break junction, forming a self-assembled monolayer nearly perpendicular to the surface of the gold electrodes. Figure 1.11 presents the process of making the metal/benzenedithiol/metal junction. The typical current-voltage characteristics and conductance are shown in Figure 1.12.

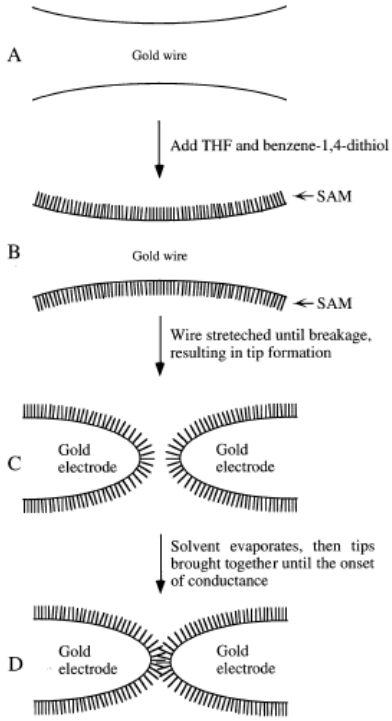

Figure 1.11 The process of forming the metal/benzenedithiol/metal junction. (a) The intact gold wire prior breaking the tip; (b) benzenedithiol solution was added and a SAM formed on the gold wire surface; (c) gold was mechanically broken in solution; (d) after the solvent evaporated, gold contacts were moved together slowly until the junction was measured conducting. Step (c) and (d) could be performed repetitively in the process (adapted from Ref. 36).

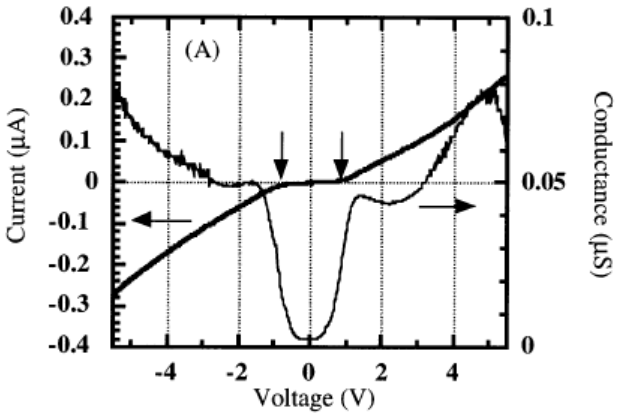

Figure 1.12 Typical current-voltage characteristics showed a plateau gap of 0.7 V and conductance plot presented a step-like character (adapted from Ref. 36).

Using metal nanoparticles is an alternative to the bulk metal electrodes in the metal-molecular junctions. In Ref. 37, Kober, Gotesman and Naaman reported a hybrid device consisting of gold nanoparticles covered with alkanedithiol molecules with different lengths. In the fabrication process, the gold nanoparticles were first mixed with the alkanedithiols, respectively, and then the hybrid mixture was deposited in the gap between two gold electrodes on silicon dioxide substrate, as shown in Figure 1.13. Conductance was measured to be length dependent, similar to what was reported in Ref. 34.

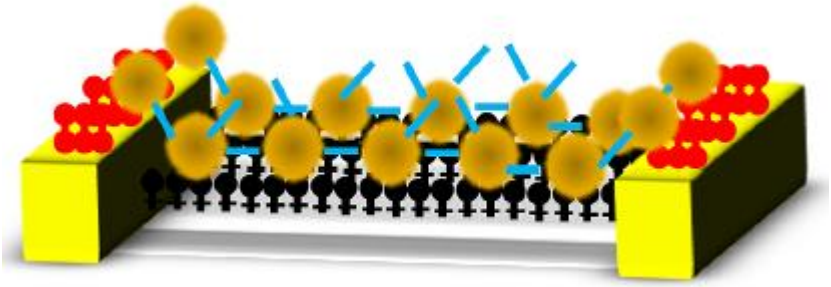

Figure 1.13 Schematic of device coated with the hybrid gold nanoparticle-organic molecule film. The gold electrodes and the gap were pre-covered with hexanedithiol and mercaptopropyltrimethoxysilane to yield good gold nanoparticle adhesion (adapted from Ref. 37).

Another approach to forming nanoparticle molecular junctions is to make small clusters of nanoparticles connected by molecules [38, 39]. Bar-Joseph and his coworkers' method was based on synthesis of a dimer structure made of two colloidal gold nanoparticles bridged by a dithiol organic molecule and then the nanoparticle dimer was trapped between two metal electrodes in order to measure the electrical conduction of the dimeric molecular junction, as illustrated in Figure 1.14 (a). The fabrication was performed in

solution and, if more than one molecule were bonded to a colloidal particle, trimers, tetramers and other oligomers could also be formed. To ensure that most of the colloidal gold particles were bridged by an individual dithiol molecule, the concentrations and the ratios of the colloidal particles and the dithiol molecules needed to be well designed and controlled precisely. Figure 1.14 (b) presents transmission electron microscope images of dimers synthesized in this manner. The gap between colloidal particles could be observed and the size was comparable with the size of the dithiol molecule.

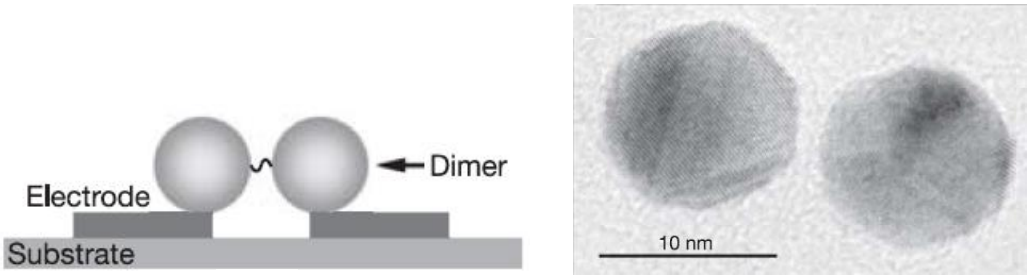

(a) (b)

Figure 1.14 (a) Schematic of colloidal dimeric device; (b) TEM of colloidal gold particle dimer connected by a benzenedithiol molecule (adapted from Ref. 38).

1.3 Overview of Thesis

Motivated by the previous work on metal/molecule/metal junctions, this work studied nanostructure networks made of metal nanoparticles and dithiol molecules, both theoretically and experimentally. Such structures have potential for active and passive components (resistors, diodes, transistors, etc.) of electronic circuits, building molecular-based circuitry at very small scales.

Chapter 2 describes modeling work on aluminum nanocluster-dithiol molecule nanoscopic systems using semi-empirical simulation methods. The size of the metal

cluster is comparable to the size of the organic molecule, which would avoid the effort to calculate the microscopic molecular junction with the macroscopic metallic electrodes separately. Thus, in this way, the whole hybrid metal-molecular system can be treated as a “supramolecule”. The semi-empirical simulation package VAMP with Austin Model 1 and Hartree-Fock methods are used in our calculation on the junctions and networks built of interconnected dithiol molecules and Al clusters. The relaxed geometries of the molecules and clusters are consistent with the work reported by other groups. The change in the electronic properties after the introduction of Al nanoparticle clusters is manifested in the decrease in the HOMO (highest occupied molecular orbital)-LUMO (lowest unoccupied molecular orbital) gaps of the molecular systems. The well delocalized molecular orbitals near the HOMO-LUMO gap of the benzenedithiol molecular networks are indicators of the good electron transport characteristic. Switching elements and molecular-scale circuits based on Y- and H-shaped networks are proposed in analogy to electron waveguide devices.

Chapter 3 concerns experimentally implementing interconnected dithiol /thiol molecule-metal cluster junctions in the form of self-assembled gold nanoparticle molecular networks. This work is motivated by previous work on the close-packed films of gold nanoparticles interconnected by dithiol organic molecules and oligomers of interconnected gold nanoparticles. The structures investigated fall in between the two extremes in terms of the size of the molecular network, which are much larger than the gold particle dimers in microscopic scale but still much smaller than the bulk films composed of many molecules. So the number of molecules studied is between gold

particle dimers, which studies one single (or a few) molecule, and self-assembled films, which contain large amounts of molecules. The impact of the type of molecule used and the ratio of the dithiol molecules versus colloidal gold nanoparticles on the conductivity of the self-assembled nanostructures is studied by using different dithiol/thiol molecules and ratios of molecules versus particles. The conductivities of the self-assembled nanostructures were analyzed with respect to their dimensions and the interconnection type, resistances of molecules, and dimensions of the networks play an important role in determining the conductivity, which can be treated as a simplified model of an interconnected resistor network. To confirm our analysis, circuit modeling of the gold particle networks using LTspice is completed and our simulation results were consistent with the results observed from the experiments.

Chapter 4 summarizes the key points of the thesis and outlines possible future research directions and several types of potential applications, such as computational nanocells, memristor devices, information security and sensors.

The work presented in this thesis contributed to four conference presentations [40–43], one conference proceeding [44] and two journal papers are in preparation [45, 46].

Chapter 2 Modeling the Electronic Characteristics of Nanoscale Metal-Molecular Networks

This chapter presents semi-empirical calculations on dithiol molecule-metal cluster networks. By analyzing several properties including HOMO-LUMO gaps, energy levels, orbital spatial distribution, etc., we can predict the electronic properties of such nanoscale metal-molecular networks.

2.1 Computational Methods - Introduction

Molecular orbital (MO) theory is one method for studying molecular structures that assumes electrons move under the influence of the nuclei throughout the whole molecule, instead of being assigned to individual bonds between atoms. The wave function for each orbital describes the possible positions for one electron to appear and the molecular orbitals are approximated as a linear combinations of atomic orbitals (LCAO). Each molecule has a set of molecular orbitals and, for each molecular orbital, its wave function $\boldsymbol{\varphi_i}$ can be written as a weighted sum of a number of constituent atomic orbitals $\boldsymbol{\chi_\alpha}$, as the following equation:

$$\boldsymbol{\varphi_i}=\sum_{\alpha}^{M_{basis}} \mathbf{c}_{\alpha i}\, \boldsymbol{\chi_\alpha} \tag{2.1}$$

The atomic orbitals wave functions are also constructed as linear combinations of basis functions and at last are built as a group of real wave functions, which results in the molecular orbital wave functions being real-valued. In Figure 2.1, the yellow and blue color indicate the positive and negative sign of the specific molecular orbital wave

function. Thus the yellow/blue surfaces represent the isosurface of one specific value of the wave function.

HOMO LUMO

Figure 2.1 HOMO and LUMO of hydrogen molecule. Yellow/blue color represents positive/negative value of wave function. Value of the isosurface is 0.003.

The molecular orbital wave function can have a node with zero electron density between nuclei, due to the cancellation of atomic wave functions and is called an anti-bonding orbital. Electrons in bonding orbitals are concentrated between the nuclei and attract the nuclei to hold them together.

2.1.1 Hartree-Fock Method

With the power of modern computers, scientists are able to study the properties of systems from individual molecules to macroscopic structures consisting of tens of thousands of atoms.

To describe an atomic system one usually starts by solving the time-independent Schrödinger equation [47, 48]

$$\mathbf{H}_{tot}\mathbf{\Psi} = \boldsymbol{E}_{tot}\mathbf{\Psi}$$
$$\mathbf{H}_{tot}=\mathbf{T}_n+\mathbf{H}_e+-\frac{1}{2\mathrm{M_{tot}}}(\sum_i^{N_{elec}}\nabla_i)^2 \quad (2.2)$$

where $\boldsymbol{\Psi}$ is the wave function to be solved, $\mathbf{T}_{\boldsymbol{n}}$ is the kinetic energy operator of the nuclei. $\mathbf{H}_{\boldsymbol{e}}$ is the electronic Hamiltonian operator. $\mathbf{H}_{\boldsymbol{e}}$ represents the kinetic energy of the electrons and the interactions of nuclei to electrons, electrons to electrons and nuclei to nuclei and is a function that depends on the nuclear positions. Assuming that the there exists a full set of solutions to the electronic Schrödinger equation, then the equation can be written as

$$\mathbf{H}_{\boldsymbol{e}}(\boldsymbol{R})\,\boldsymbol{\Psi}_{\boldsymbol{i}}(\boldsymbol{R},\boldsymbol{r}) = \boldsymbol{E}_{\boldsymbol{i}}(\boldsymbol{R})\,\boldsymbol{\Psi}_{\boldsymbol{i}}(\boldsymbol{R},\boldsymbol{r}),\ i=1, 2, \ldots, \infty \qquad (2.3)$$

where **R** denotes the positions of nuclei and **r** denotes the positions of electrons. The Born-Oppenheimer approximation [47] assumes that the motions of electrons and nuclei can be separated and also ignores the coupling between nuclei and electron.

The electronic Schrödinger equation can only be solved exactly for simple one-electron systems such as H_2^+ the hydrogen atom. For general cases, we need to use numerical methods to calculate approximate solutions. The Pauli exclusion principle states that two electrons can't have the exact same quantum numbers and that requires the wave function to be antisymmetric [49]. The is achieved by building the wave function from Slater determinants (SDs) [49].

$$\boldsymbol{\Phi}_{\boldsymbol{SD}} = \frac{\mathbf{1}}{\sqrt{N!}} \begin{vmatrix} \boldsymbol{\varphi}_{\mathbf{1}}(\mathbf{1}) & \boldsymbol{\varphi}_{\mathbf{2}}(\mathbf{1}) & \cdots & \boldsymbol{\varphi}_{\boldsymbol{N}}(\boldsymbol{N}) \\ \boldsymbol{\varphi}_{\mathbf{1}}(\mathbf{2}) & \boldsymbol{\varphi}_{\mathbf{2}}(\mathbf{2}) & \cdots & \boldsymbol{\varphi}_{\boldsymbol{N}}(\boldsymbol{N}) \\ \vdots & \vdots & \ddots & \vdots \\ \boldsymbol{\varphi}_{\mathbf{1}}(\boldsymbol{N}) & \boldsymbol{\varphi}_{\mathbf{2}}(\boldsymbol{N}) & \cdots & \boldsymbol{\varphi}_{\boldsymbol{N}}(\boldsymbol{N}) \end{vmatrix}, \langle \boldsymbol{\varphi}_{\boldsymbol{i}} | \boldsymbol{\varphi}_{\boldsymbol{j}} \rangle = \ddot{\mathrm{o}}_{\boldsymbol{ij}} \qquad (2.4)$$

The columns in the Slater determinant are the single-electron wave functions or the so-called molecular orbitals (MO), which are the spatial orbitals multiplied with the spin orbitals α or β. In the Hartree-Fock method [50], the total wave function is a product of electron orbitals. The interactions between the particles are treated in an average fashion.

By proper selection of a special set of MOs, the energies of the MOs can be written as the Hartree-Fock equation

$$\mathbf{F}_i\boldsymbol{\varphi}_i=\boldsymbol{\varepsilon}_i\boldsymbol{\varphi}_i \tag{2.5}$$

where $\mathbf{F}_i$ is the Fock operator, which effectively describes the one-electron energy including the kinetic energy of an electron, the attraction to the nuclei and the repulsion to all the other electrons.

The Hartree-Fock equation can be written in a matrix notation

$$\mathbf{FC}=\mathbf{SC}\boldsymbol{\varepsilon} \tag{2.6}$$

where **F** is the Fock matrix, **C** is the coefficients matrix and **S** matrix represents the overlap between basis functions. **F** can be calculated as

$$\mathbf{F}=\mathbf{h}+\mathbf{G}\cdot\mathbf{D}$$
$$\boldsymbol{D}_{\gamma\ddot{o}}=\sum_{i}^{occ\ MO}\mathbf{c}_{\gamma i}\mathbf{c}_{\ddot{o}i} \tag{2.7}$$

D is called the density matrix representing the electron density, **h** represents the attraction by the nuclei and **G** denotes that the **D** matrix is contracted by a four-dimensional tensor.

The unknown MO coefficients $c_{\alpha i}$ are calculated by diagonalizing the Fock matrix, whereas the problem is that the MO coefficients need to be known to build the Fock matrix. Therefore, the calculation starts from a guess of the coefficients, then builds the **F** matrix and diagonalizes it. The new set of coefficients are compared with the former set of coefficients and, if they are different, the **F** matrix is built again with the new set of coefficients. The process continues iteratively until the new set of coefficients are equal to the former set and this process is called the self-consistent field calculation.

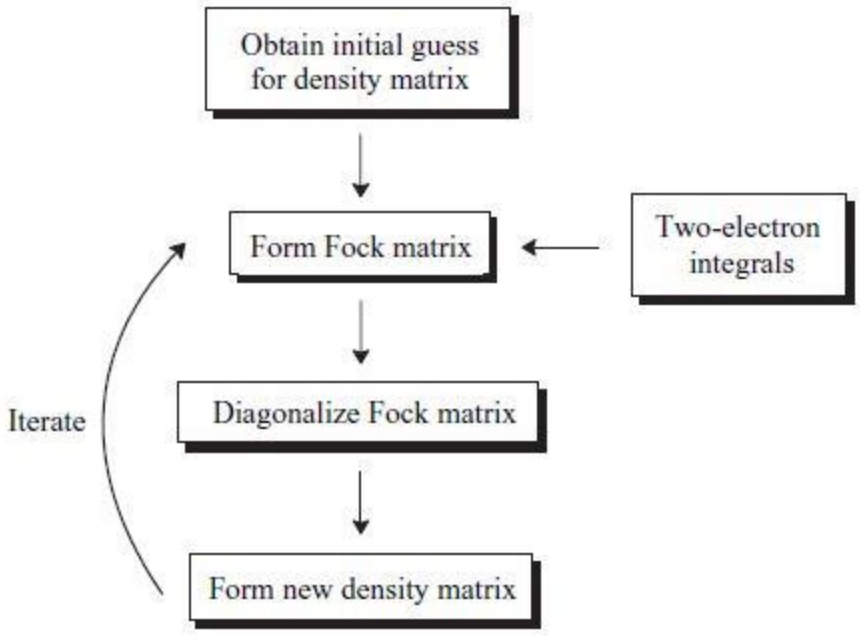

Figure 2.2 The SCF procedure (adapted from Ref. 2).

The procedure illustrated in Figure 2.2 consists of the following steps:

(1) Calculate all the electron integrals.

(2) Create a reasonable guess of the MO cofficients.

(3) Generate the initial density matrix **D**.

(4) Generate the Fock matrix. Two-electron integrals are calculated to give electron-electron repulsion.

(5) Diagonalize the Fock matrix and the eigenvectors are the new MO coefficients.

(6) Form the new density matrix and compare with the former density matrix. If not close enough, go to step (4) and repeat the process.

The above procedure includes the basic process of the Hartree-Fock calculation. In terms of the spatial orbitals, if there are no restriction on building the spatial orbitals, the trial function is called an unrestricted Hartree-Fock (UHF) wave function [51]. In systems

with a closed shell, restriction of the same spatial orbital for the two electrons on the same level is made and such wave functions are called restricted Hartree-Fock (RHF) wave functions.

Geometry optimization is the process finding the minima of the system's total energy that is a function of nuclear coordinates and, in most cases, iterative methods are required to locate the stationary points on the energy surface. Since the optimization problems in computational chemistry tend to have many variables, it is commonly assumed that the first derivative of the total energy function, the gradient **g**, is with respect to all the variables and can be calculated analytically. The Hellmann-Feynman theorem (equation 2.8) is used to calculate the intramolecular forces for geometry optimization and the equilibrium geometry is achieved when the forces acting upon the nuclei vanish into a small range.

$$\boldsymbol{F}_{\boldsymbol{X}_\gamma} = -\langle \boldsymbol{\psi} \left| \frac{\boldsymbol{\partial H}}{\boldsymbol{\partial X}_\gamma} \right| \boldsymbol{\psi} \rangle \qquad (2.8)$$

where $\boldsymbol{F}_{\boldsymbol{X}_\gamma}$ is the force, *H* is the Hamiltonian operator, $\boldsymbol{\psi}$ is the wave function, and $\boldsymbol{X}_\gamma$ is a parameter.

The Newton-Raphson (NR) method expands the true function ***f*(x)** to second order around the current point $\mathbf{x_0}$:

$$f(\mathbf{x}) \approx f(\mathbf{x_0}) + \mathbf{g}(\mathbf{x} - \mathbf{x_0}) + \frac{\mathbf{1}}{\mathbf{2}} (\mathbf{x} - \mathbf{x_0})^2 \mathbf{H} \qquad (2.9)$$

and, by requiring the gradient of the second-order approximation to be zero, the step is

$$(\mathbf{x}-\mathbf{x_0}) = -\mathbf{H}^{-1}\mathbf{g} \qquad (2.10)$$

Where **g** is the gradient of energy and **H** is the Hessian matrix which represents the second derivative of energy, referred as force constant. The total energy and its first derivatives are calculated after the SCF calculation of each cycle and are used to make displacements of the atomic coordinates to optimize the system's geometry. The procedure continues until the net inter-atomic force on each atom is acceptably close to zero and the total energy is on a stationary point on the potential energy surface.

2.1.2 Density Functional Theory

Besides the Hartree-Fock method, another main category of quantum computational methods is the density functional theory (DFT) method [52]. Instead of dealing with the wave functions directly, DFT takes the electron density as a functional for calculating the energies. The basis of the applicability of DFT is given by Honhenberg and Kohn that the electronic energy of the ground state can be determined completely by the electron density [52]. The energy functional in the electronic Schrödinger equation can be divided into three parts, the kinetic energy $\mathbf{T}[\rho]$, the potential energy of the attraction between the nuclei and electrons $E_{ne}[\rho]$ and the repulsion between electrons $E_{ee}[\rho]$, where ρ is the electron density.

$$\mathbf{H= T}[\boldsymbol{\rho}]+ \boldsymbol{E_{ne}}[\boldsymbol{\rho}]+ \boldsymbol{E_{ee}}[\boldsymbol{\rho}] \tag{2.11}$$

The foundation of the success of DFT methods is introduction of the use of orbitals by Kohn and Sham (KS) in 1965 [53] to address the main flaw DFT methods had of poor description of the kinetic energy. The KS formalism splits the kinetic energy functional into two parts, one that can be calculated from an auxiliary set of orbitals used for

describing the approximate electron density plus a correction term. The approximate electron density is written in terms of the one-electron wave functions

$$\boldsymbol{\rho_{approx}}=\sum_{i=1}^{N_{elec}} |\boldsymbol{\varphi_i}|^2 \quad (2.12)$$

The Kohn-Sham theory calculates the kinetic energy with the assumption of no electron interaction and the remaining kinetic energy is absorbed into the exchange-correlation term $E_{xc}[\rho]$, which is the remaining part after subtraction of the non-interacting kinetic energies plus the potential energy terms.

Between different DFT methods, the main difference is the choice of the exchange-correlation energy functional. In the Local Density Approximation (LDA) [54], the electron density is assume to be varying slowly so that it can be treated as a uniform electron gas. The Generalized Gradient Approximation (GGA) [55] methods improves the exchange-correlation energy by inclusion of the first order derivative of the density.

2.1.3 Semi-empirical Methods

The word “ab initio” is latin for “from the beginning”. A calculation is called ab initio if the calculation is conducted without using of any experimental data and all the results are obtained from the pure theory. However the run time cost of ab initio would be very high for large systems made of hundreds of atoms since the cost of calculation scales as the fourth power of the number of basis functions [56] (similar to DFT calculations, for example). Semi-empirical methods reduces the computational cost by incorporating experimental data to parameterize the two-electron integrals [57]. The incorporation of experimental data in the calculation also increases the accuracy in many situations.

Zero Differential Overlap (ZDO) is the central assumption in semi-empirical methods that neglects all the products of basis functions that depend on the same electron coordinates when located on different atoms, which leads to the following consequences:

(1) The overlap matrix **S** is reduced to unit matrix.

(2) One-electrons with three centers (two from the basis functions and one from the operator) are reduced to zero.

(3) All three- and four-center two-electron integrals are neglected.

For compensation of the above approximations, the other integrals are parameterized with their values assigned according to calculations or experimental data. Various semi-empirical methods differentiate with each other by how many integrals are neglected and how the parameterization is achieved.

Without further approximation the above assumptions form the basis of the Neglect of Diatomic Differential Overlap (NDDO) approximation. Using μ, ν to denote the s- or p-type orbitals, the overlap integrals can be written as

$$S_{\mu\nu} = <\mu|\nu> = \delta_{\mu\nu}\delta_{AB} \tag{2.13}$$

The one-electron operator is

$$\mathbf{h} = -\frac{1}{2}\nabla^2 - \sum_{\alpha}^{N_{nuclei}} \frac{Z'_{\alpha}}{|\mathbf{R}_{\alpha} - \mathbf{r}|} = -\frac{1}{2}\nabla^2 - \sum_{\alpha}^{N_{nuclei}} V_{\alpha} \tag{2.14}$$

Z'_a denotes that the nuclear charge is reduced by the core electrons.

The one-electron integrals are

$$<\chi_A|\mathbf{h}|\chi_A> = <\chi_A|-\frac{1}{2}\nabla^2 - V_A|\chi_A> - \sum_{\alpha}^{N_{nuclei}} < \chi_A|V_a|\chi_A > \tag{2.15}$$

$$<\chi_A|\mathbf{h}|\chi_B>=<\chi_A|-\frac{1}{2}\nabla^2 - V_A - V_B|\chi_B>$$

$$<\chi_A|V_C|\chi_B>=0$$

MNDO, AM1 and PM3 are all parameterizations of the NDDO approximation where the parameterizations are made in terms of atomic variables and the only difference is how the core-core repulsion, which is the repulsion between nuclear charges properly reduced by the number of core electrons, is treated and how the parameters are assigned:

The main approximation in the Modified Neglect of Diatomic Overlap (MNDO) [58] model is the formula of the core-core repulsion

$$V_{nn}^{MNDO}(A,B)=Z_A'Z_B'<s_As_A|s_Bs_B>(1+e^{-\alpha_A R_{AB}}+e^{-\alpha_B R_{AB}}) \qquad (2.16)$$

The α exponents are fit as parameters and the interaction that involves O-H and N-H bonds are treated differently

$$V_{nn}^{MNDO}(A,H)=Z_A'Z_H'<s_As_A|s_Hs_H>(1+R_{AH}e^{-\alpha_A R_{AH}}+e^{-\alpha_H R_{AH}}) \qquad (2.17)$$

The two-electron integrals are either evaluated based on spectroscopic data or by multipole-multipole interactions from classical electrostatics.

Austin Model 1 (AM1) [59] modifies the core-core function by addition of the Gaussian function to address the large activation energy problem encountered in MNDO – too high for bond breaking/forming reaction. The core-core repulsion in AM1 is given

$$V_{nn}^{AM1}(A,B)=V_{nn}^{MNDO}(A,B)+\frac{Z_A'Z_B'}{R_{AB}}\sum_k(a_{kA}e^{-b_{kA}(R_{AB}-c_{kA})^2}+ a_{kB}e^{-b_{kB}(R_{AB}-c_{kB})^2}) \qquad (2.18)$$

The k is a variable between 2 to 4. The activation energy and hydrogen bond strength are improved compared to MNNDO. AM1 is a considerable improvement over MNDO and has been parameterized for many of the main-group elements.

Unlike MNDO and AM1 in which the parameterization is done by directly fitting to experimental data, Parametric Method number 3 (PM3) [60] uses a complex optimization algorithm to search for the optimized parameters automatically, where the optimization process is made by deriving and implementing formulas for the derivative of a suitable error function. All the parameters are optimized simultaneously including the two-electron integrals. The AM1 formula for the core-core repulsion is kept with only two Gaussians assigned to each atom. The Gaussian parameters are implemented as an integral part of the model that are allowed to vary freely. With this method, a global minimum point could be reached given a set of experimental data. Statistically, PM3 was more accurate than the other semi-empirical methods at the time it was invented [61], although there were several deficiencies of it for certain cases such as the low rotational barrier for the amine bond.

To further improve the performance of semi-empirical calculations, several new methods were introduced. Examples are Parametric Method number 5 (PM5) [62], AM1* [63], and Semi Ab Initio Method 1 (SAM1) [64].

The computational time cost of performing an Hartree-Fock calculation usually scales as the fourth power of the number of basis functions used due to the two-electron integrals

involved in the calculation. Semi-empirical methods largely reduce the computational cost by reducing the calculations of integrals via parameterization with empirical data. Semi-empirical calculations are much faster than ab-initio methods and have been successfully used in describing organic structures where only a few elements are used extensively and the system is of moderate size. In this work we focused on using semi-empirical methods for modeling dithiol molecule-metal cluster networks because of its computational accuracy and efficiency.

2.2 Simulated Nanostructures and Methods

2.2.1 Nanostructures Simulated

1, 4-benzenedithiol is one representative of the group of conjugated dithiol molecules, which is more conductive than its saturated alkanedithiol counterparts [65]. The molecule has a rigid geometry and possesses delocalized π-electrons that makes it one of the simplest systems to study [66]. The sandwiched structure of benzenedithiol molecule bound between two gold electrodes has be simulated extensively by researchers [65], [67–71], including the interactions between the molecular orbitals and the surface metal states upon absorption of benzenedithiol onto gold electrodes [70], the electronic properties of the sandwiched structures [65, 67, 69, 70] and the electron transport characteristics through single benzenedithiol molecules between gold electrodes [65], [67–69, 71], as illustrated in Figure 2.3. The Fermi level is located between within the HOMO-LUMO gap of the molecule [65, 69, 71] and it is the spatially delocalized molecular orbitals close to the Fermi level that are responsible for the electron transport through the molecular junction [65, 67, 69, 71]. The simulated current-voltage

characteristics show consistency with the data measured in experiments although discrepancy of 2-3 orders of magnitude of the molecule's conductance is also observed [67, 68, 71].

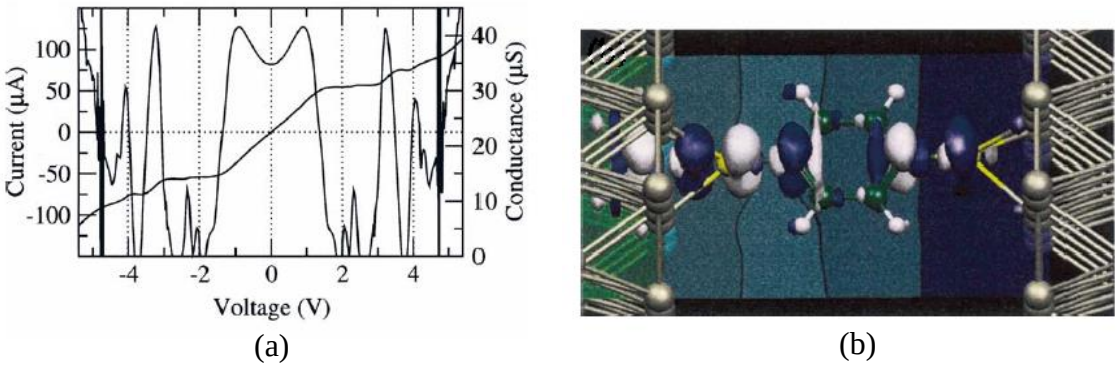

(a) (b)

Figure 2.3 (a) Current-voltage plot of benzenedithiol bridged between two gold electrodes; (b) Schematic of the junction with isosurface of the induced density and the potential drop through the molecule at bias of 1 V (adapted from Ref. 68).

Inspired by the previous work simulating single benzenedithiol bridged to bulk electrodes, we modeled systems that consist of benzenedithiol molecules interconnected with metallic nanoclusters. By shrinking the bulk electrodes to nanoscale metallic clusters, it allows one to build multiple molecular junctions together and therefore leads to the creation of nanoscale networks, where the electronic structure analysis of single molecule contact devices is extended to a system consisting of multiple metal-molecule nanojunctions. The metallic nanocluster used here is the planar Al_6 cluster, which is one of the stable isomers of Al_6 [72–74]. The size of the cluster is comparable to the size of benzenedithiol molecule and, by connecting benzenedithiol molecules and Al_6 clusters together, a group of molecular chains consisting of one to four molecular junctions were created as shown in Figure 2.4. 1, 3, 5-trithiol-benezene is the trithiol counterpart of benzenedithiol [75] and, by adopting it into our structures, networks with multiple

branches were constructed, such as the Y-shaped and H-shaped networks in Figure 2.5. In addition, molecular chains made of hexanedithiol, octanedithiol and decanedithiol were also modelled for comparison with benzenedithiol.

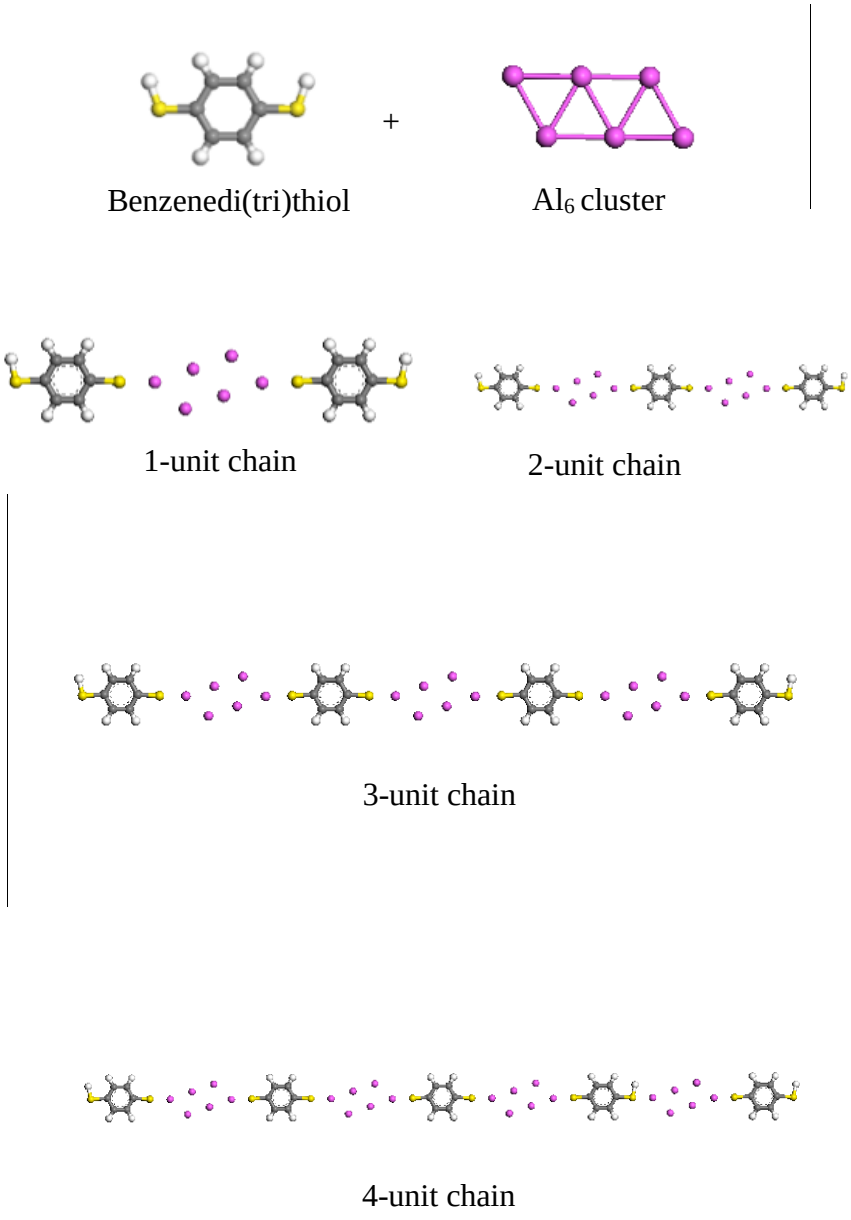

Figure 2.4 Building blocks and starting unrelaxed structures for benzenedithiol-Al_6 cluster chains.

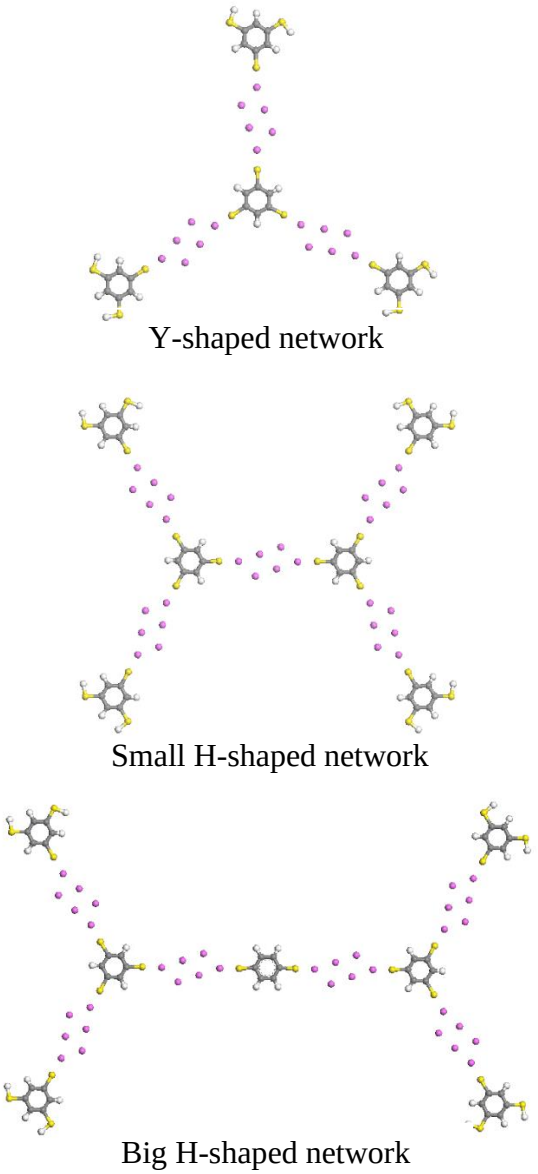

Figure 2.5 Building blocks and starting unrelaxed structures for benzenedithiol-Al_6 cluster chains and benzenetrithiol-Al_6 Y-/H-shaped networks.

2.2.2 Details of Modeling Method

All calculations were performed using VAMP, an Accelrys Materials Studio general semi-empirical molecular orbital package. VAMP provides fast and reliable calculations

of structures and properties of molecules related structures and provides a trade-off compared to first-principles methods, which require much more computing resources. Root-mean-square (RMS) force for the geometry optimization that measures the force displacement from the local minimum point is set to be at least 0.4 $kcalmol^{-1}Å^{-1}$. The SCF tolerance that determines whether the SCF procedure converges is set to be at least 1×10^{-5}. The isosurface value for all molecular orbital plots shown was 0.003. Three Hamiltonians AM1 [59, 76, 77] , AM1* (extended Austin Model 1 [63, 78]) and PM3 [77, 79, 80] were used for the calculations of dithiol molecules, Al clusters and the molecule-Al cluster chains and networks. Although AM1* is supposed more accurate than AM1, it didn't converge for most calculations except for the isolated molecules. PM3 calculations can complete properly for all the structures we modeled but there was always a shift in the energy levels that did not agree with reference data. Three Hartree-Fock methods RHF, UHF [51] and A-UHF (annihilated Hartree-Fock method) were also tested. The relaxed structures calculated with UHF usually have problem with their spin state except for dithiol molecules and Al_6 cluster with triplet spin state and A-UHF doesn't converge in most cases. As a result, the geometry of 1, 4-benzenedithiol and other alkanedithiol molecules were optimized using the AM1* Hamiltonian and UHF method and the geometry of Al_6 cluster was relaxed using AM1 Hamiltonian and also UHF method. All metal-molecule structures were built using optimized molecules and unrelaxed Al_6 clusters (Figure 2.4 and 2.5). The resulting extended molecule-Al_6 cluster chains and networks were modeled with the AM1 Hamiltonian and RHF method. The typical Al-S bond lengths in the starting structures were 2.1 Å and 2.2 Å.

2.3 Results and Analysis

2.3.1 Relaxed Geometries

The benzenedithiol molecule was the first structure we modeled. The HOMO-LUMO gap is one important parameter to determine the quality of calculation and, to be confident that our optimized geometries are real, we compared the HOMO-LUMO gaps of our relaxed molecules with the data of other experimental and theoretical works. In our calculation, the HOMO-LUMO gap of benzenedithiol was 8.431 eV, which compares well with the reported values between 8.6 and 9.11 eV [81, 82]. The detailed data are shown in Table 2.1. The calculated bond lengths for relaxed geometry of benzenedithiol were also compared with [83] for all bond types, as shown in Table 2.2, except for S-H probably due to the different method used. For 1, 3, 5-trithiol-benzene, the calculated bond lengths were also consistent with previous work [75].

Table 2.1 HOMO, LUMO energies and gap in our calculation and other works.

HOMO (eV)	LUMO (eV)	LUMO-HOMO gap (eV)	Source
-8.455	-0.024	8.431	This work
-8.35	0.76	9.11	[82]
-7.95	0.74	8.69	[82]
-8.3	0.3	8.6	[81]

Table 2.2 Comparison of calculated bond lengths of benzenedithiol in this work with data from Ref. 83.

	This work	Ref. 83
C-C (Å)	1.395	1.4
C-S (Å)	1.807	1.77
C-H (Å)	1.101	1.09
S-H (Å)	1.418	1.35

We focused on small Al clusters (n=2-6) in order to ensure the computational efficiency of our semi-empirical calculations. There are many local minima in the potential energy surface, which leads to a rich variety of structure of Al clusters [72–74], as shown in Figure 2.6. We simulated Al clusters of several sizes from Al dimer to Al_6 cluster (Figure 2.7 (c)). Our simulations showed that Al_6 cluster was the best fit for our calculations since it was stable both by itself and when connected to dithiol molecules and the symmetric geometry made it easy to build molecular junctions with S atom on its two long diagonal ends. The most stable structure of an isolated Al_6 cluster was reported to be the planar parallelogram [72, 74] or bipyramid structure [72–74] and in our simulations a slightly distorted planar structure was calculated to be the most stable structure of Al_6 with a triplet spin multiplicity in the ground state. The calculated Al-Al bond lengths were between 2.3 to 2.5 Å, a bit smaller than other work (~ 2.5 to 2.8 Å) [72–74]. The aluminum cluster had a HOMO-LUMO gap of 4.709 eV and the HOMO energy was -7.487 eV, which is comparable to the ionization potential of Al_6 clusters in [72, 73] where it was reported to be around -7 eV.

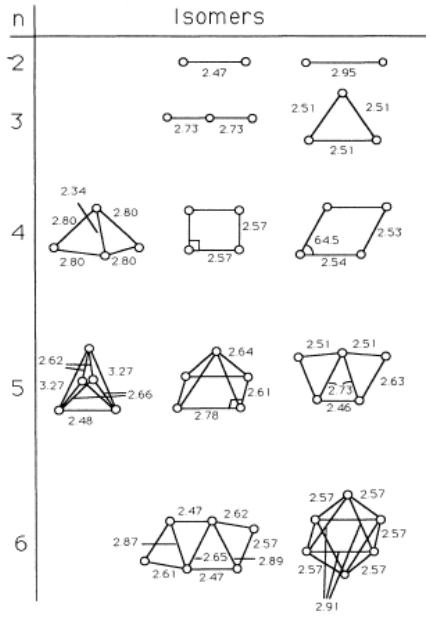

Figure 2.6 Minimum-energy structures of Al_n clusters, n=2-6 (adapted from Ref. 74). Bond lengths are labeled aside the corresponding Al-Al bond.

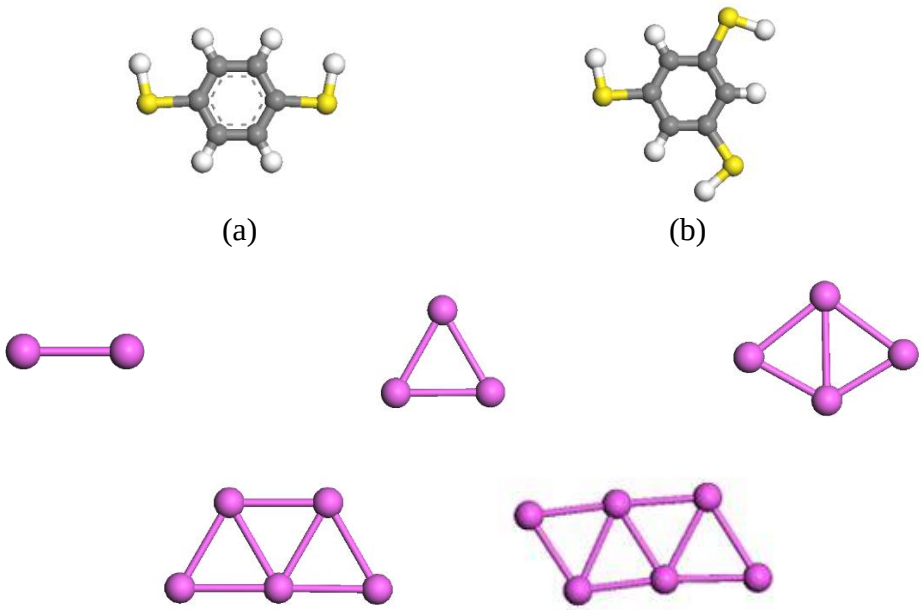

Figure 2.7 Relaxed geometries of (a) single benzenedithiol molecule relaxed with AM1*-UHF; (b) single 1, 3, 5-trithiol-benzene molecule relaxed with AM1*-UHF; (c) single clusters from Al dimer to Al_6 cluster. Al_6 cluster is relaxed with AM1-UHF-triplet.

In the relaxed geometries of the metal-molecule junctions, the dithiol molecules and the Al_6 clusters retained similar structures as in the isolated condition. The shape of the Al_6 cluster might be distorted due to the interaction with the molecule, as shown for the 3-unit and 4-unit benzenedithiol-Al_6 chains in Figure 2.8, but in most cases the Al_6 cluster retained the similar structure as the single Al_6 cluster of Figure 2.7 (c).

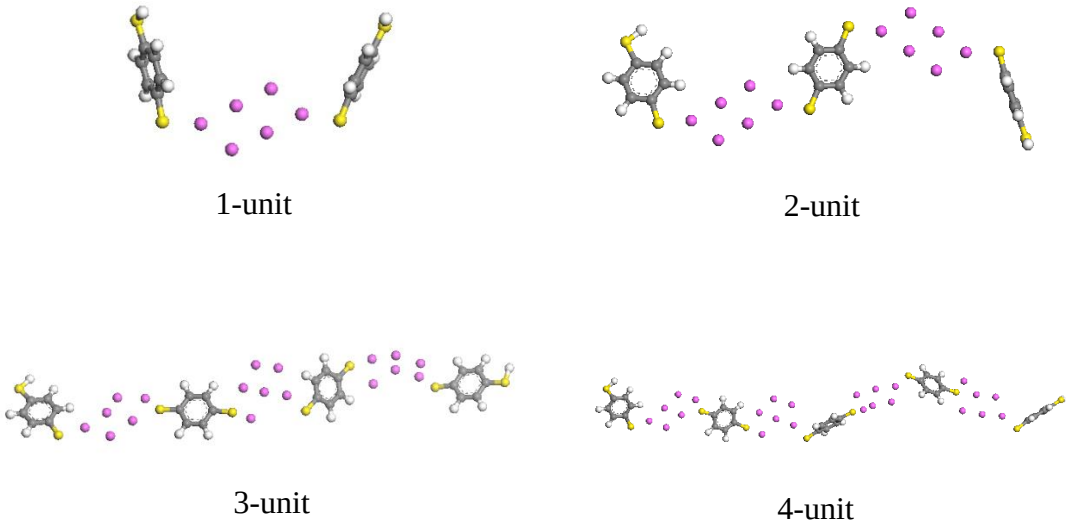

Figure 2.8 Relaxed geometries for benzenedithiol-Al_6 chains 1-unit to 4-unit.

For the benzenedithiol-Al_6 chains (1-unit to 4-unit), the benzenedithiol molecule was coupled well with the neighboring Al clusters, which was consistent with the property of S atom to form covalent bonds with metal atoms (Au, Ag, Al, etc.) [84–88]. The geometries of the benzenedithiol-Al_6 chains and networks (Figures 2.8 and 2.10) were distorted to certain extent compared to their starting structures in Figure 2.4 and 2.5. This was considered to a certain extent due to the good coupling between the benzenedithiol molecule and Al_6 cluster, which will be discussed in more detail later. This point is

supported when comparing with the alkanedithiol-Al_6 chains. As seen in Figure 2.9, the octanedithiol chains take well-aligned geometries and hexanedithiol and decanedithiol chains retain similar structures.

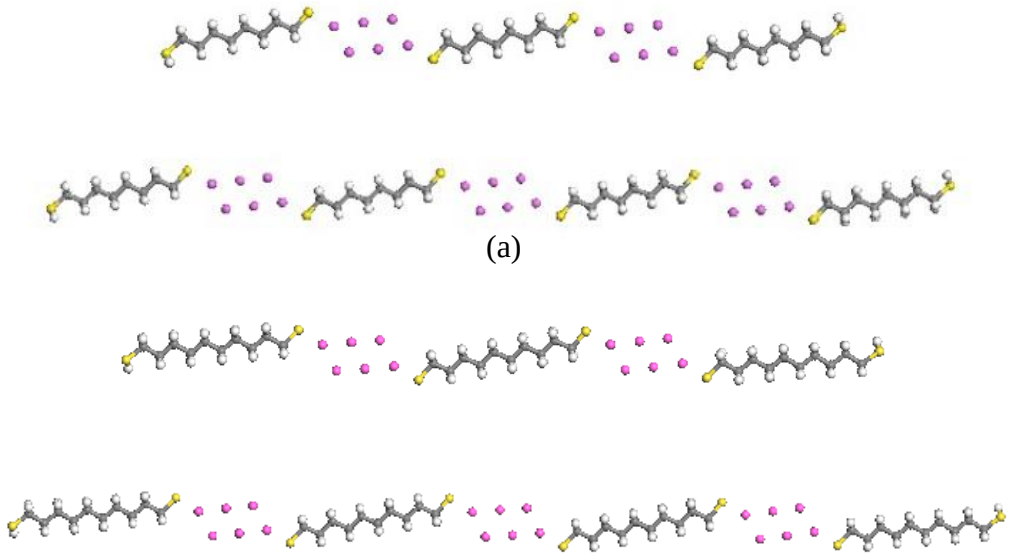

(a)

(b)

Figure 2.9 Relaxed geometries of (a) octanedithiol 3, 4-unit chains; (b) decanedithiol 3, 4-unit chains. All relaxed with AM1-RHF.

The relaxed Al-S bond lengths varies between 1.8 to 2.5 Å for all the structures we simulated (benzenedithiol chains and networks and alkanedithiol chains), which was similar to previous work [89, 90].

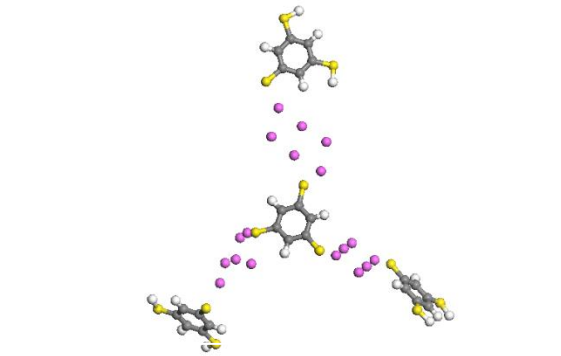

Y-shaped network

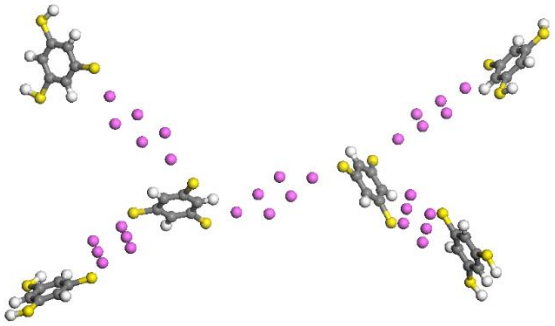

Small H-shaped network

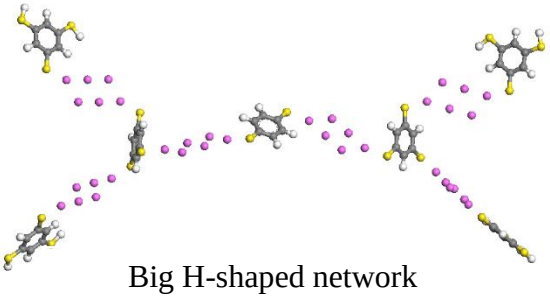

Big H-shaped network

Figure 2.10 Relaxed geometries of Y-shaped and H-shaped networks with AM1-RHF.

2.3.2 Energy Levels and HOMO-LUMO Gap

The ionization potential of a system modeled within the Hartree-Fock formalism can be equated to the negative value of the HOMO according to Koopmans' theorem [91, 92]. Although Koopmans' theorem doesn't claim the correspondence between electron affinity and the LUMO explicitly, several works have confirmed this and it is possible to generalize this theorem to the electron affinities [93–95]. In our simulation, the ionization

potentials of the metal-molecular structures were taken as the HOMO energy, which typically were around -7.5 eV. This value is consistent with Ref. 88 where the energy levels of another thiol molecule, methanethiol, adsorbed on the surface of aluminum were studied via ultraviolet photon spectroscopy.

We studied the HOMO-LUMO gap of our structures very carefully since it is typically an indicator of the system's electron transport properties and describes the tunneling barrier for the electron to transport through the junction. From other works, we see modification of the HOMO-LUMO gap has been examined for molecules with different endgroups [71, 96] and upon connecting molecules to metallic electrodes [65, 67–71, 96, 97, 98]. The smaller the HOMO-LUMO gap is, the lower the barrier is for electron to transport through the molecule. The HOMO-LUMO gap of the benzenedithiol-Al_6 structures decreased by several eV compared to the isolated molecule in our simulation, as shown in Table 2.3, which indicates possible good conductivity of interconnected benzenedithiol and Al_6 cluster systems. The HOMO-LUMO gap keeps decreasing as a function of the number of junction units in the benzenedithiol-Al_6 molecular chains, which is an indicator of decreased molecular barrier to charge transport, as shown in Figure 2.11.

Table 2.3. Calculated values of the HOMO-LUMO gap for various structures.

Structures	HOMO-LUMO gap (eV)
1,4-dithiolbenzene	8.431
Al_6-cluster	4.709
Benzenedithiol-Al_6 cluster 1-unit chain	5.162
Benzenedithiol-Al_6 cluster 2-unit chain	5.067
Benzenedithiol-Al_6 cluster 3-unit chain	4.453
Benzenedithiol-Al_6 cluster 4-unit chain	4.264

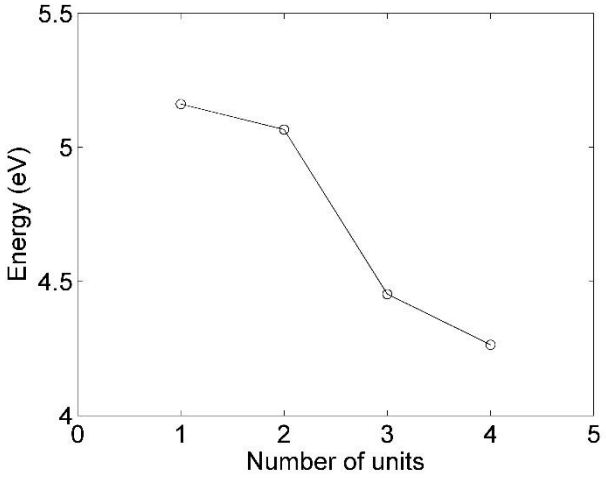

Figure 2.11 HOMO-LUMO gaps of benzenedithiol-Al_6 chains versus number of units.

Associated with the trend of the HOMO-LUMO gap, the ionization potentials and electron affinities, or equivalently the positions of the HOMO and LUMO are also changing with the benzenedithiol-Al_6 chain length. The HOMO energies increase versus chain length, while the LUMO energies decrease, as shown in Figure 2.12. It is generally believed that the HOMO and LUMO are the descriptors of the tunneling barrier to electron transport. The higher/lower the energy of the HOMO/LUMO the more effective a molecular system will be at transporting charge [99]. The changing trend of HOMOs and LUMOs points to increased electrical conductance as these superstructures are extended.

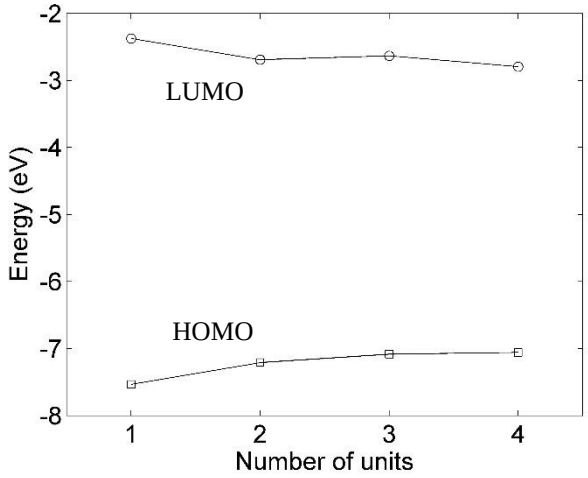

Figure 2.12 HOMO and LUMO position versus the number of units in benzenedithiol-Al_6 chains.

In the orbital energy spectrums of isolated Al_6 cluster, benzenedithiol molecule and one unit chain, it can be seen that the HOMO of the Al_6 cluster lies in the molecular HOMO-LUMO gap. If we consider the HOMO of Al_6 as the Fermi level (dotted line, Figure 2.13), this phenomenon is similar to the Fermi level alignment reported in other works [65, 67, 68, 97], where the Fermi level of metal electrode contacts lie inside the HOMO-LUMO gap of the molecule. The energy levels near the HOMO-LUMO gap for benzenedithiol-Al_6 linear chains become more closely spaced as chain length increases, shown in Figure 2.14. Such behavior indicates that these molecular orbitals could provide an extended pathway for transferring charge from one end to another and may signify that an electronic band is starting to form as occurs in semiconductor crystals.

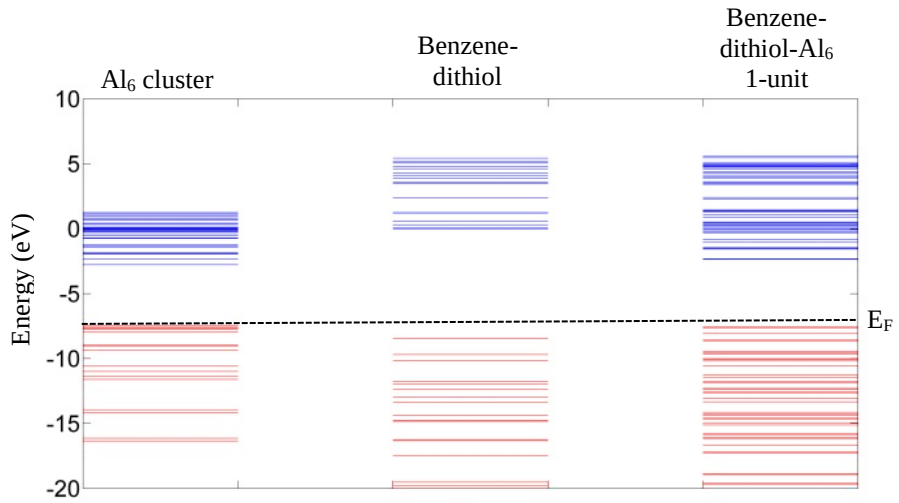

Figure 2.13 Orbital energy spectra for structures indicated. Red lines represent energy level of HOMO and below, blue lines represents LUMO and above.

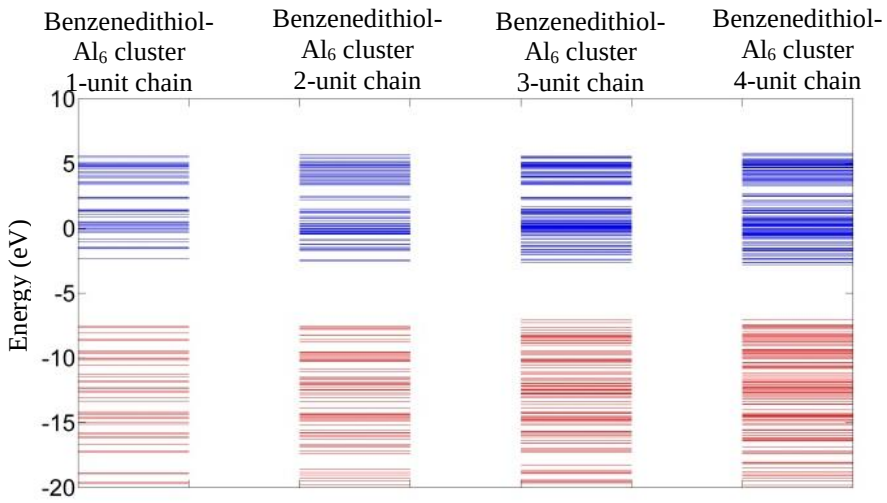

Figure 2.14 Orbital energy spectrum of benzenedithiol-Al_6 chains versus length.

2.3.3 Electron Transport Properties

The degree of molecular orbital delocalization and the coupling between a molecule and electrode are important factors that influence the electron transport property of a molecular system [65, 67–69, 71, 96, 97]. Well-delocalized orbitals near the HOMO-

LUMO gap usually correspond to peaks in the transmission probability and the associated electronic density of states. This type of correspondence between delocalized orbitals and transmission has been studied thoroughly in Ref. 67, which reported that several individual well-delocalized orbitals contributed to their corresponding peaks in the transmission of the benzenedithiol molecule bridging between two gold electrodes. Besides well delocalized orbitals, Ref. 67 also discussed the collective effect of two or more energetically close molecular orbitals combined together for large transmission to create an electron transport path. Thus we examined the orbitals close to the HOMO-LUMO gap closely to analyze the electron transport characteristics of our structures.

In the isolated molecules, we can get an idea about the conductivity difference between benzenedithiol and alkanedithiols. The orbitals of benzenedithiol show delocalized π-bonding features, as expected for conjugated organic molecules, as in Figure 2.15. It is well known that benzenedithiol is more conductive than alkanedithiols [65] and the different delocalization/localization features correspond with the different conductivities between molecules. In addition, the Al_6 cluster displays well-delocalized orbitals consistent with large free electron density in the metallic particle.

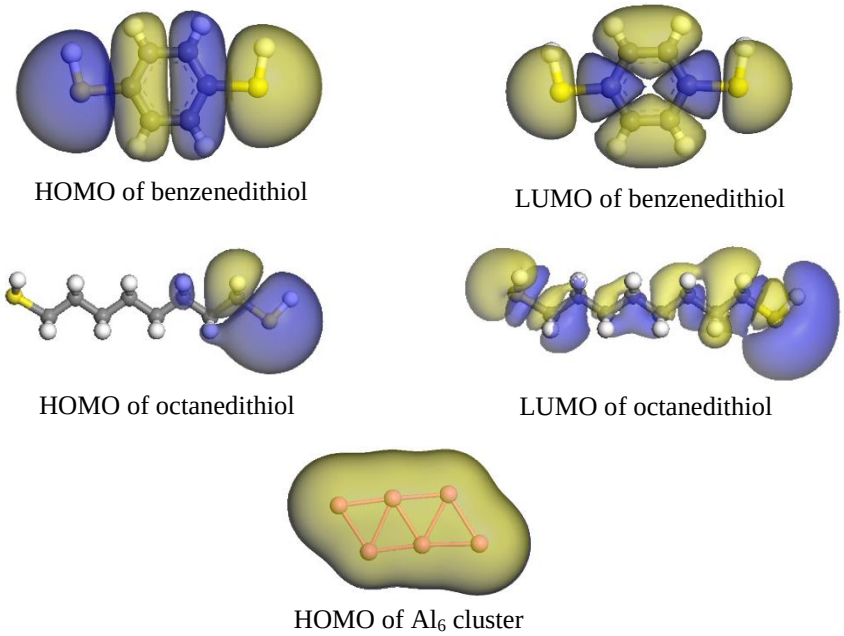

Figure 2.15 Orbitals of relaxed benzenedithiol molecule, octanedithiol molecule and Al_6 cluster. Isosurface colors correspond to the sign of wave function.

For the combined metal-molecule structures, the orbitals are either well-delocalized and extend significantly throughout the structure or overlap with other energetically close orbitals to form possible electron transport paths. In Figure 2.16, the HOMO and LUMO orbitals of 1-unit and 2-unit benzenedithiol-Al_6 chains show that the benzenedithiol molecules and Al_6 clusters are well coupled and the molecular orbitals are delocalized through the whole structure. These type of well delocalized molecular orbitals are common in the short chains of 1-unit and 2-unit and can be seen as a conducting path for one electron transport through the structure.

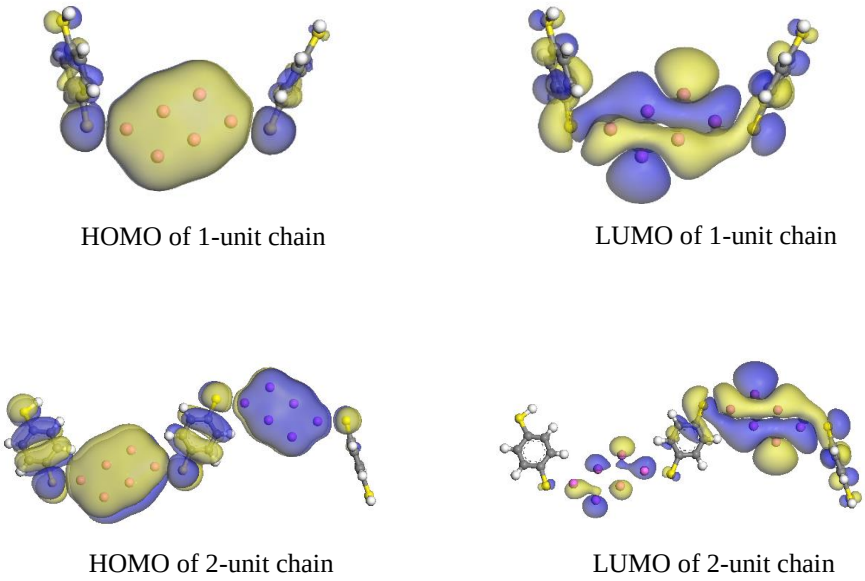

Figure 2.16 HOMO and LUMO of 1-unit and 2-unit benzenedithiol-Al_6 chains.

In 3-unit chain, the collective effect of energetically close orbitals starts to become more remarkable while we can still see well delocalized orbitals on this structure. As seen in Figure 2.17, LUMO+3 is well delocalized through the whole structure, which contributes one transport pathway for electron and orbitals HOMO-3 and HOMO-2, HOMO-1 and HOMO, LUMO to LUMO+2 are quite close in energy respectively. HOMO-3 mainly localizes on the middle Al_6 cluster and its two neighbor molecules and HOMO-2, which is only 0.217 eV higher than it mainly localizes on the right unit. For the range of energy close to HOMO-1 and HOMO, HOMO-1 localizes in the middle and HOMO localizes on the right and again they form another conduction path for electrons. When an electron with close energy to these orbitals tunnels onto the structure, it can be quite easy for the electron to hop from one orbital to another and thus transport through the whole structure. Similar properties can be found on orbitals of LUMO to LUMO+2 with LUMO localizing in the middle, LUMO+1 localizing on the left and LUMO+2 localizing on the

right. The contribution of these orbitals to transmission can be seen more clearly when we associate them with the electronic density of states (DOS) of the 3-unit chain. As shown in Figure 2.18, HOMO-2 and HOMO-3 are around 0.2-0.3 eV from the first peak below HOMO and LUMO, LUMO+1 and LUMO+2 together give rise to the first peak above LUMO.

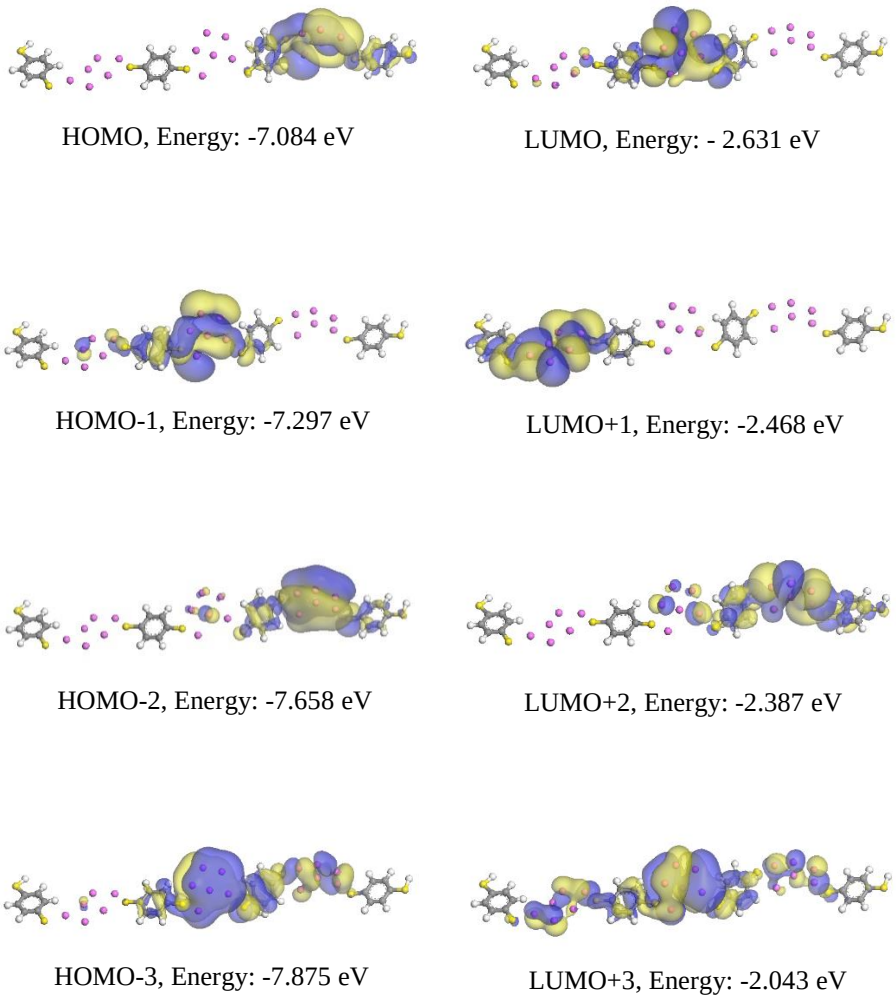

Figure 2.17 Frontier orbitals of benzenedithiol-Al_6 3-unit chain.

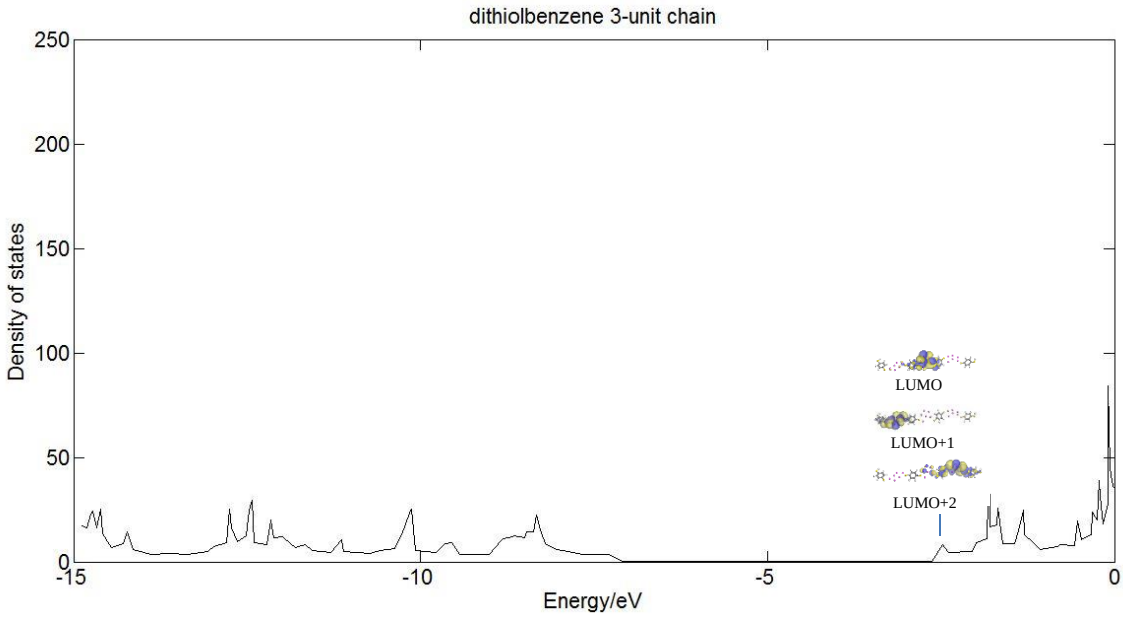

Figure 2.18 Electronic density of states of benzenedithiol 3-unit chain.

Similar behaviour is found on the 4-unit chain: As shown in Figure 2.19, although there are no well-delocalized orbitals, the HOMO-1, HOMO-2 and HOMO-3 are energetically close and couple to each other in the spatial distribution as do the LUMO, LUMO+1 and LUMO+2. In the DOS, the HOMO-7 to HOMO-4 together contribute to the first peak below HOMO and, on the LUMO side, the first peak is made of contributed LUMO, LUMO+1 and LUMO+2, as illustrated in Figure 2.20.

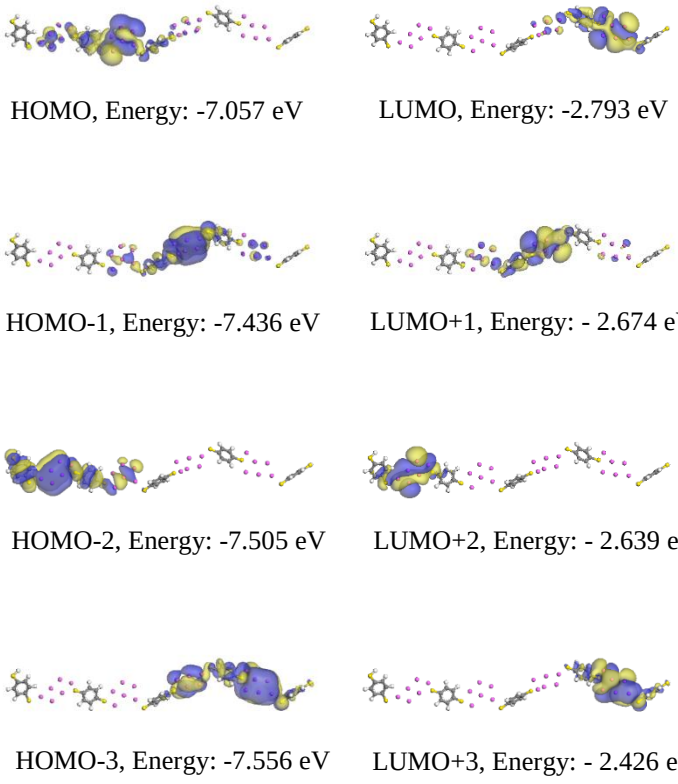

Figure 2.19 Selected frontier orbitals of benzenedithiol 4-unit chain.

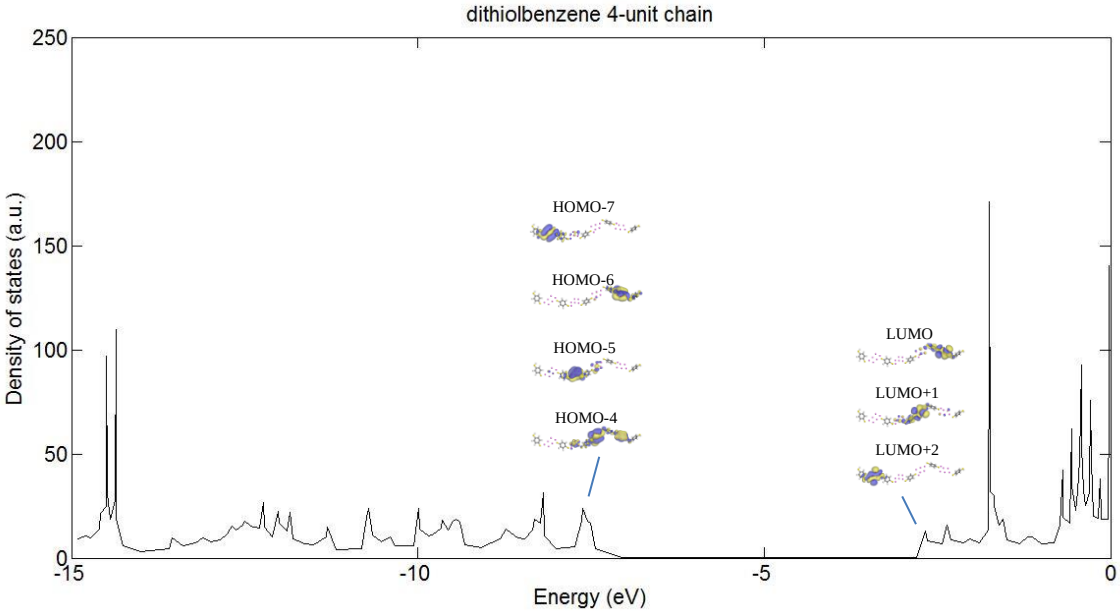

Figure 2.20 Density of states of benzenedithiol 4-unit chain.

Typical frontier orbitals for Y- and H-shaped molecular networks composed of 1, 3, 5-benzenetrithiol have spatial distribution around the HOMO-LUMO gap that are well-delocalized or overlap with other orbitals close in energy, as shown in Figure 2.21. Take the Y-shaped network for example and we can see that HOMO-1 to HOMO-3 of which two are well delocalized and HOMO-3 compensates the branch where the others have less weight. For energetically close orbitals LUMO to LUMO+3, the orbitals together cover the whole structure. The energy level spectra of the networks were also consistent with the linear chain structures described above indicating electron transport pathways exist with band-like formation evident.

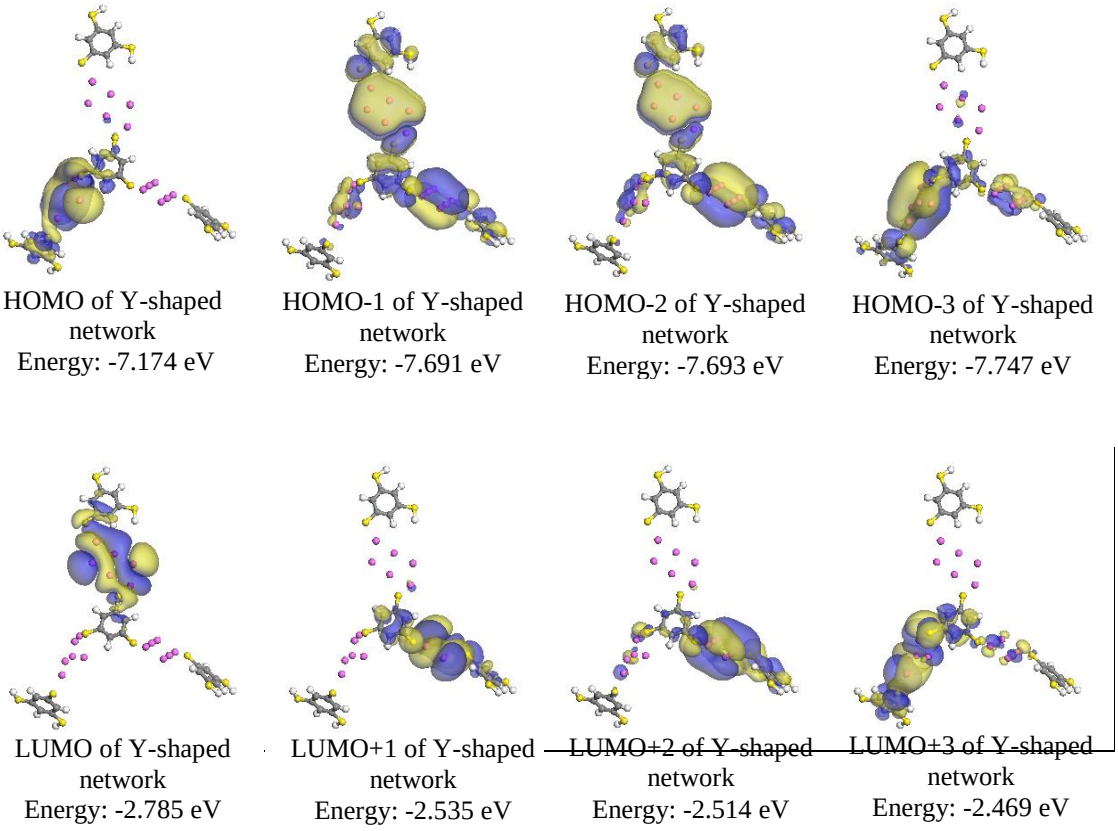

Figure 2.21 Frontier orbitals of Y-shaped, small H-shaped and big H-shaped networks.

For comparison, we also studied structures based on alkanedithiols with saturated C-C, which are usually found to be poor conductors compared to conjugated molecules such as benzenedithiol because of their larger HOMO-LUMO gaps (e.g., 10.014 eV for octanedithiol in our calculations) and exponential decrease in transmission probability with distance [65]. The frontier orbitals of an octanedithiol 3-unit linear chain are shown in Figure 2.22. The orbitals are mainly localized on the metallic clusters with little extension onto the molecule, which thus makes the electrons confined in one region and isolated from other parts of the structure, making it difficult for electrons to travel along the whole structure. In addition, the orbitals around the HOMO-LUMO gap were typically not as closely spaced in energy compared to the analogous benzenedithiol structure. Similar results were found for hexanedithiol- and decanedithiol-based structures. Lastly, the LUMO/HOMO was found to increase/decrease in going from benzenedithiol (best conductor) to decanedithiol (worst conductor) in Figure 2.23, as expected in Ref. 100, which is consistent with an increasing barrier for electrons.

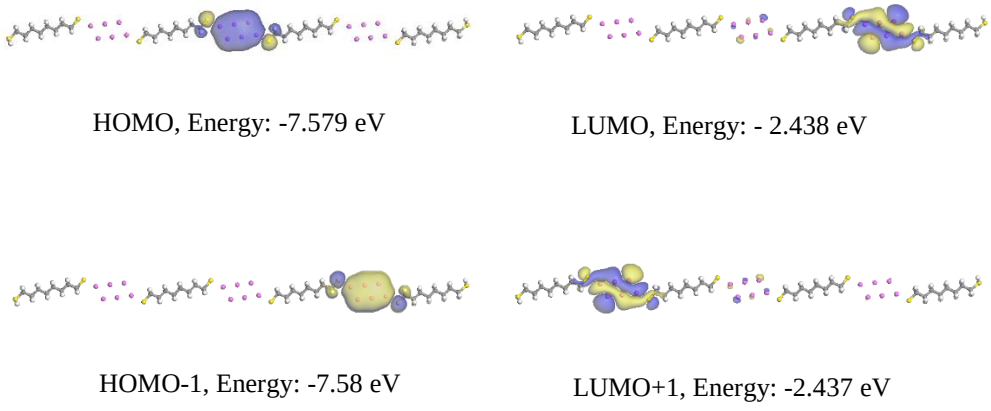

HOMO, Energy: -7.579 eV

LUMO, Energy: - 2.438 eV

HOMO-1, Energy: -7.58 eV

LUMO+1, Energy: -2.437 eV

Figure 2.22 Frontier orbitals ocotanedithiol-Al_6 3-unit chain.

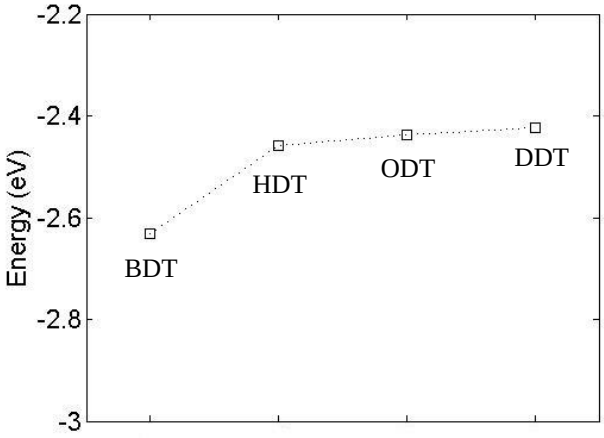

Figure 2.23 LUMO position vs. molecule type for 3-unit chains. From left to right are benzenedithiol (BDT), hexanedithiol (HDT), octancedithiol (ODT), and decanedithiol (DDT).

2.3.4 Switching Element and Circuit Applications

The metal-molecular networks studied in this work provide several possibilities for applications in nanoelectronics as molecular-scale switches and logic circuits. Analogous to electron waveguide devices [101] such as the Y-branch switch [102], we illustrate a potential switching element in Figure 2.24 (a) based on the benzenetrithiol-Al_6 Y-shaped network. The electron-wave Y-branch switch uses a control voltage from the gate to guide the incoming electrons between two drain leads. In our configuration a lateral electric field (e.g., via a gate electrode) is used to deflect an incoming current between the two arms or drain leads of the Y-branch structure. The electric field from gate changes the energy of the incoming electron so that the electron is deflected to hop from the incoming branch to the output branch since the spatial distribution of the orbital occupied by the electron is switched from one branch to another. It has also been shown that such switching is possible by applying a potential difference between the drain arms, i.e.,

without external gates and such behavior may allow significant gain and potentially THz operation with proper biasing schemes [103].

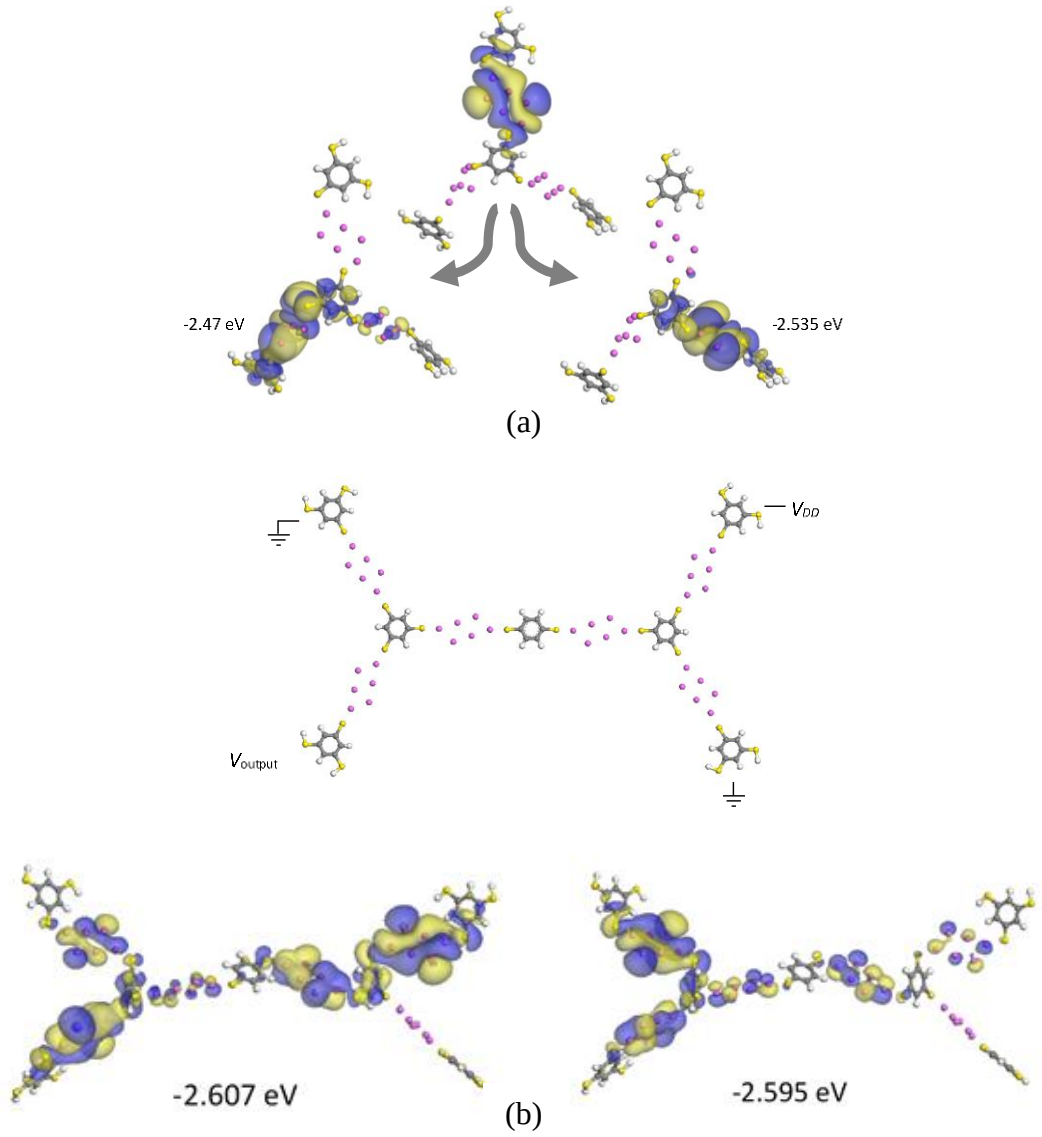

Figure 2.24 (a) Switching element based on Y-shaped molecular network. Application of a lateral electric field effects switching of the incoming current between the two branches (orbital energies indicated). (b) Molecular network consisting of two Y-shaped structures (unrelaxed structure). A first-order implementation of a logical inverter is shown with biasing configuration. Simulation results show example where for low gate voltage output is V_{DD} (top image), whereas switching to a higher energy orbital gives output as ground (bottom image).

In addition to individual devices, one can also consider larger molecular networks for logic gates and circuits. For example, in Figure 2.24 (b) we show two Y-shaped networks coupled to each other via a benzenedithiol molecule that can operate as a simple logic inverter. By changing the external electric field, the electron transport path between V_{DD} and output would be switched ON and OFF by switching between two orbitals with different spatial distribution. Such Y-branches can be used to implement logic functions such as NAND and NOR for different biasing configurations [104]. Power dissipation for electron wave devices is estimated to be quite low with switching energies often just tens of meV [105], which is consistent with our calculations.

2.4 Conclusion

Semi-empirical calculations were performed on benzenedithiol molecules, Al_6 clusters and several nanoscale hybrid molecular structures built from the two components. HOMO-LUMO gaps of benzenedithiol-Al_6 cluster chains/networks decrease several eV compared to the isolated molecule. HOMO-LUMO gaps of benzenedithiol molecular chains show a decreasing trend with respect to the structures' length, which originates from the increasing HOMO energies and decreasing LUMO energies, indicating a decreasing barrier for electrons. The orbital spatial distributions are either well-delocalized or overlapping with close energy levels to form electron transport paths. The benzenedithiol-Al_6 cluster networks can be potentially used for implementation of electron-wave Y-shape branch devices. The work in this chapter was partially presented at two conferences [41, 43, 44] and one journal paper [46] is under preparation.

Chapter 3 Self-Assembled Nanoparticle Molecular Networks

We used an inexpensive solution based method to fabricate self-assembled gold nanoparticle-molecular networks, whose electrical properties can be controlled and modified by using different molecules and changing the ratio of molecules to particles inside the network geometry.

3.1 Self-assembled Nanoparticle Layers

Bethell and his coworkers prepared self-assembled gold nanoparticle monolayers onto a solid substrate using dithiols as the spacer units [106]. Their method originated from the idea of replacing the thiol molecules with dithiol spacers in the process of synthesizing gold nanoparticles with narrow size distributions. Certain three dimensional materials were fabricated by adding small amount dithiols into the red colloidal gold solutions synthesized in absence of thiols. Transmission electron microscopy (TEM) images showed the nanoparticles were ordered into chains and globular supramolecular structures, as shown in Figure 3.1. The size of the gold nanoparticles was around 8 nm in diameter and the precipitated gold nanoparticle-containing material were stable in the air under ambient conditions.

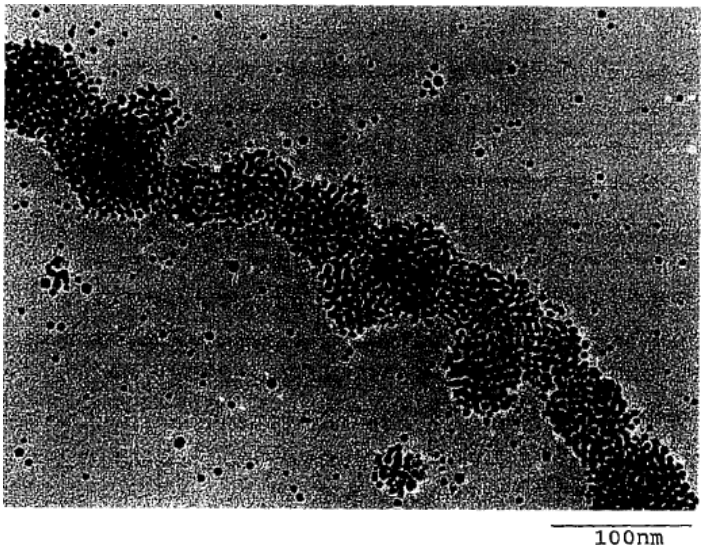

Figure 3.1 TEM image showing self-assembled gold nanoparticles after attached with nonanedithiol (adapted from Ref. 106).

In addition, a layer-by-layer procedure was also mentioned in Ref. 106 to fabricate hybrid self-assembled layers of gold nanoparticles and dithiol linkers on a glass substrate, as illustrated in Figure 3.2. The surface of the glass slide was first derivatized by being treated with 3-mercaptopropyl-trimethoxysilane followed by iterations of being immersed into either colloidal gold solutions or dithiol solutions. Measurement on the resistivity of the gold-dithiol multilayers parallel to the glass surface revealed the effect of the alkanedithiols' methylene unit numbers: 6 to 7 Ω for hexanedithiol; 80 to 90 Ω for nonanedithiol; 1400 to 1600 Ω for dodecanedithiol, which was consistent with the fact that methylene unit numbers played an important role in determining alkanedithiols' conductance.

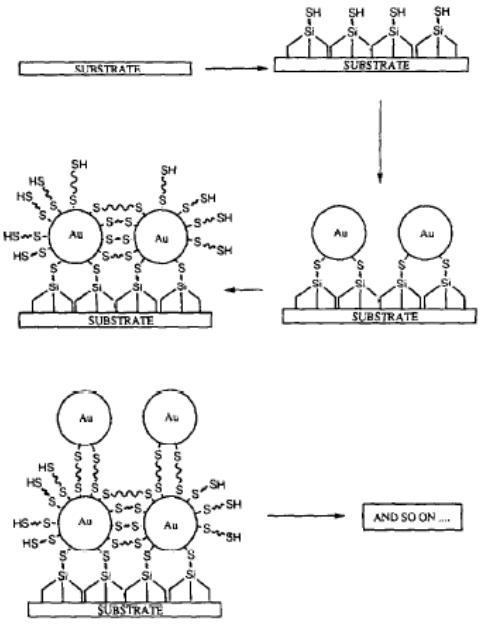

Figure 3.2 Schematic of the layer-by-layer method of fabricating nanomaterials of gold nanoparticles and dithiols (adapted from Ref. 106).

Ref. 37 used a similar approach introduced in Chapter 1: Self-assembled gold-dithiol monolayers were deposited onto interdigitated electrodes with a gap of 2 μm on silicon substrate. (see Figure 3.3).

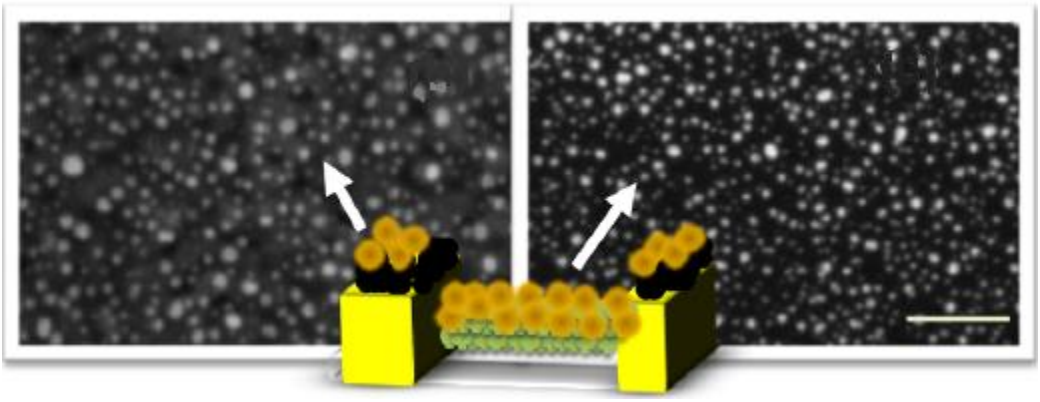

Figure 3.3 SEM images of: left image - gold substrate covered with gold nanoparticle-hexanedithiol monolayer; right image – monolayer on silicon substrate. Scale bar is 100 nm. (adapted from Ref. 37)

3.2 Nanoparticle Oligomers

The oligomer approach provides an accurately controlled way of contacting a few molecules. As introduced in Chapter 1, Bar-Joseph and his coworkers reported their method of fabricating single molecule contact by synthesis of dimer structures of colloidal gold nanoparticles [38]. The synthesis of gold nanoparticle dimers was done by mixing a solution of dithiol molecule with a colloidal gold solution, which was stabilized using the conventional citrate method. However, if more than one molecule were attached to a gold particle, trimer, tetramer and other higher oligomer structures could be formed, as shown in Figure 3.4. In order to ensure the success of fabricating dimer structures, the concentration of the molecule versus the colloidal gold particles was kept to be 1:10 to make sure that there were much fewer molecules than the gold particles. The dimers were separated from the monomeric particles and higher oligomers by centrifuging in a sucrose density gradient.

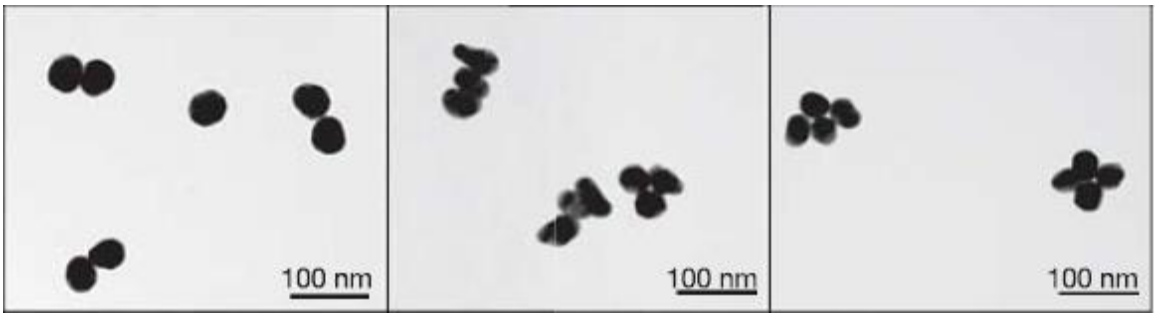

Figure 3.4 Dimer, trimer and tetramer structure of 50 nm colloidal gold particles (adapted from Ref. 38).

As can be seen in Figure 3.5, the SEM image shows a higher magnification of the dimer structure, which shows that the gap between the two particles is well distinguished and the size is in agreement with the size of the dithiol molecule, around 1 nm. The dimer

was located between two electrodes using the electrostatic trapping method based on the dipole-dipole interaction of the electrodes and colloids in order to measure the conductance of the single dithiol molecule bridged in between.

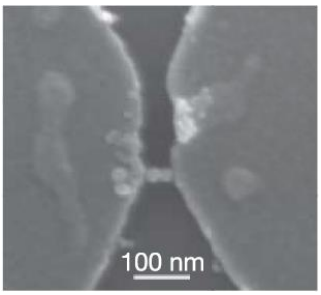

Figure 3.5 SEM image of a dimer trapped between two gold electrodes (adapted from Ref. 38).

Besides measuring conductance of single molecules, the dimers can also be used for quantum information operations [107], which stems from its ability to confine an electron in a limited region as well as to detect and monitor the electron's presence through the Coulomb blockade behaviour seen in Figure 3.6.

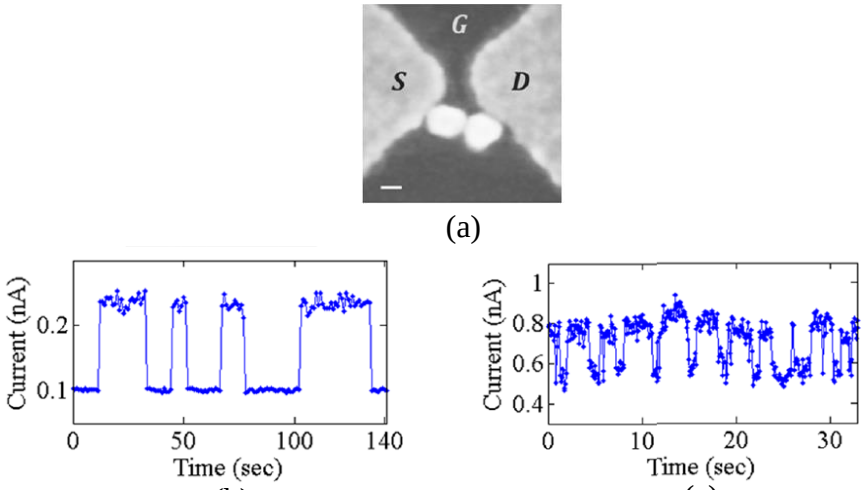

Figure 3.6 (a) SEM image of a trapped dimer structure; Random telegraph signal of the current flowing through the dimer (b) at V_{SD} = 18 mV, V_G = 0 mV and (c) at V_{SD} = -16 mV, V_G = -400 mV. (adapted from Ref. 39).

The two approaches introduced above represent the two extremes of the structures involved with gold nanoparticles and dithiol molecules: the first approach fabricates close-packed layers of molecule-covered nanoparticles in a broad area and measures the conductance property of the molecules in an averaged manner; the second approach fabricates well-defined molecular junctions of a few molecules using the gold nanoparticle dimers, by which the conductance of the single molecule can be well characterized. Our motivation arises from the question of what are the structures that lie between these two extremes. The structures we fabricated are of an "intermediate" size: not small oligomers of nanoparticles or either networks of particles fully covered by molecules – they are actually small aggregates of nanoparticles with a few molecules interconnecting. From these nanoscale networks, we are able to associate the measured data with the networks' size and topology.

3.3 Fabrication and Characterization Methods

3.3.1 Introduction of In-solution Fabrication Method

Our fabrication method is an extension of the in-solution recipe of Ref. 38. Our recipe basically follows the main procedures but changes the ratio of the concentration of colloidal gold nanoparticles versus the dithiol molecule linkers to control molecular connections in order to make larger molecular network structures rather than just small oligomers.

3.3.2 Details of Recipe

1, 6-hexanedithiol (96%), 1, 9-nonanedithiol (95%), 1-octanethiol (97%), 1-hexanethiol (99%), 1, 4-benzenedithiol (99%), and 30 nm citrate stabilized colloidal gold nanoparticles were purchased from Sigma Aldrich. NaOH solution and pure ethanol were used as solvents both for colloidal gold and molecules. Deionized water was used in all the experiments.

The substrates were made of an array of patterned interdigitated gold electrodes which were deposited on Si substrate with a layer of SiO_2 on top using photolithography. The gold electrodes were 35 nm in thickness on top of a 5 nm thick Ti layer. The gaps between electrodes are in the range of 1-2.5 μm.

The fabrication procedure is presented in Figure 3.7. Initially, we used 1 mM NaOH as solvent for dissolving thiol/dithiol molecule and later changed to use ethanol as solvent because of it better solubility. To begin with, thiol/dithiol molecules were dissolved in solvent and then the solution was then stirred on a VWR hot plate magnetic stirrer for about 5 minutes at 300 rpm. A centrifuge tube filled with 1.25 mL of colloidal gold solution was centrifuged at 9.8×10^3 g for 5 minutes, post which the supernatant was discarded using a micropipette. This was followed by filling the centrifuge tube with 1.25 mL of 1mM NaOH solution. The precipitate was resuspended by handshaking and then centrifuged once again. The same procedure was repeated for the third time with an exception that after centrifuging and removing the supernatant, the precipitate was suspended in 0.25 mL of NaOH. This resulted in obtaining concentrated colloidal gold

solution in NaOH. This solution was then mixed with an equal volume of thiol/dithiol solution in 1 mM NaOH and incubated at 4 °C for 24 hours. In other words, the ratio of $N_{thiol/dithiol}$: $N_{particle}$ was 1:1. In order to study the effect of variation of $N_{thiol/dithiol}$: $N_{particle}$ ratio in the experiment, we repeated the above synthesis procedure by adjusting the ratio of $N_{thiol/dithiol}$: $N_{particle}$ to 5:1.

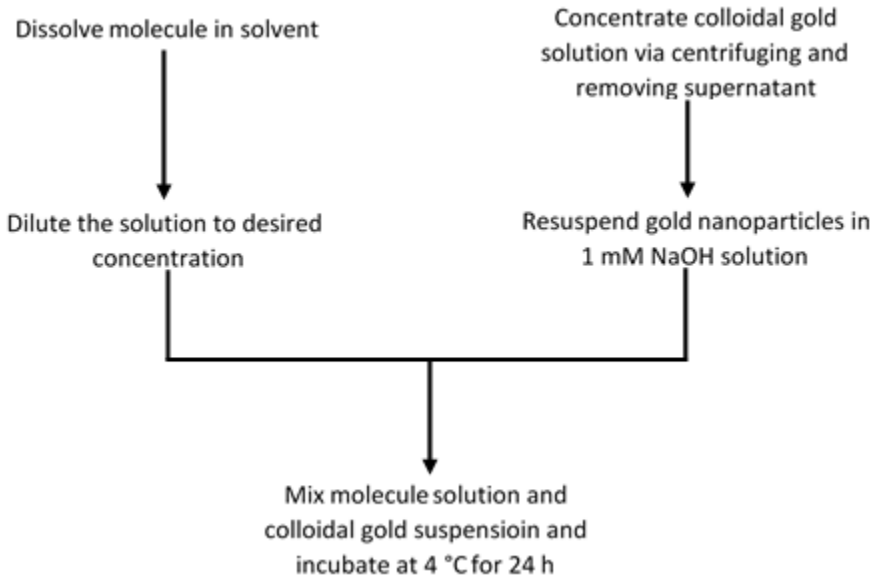

Figure 3.7 Fabrication procedure.

The solution mixture of colloidal gold particles and thiol/dithiol molecules was incubated at 4 °C for 24 hours and then deposited onto clean substrates (substrates were first rinsed with acetone, isopropanol and deionized water and then dried using nitrogen gas) and dried in ambient condition. These substrates were then used for electrical measurements. Figure 3.8 shows that the solution after incubation is well dispersed.

Figure 3.8 Mixture solution of 1, 9-nonanedithiol and colloidal gold particle with ratio $N_{thiol/dithiol}$: $N_{particle}$ = 1:1 after incubation of 24 h.

3.3.3 Characterization Method and Instruments

Current-voltage (*I-V*) data was obtained by electrical measurements using a Janis probe station which was configured with an electrical characterization system (Keithley 4200). Tungsten probes were used for two-terminal measurements on the particle-network films bridged between the interdigitated electrodes. The morphology of the networked films were studied using Olympus BXFM optical microscopy and Nanonics MultiView 1000 atomic force microscope (AFM) with pulled glass fiber (10 nm in diameter) in non-contact mode. We also probed the conductivity of the structure locally with the help of conducting AFM tip. Conductance of the sample was obtained when the tip was lowered on the film. All the measurement were conducted at room temperature.

3.4 Results and Analysis

AFM images (Figure 3.9) clearly show that the colloidal gold nanoparticle dimers and larger oligomers are formed as presented in Ref. 38 confirming the effect of dithiol molecules acting as linkers between gold nanoparticles. The height of the particle oligomers are around 30 nm, consistent with the diameter of the gold particle. Large

networked films are also observed on the substrates, either in the gap between electrodes or on the large area of gold film.

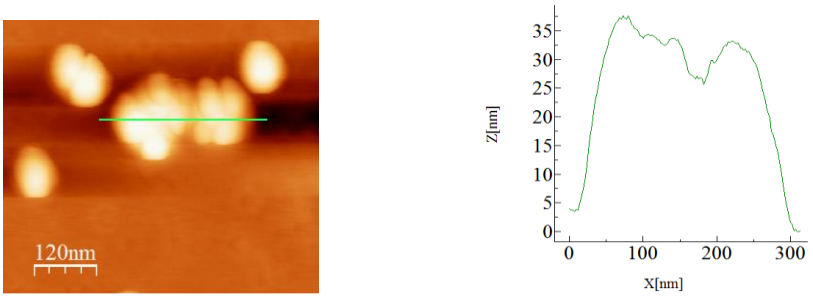

(a)

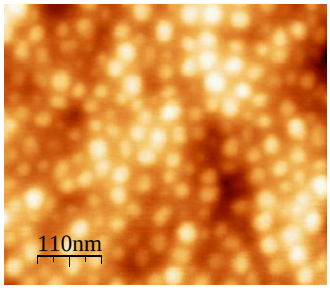

(b)

Figure 3.9 AFM images of (a) gold nanoparticle dimers and larger oligomers; (b) Large networked gold particle film.

3.4.1 Nonanedithiol-Gold Nanoparticle Networks

For the samples with $N_{dithiol}$: $N_{particle}$ = 1:1, the range of the current magnitude varies from 10^{-10} to 10^{-6} A. Several *I-V* plots of different sets are presented in Figure 3.10. Generally speaking the *I-V* curves are quite linear although some curves may also be twisted. The shapes of the measured *I-V* curves are consistent with other works [34, 108]

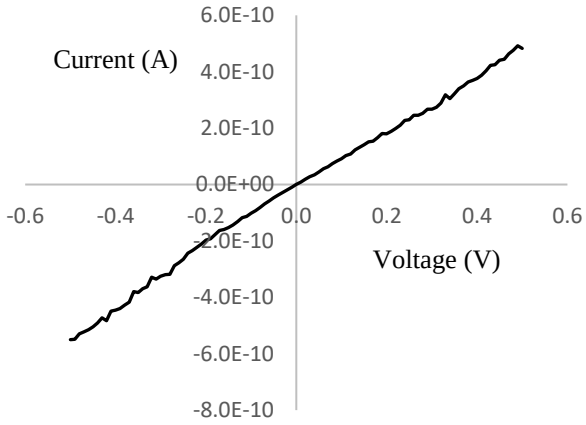

(a)

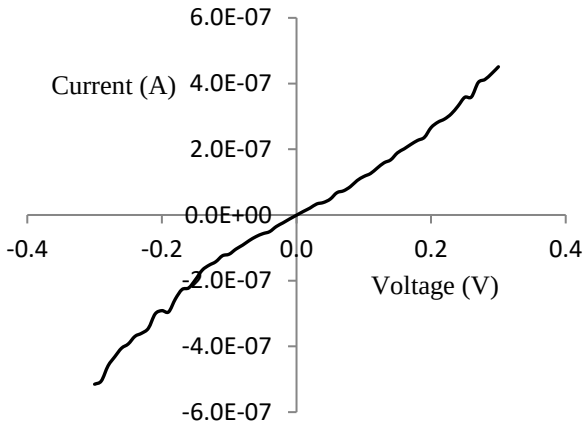

(b)

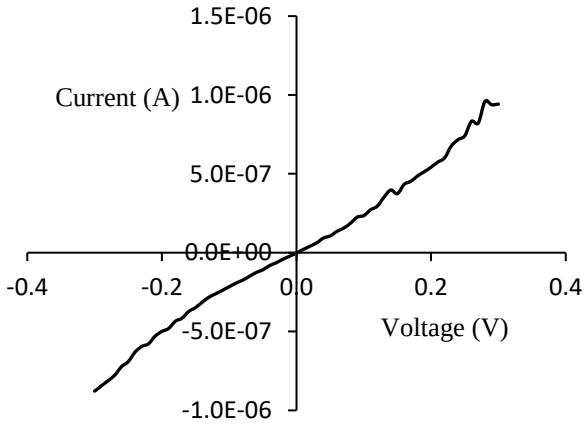

(c)

Figure 3.10 *I-V* plots nonanedithiol sample: (a) (b) (c) represent their respective set.

The set measured with *I-V* curve of Figure 3.10 (c) is shown in Figure 3.11. It can be seen that certain nanostructures built of colloidal gold particle exists between the bottom two

electrodes. The AFM image of Figure 3.11 (b) shows the topology of the structure. An aggregate of gold particles forms a connection between electrodes and the middle part of the aggregate possess a height of 60-70 nm, which indicates it is made of two layers of contacted gold particles, as shown in the cross-section of Figure 3.11 (c).

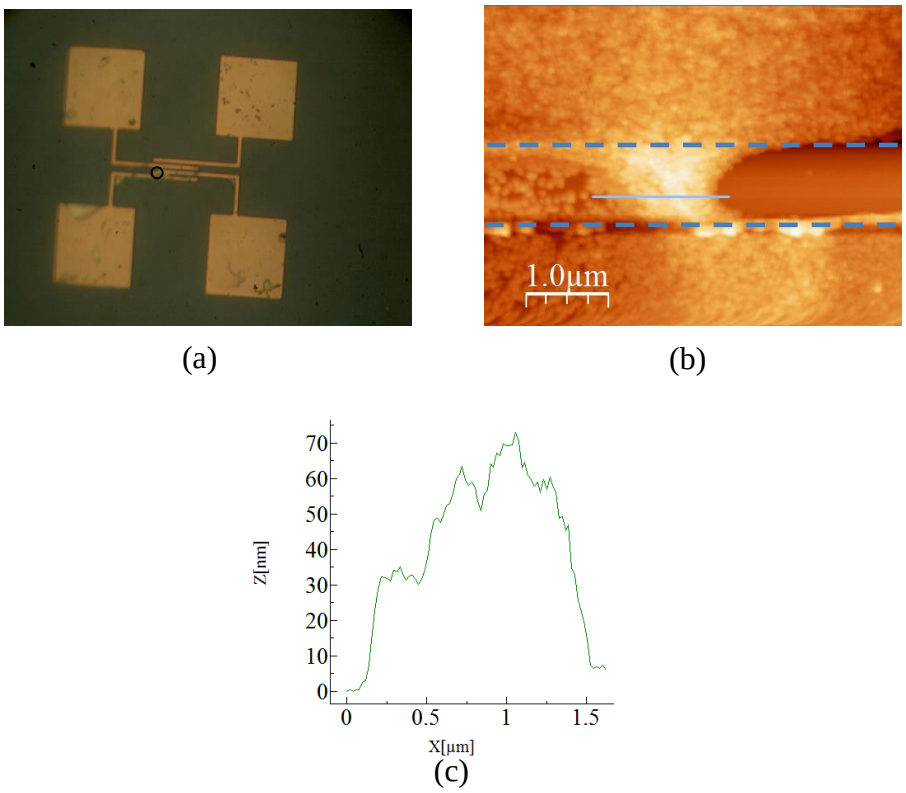

(a) (b)

(c)

Figure 3.11 Nonanedithiol sample: (a) Optical image; (b) AFM image; (c) AFM cross-section contour of the electrode set *I-V* curve Figure 3.10 (c). The cross-section is labeled in (b). The grey dotted line represent edge of electrode.

Similar behavior is seen for samples with ratio $N_{dithiol}$: $N_{particle}$ = 5:1, several sets are measured with significant amount of current passing through and the most measured *I-V* characteristics are linear, as shown in Figure 3.12 (a). The AFM image of Figure 3.12 (c) shows that the nanostructure adopts a cone shape and the height of the narrowest part is around 60 nm, which is also a bilayer of gold nanoparticles.

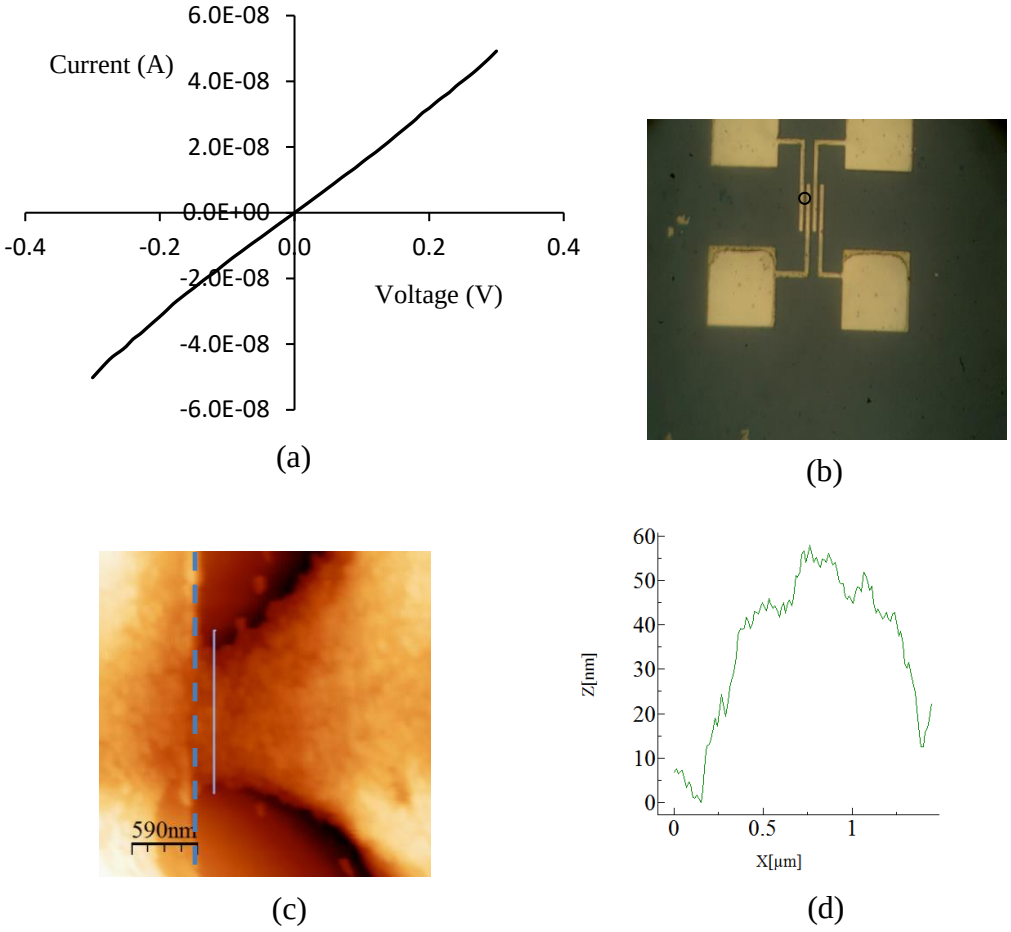

Figure 3.12 (a) *I-V* plot of a nonanedithiol sample; (b) Optical image; (c) AFM image; (d) AFM cross section contour of the nanostructure on one set of the $N_{dithiol}$: $N_{particle}$ = 5:1 sample. Grey dotted line represents edge of electrode.

We also sometimes found nonlinear *I-V* plots on certain sets as in Figure 3.13. The structure has a height of around 200 nm indicating that it is made of multiplayers (around 6 to 7 layers) of gold nanoparticles.

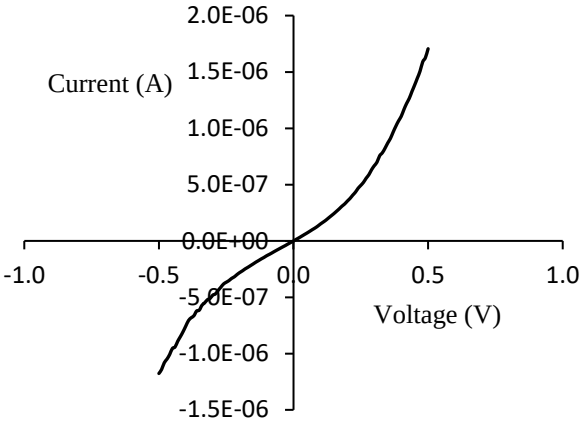

(a)

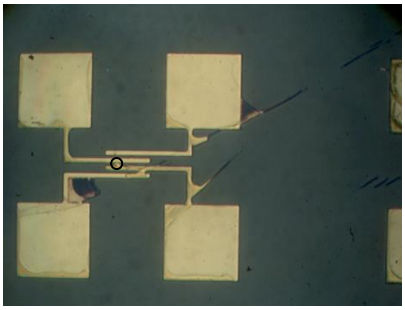

(b)

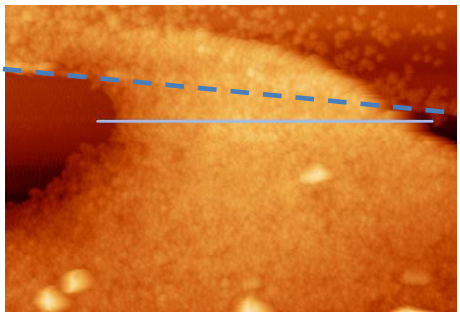

(c)

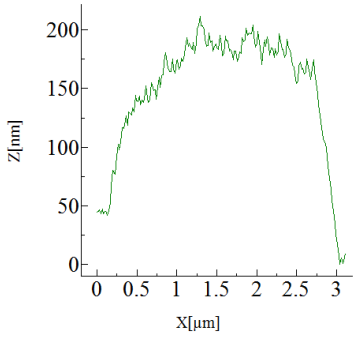

(d)

Figure 3.13 (a) *I-V* plot of a nonanedithiol sample; (b) Optical image; (c) AFM image; (d) AFM cross section contour of the nanostructure on one set of the $N_{dithiol}$: $N_{particle}$ = 5:1 sample with nonlinear *I-V* character. Grey dotted line represents edge of electrode.

For the samples fabricated with ethanol as solvent for nonanedithiol molecules, we also measured linear *I-V* characteristics on both the samples with ratio $N_{dithiol}$: $N_{particle}$ = 1:1 and 5:1, as shown in Figure 3.14.

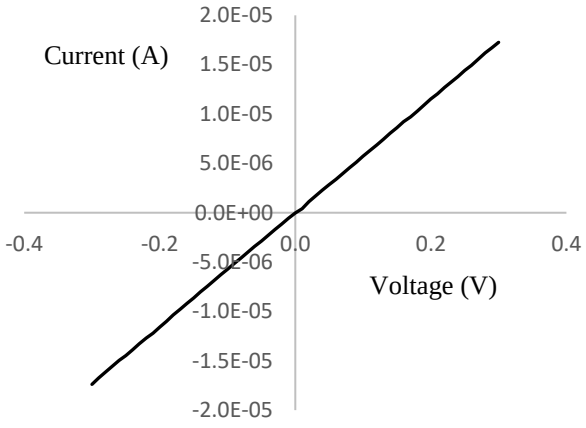

(a)

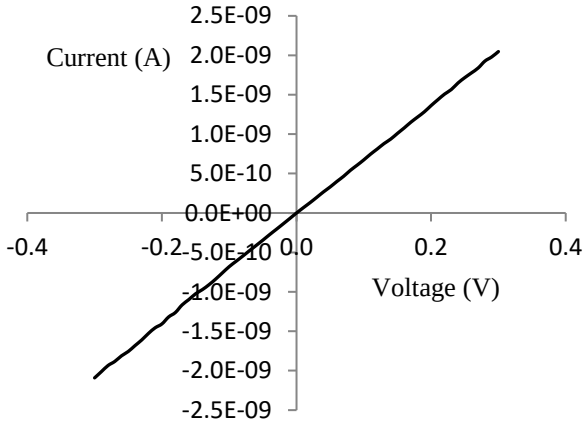

(b)

Figure 3.14 *I-V* plots of nonanedithiol samples: (a) $N_{dithiol}$: $N_{particle}$ = 1:1; (b) $N_{dithiol}$: $N_{particle}$ = 5:1.

3.4.2 Hexanedithiol , Hexanethiol and Octanethiol-Gold Nanoparticle Networks

For comparison, we also fabricated several samples using 1, 6-hexanedithiol molecule as linkers. The measured current-voltage characteristics are also linear *I-V* curves similar to nonanedithiol samples, as shown in Figure 3.15. The *I-V* plot of Figure 3.15 (a) is measured on a ratio $N_{dithiol}$: $N_{particle}$ = 1:1 sample. The resistance of the structures measure is around $2\times10^{9}\ \Omega$. Figure 3.15 (b) is measured from a sample of ratio $N_{dithiol}$: $N_{particle}$ = 5:1, whose resistance is identified around $6\times10^{7}\ \Omega$. Also, like the situation of

nonanedithiol samples, from the samples made using ethanol as solvent for molecules, we measured similar linear current-voltage curves as well, as shown in Figure 3.16.

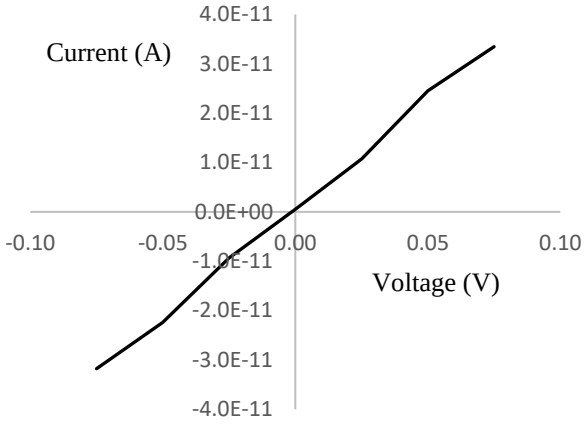

(a)

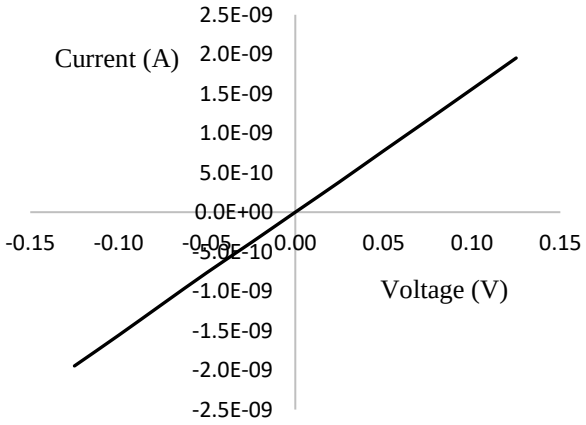

(b)

Figure 3.15 *I-V* character of hexanedithiol samples with ratio (a) $N_{dithiol}$: $N_{particle}$ = 1:1 and (b) $N_{dithiol}$: $N_{particle}$ = 5:1.

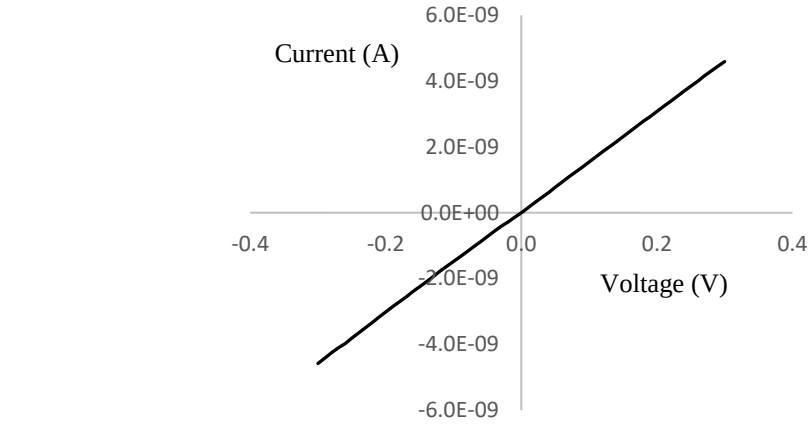

(a)

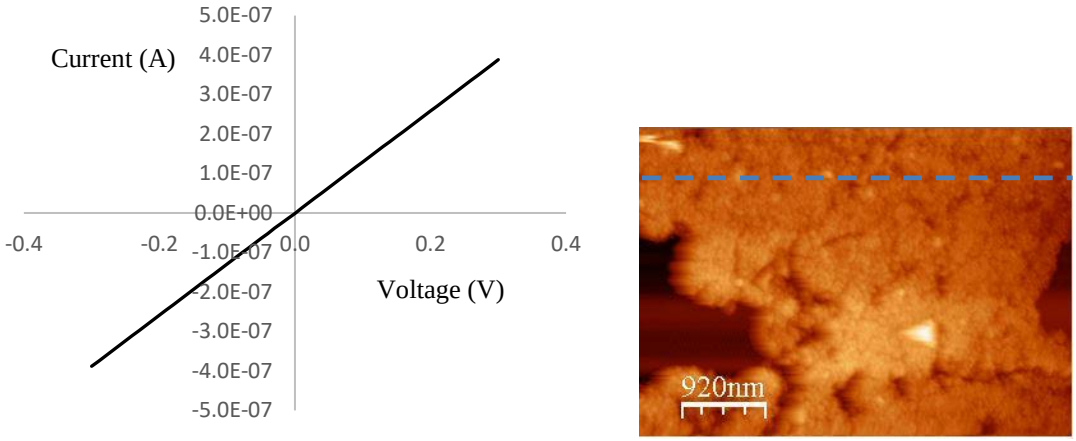

(b)

Figure 3.16 (a) *I-V* plot of hexanedithiol sample with ratio $N_{dithiol}$: $N_{particle}$ = 1:1; (b) *I-V* plot and AFM image of hexanedithiol sample of ratio $N_{dithiol}$: $N_{particle}$ = 5:1. Grey dotted line represents edge of electrode.

Besides nonanedithiol and hexanedithiol, we also fabricated several samples with hexanethiol and octanethiol with the recipe using ethanol as solvent for dithiols. Linear current-voltage plots were measured on several electrode sets on both samples, presented in Figure 3.17, while sometimes we also measured nonlinear *I-V* curves on these samples seen in Figure 3.18.

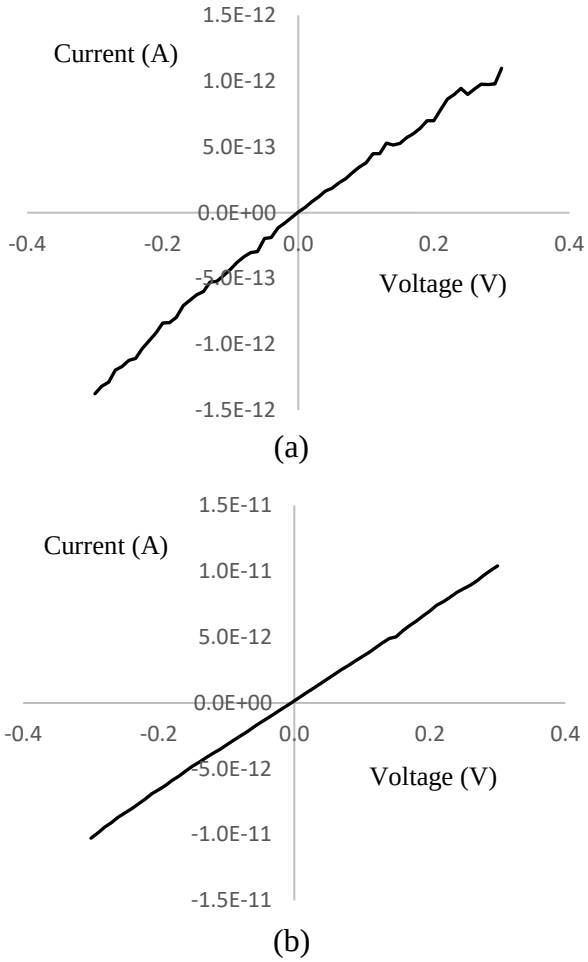

Figure 3.17 *I-V* plots of thiol samples: (a) hexanethiol; (b) octanethiol. Both ratios of $N_{dithiol}$: $N_{particle}$ = 1:1.

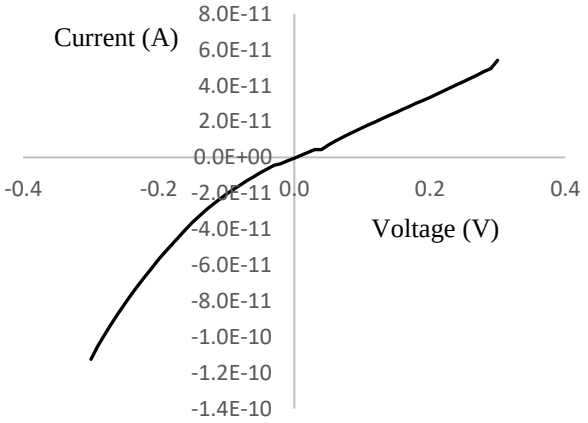

Figure 3.18 Nonlinear *I-V* plots of octanethiol with $N_{dithiol}$: $N_{particle}$ = 1:1.

3.4.3 Benzenedithiol-Gold Nanoparticle Networks

The benzenedithiol samples were fabricated with the recipe using ethanol. Benzenedithiol is a π-conjugated molecule rather than a saturated molecule. Measurements on benzenedithiol samples sometimes indicated linear *I-V* characteristics of the nanostructures, as shown in Figure 3.19, but in the meanwhile we also measured several nonlinear *I-V* curves, as shown in Figure 3.20

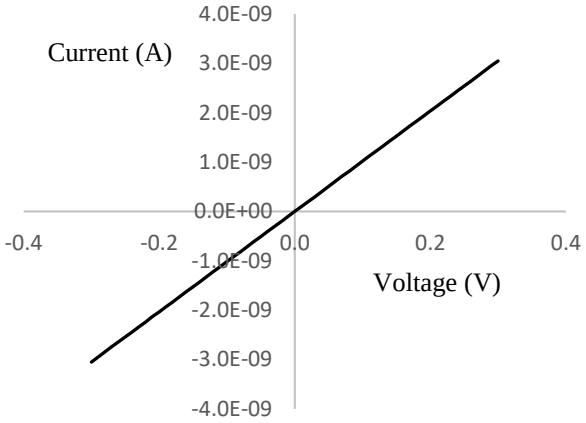

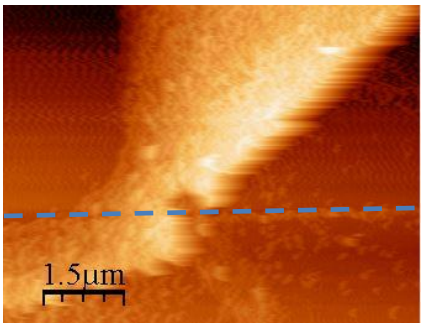

(a)

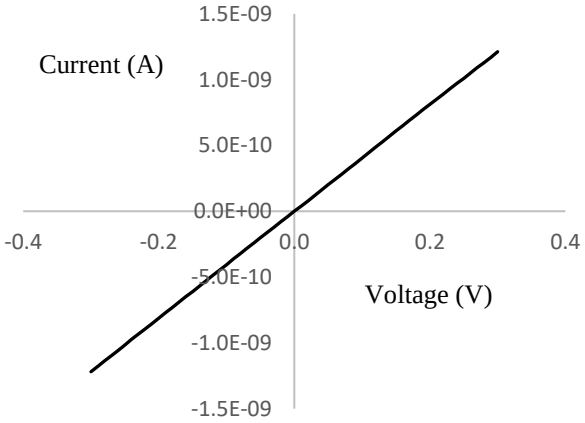

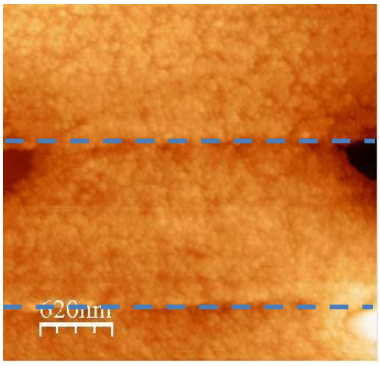

(b)

Figure 3.19 *I-V* plots and AFM images of benzenedithiol sample with ratio (a) $N_{dithiol}$: $N_{particle}$ = 1:1; (b) $N_{dithiol}$: $N_{particle}$ = 5:1. Grey dotted line represent edge of electrode.

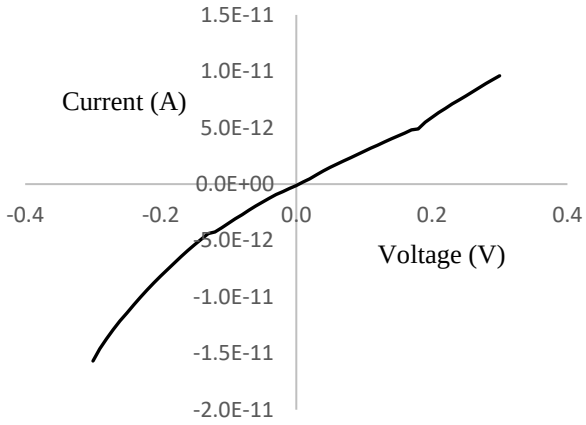

Figure 3.20 Nonlinear *I-V* plot of benzenedithiol sample with ratio $N_{dithiol}$: $N_{particle}$ = 5:1.

3.4.4 Control Samples

Control samples were fabricated without any molecules. The control sample in Figure 3.21 is made by mixing colloidal gold solution with deionized water. The nanostructure shown in Figure 3.21 has a height of over 200 nm at the narrowest part and resides between the bottom electrodes of the set. Another batch of control samples which are made by mixing with ethanol were also synthesized and the measured samples of gold particle networks also showed smooth linear *I-V* characteristics, as shown in Figure 3.22. All control samples displayed linear *I-V* curves.

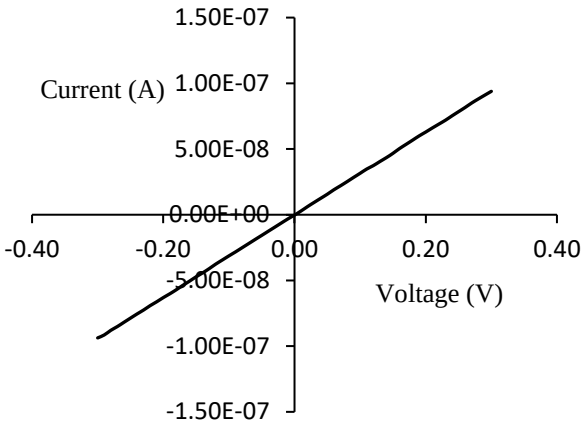

(a)

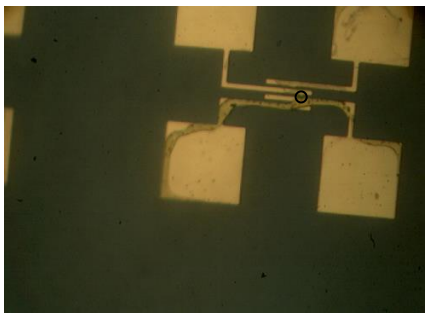

(b)

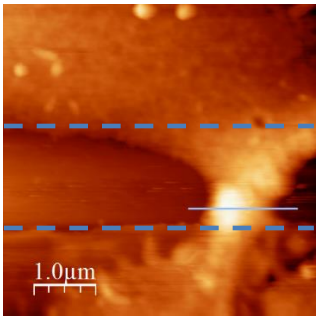

(c)

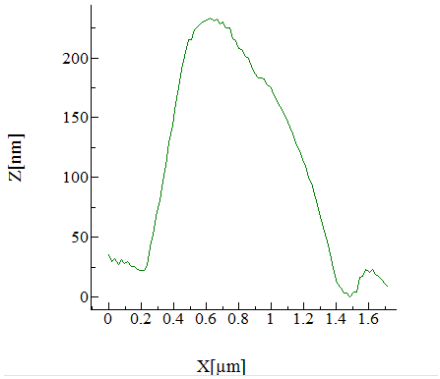

(d)

Figure 3.21 (a) *I-V* plot of control sample; (b) Optical image and (c) AFM image of the structure measured; (d) AFM cross section contour of one nanostructure on control sample. Grey dotted line represents edge of electrode.

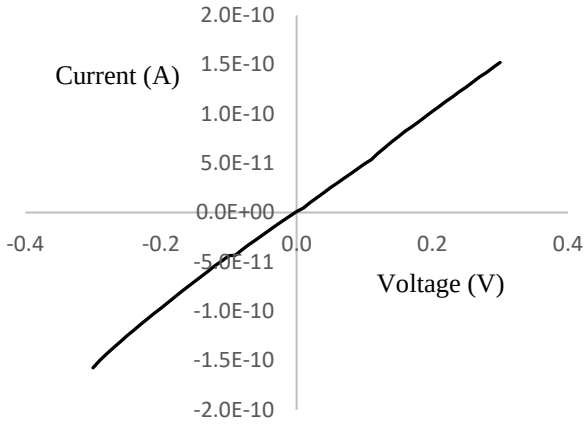

Figure 3.22 *I-V* plots of control sample synthesized by mixing colloidal gold solution with ethanol.

3.4.5 Conducting Tip AFM

A schematic of the conducting tip AFM measurement is presented in Figure 3.23. The materials to be probed are deposited on a conducting gold film, which is connected to ground. The AFM is operated in contact mode with a voltage bias applied on the AFM tip. This method allows one to probe the nanoparticle networks locally, which is focused on the vertical structures formed by gold nanoparticles between the AFM tip and gold substrate. By sampling multiple locations on the network, we measured two distinct resistance ranges either kΩ or MΩ. This implies that within the self-assembled gold nanoparticle-molecular network, there are two types of connections between two neighbouring particles: I. the particles are bridged by an individual dithiol molecule, and II. the two particles are in direct contact with each other, as shown in Figure 3.24.

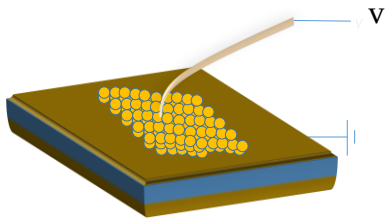

Figure 3.23 Schematic of conducting AFM tip measurement.

Figure 3.24 I. Particles bridged by one single molecule; II. Particles in direct contact.

3.4.6 Data Analysis

The conductance of dithiol/thiol molecules varies dramatically depending on the molecule's structure. For alkanedithiol\thiol molecules, conductance will decrease exponentially vs increasing number of methyl units [34, 97, 109], while the π-conjugated molecule benzenedithiol is typically more conductive than alkanedithiol/thiols [65]. Reference data of conductance of a number of molecules are shown in Table 3.1.

Table 3.1 Conductance of dithiol molecules, where G_0 is the quantum conductance [34, 110–112].

Molecule	Conductance (G_0)
Hexanedithiol	1.2×10^{-3}
Octanedithiol	2.5×10^{-4}
Decanedithiol	2×10^{-5}
Hexanethiol	1.6×10^{-4}
Octanethiol	8.7×10^{-5}
Benzenedithiol	2.5×10^{-3}

In the ideal case that there is a single molecule bridging between neighbouring particles, as shown in Figure 3.25 (a), the topology of the network is a periodic structure consisting of hexagonal unit. However, in real situations, most likely a topology of the network is that both molecular contact and direct gold contact exist in the network, as in Figure 3.25 (b) and this can explain the two distinct resistance range measured by conducting AFM tip method. When the vertical region between AFM tip and gold substrate is interconnected by dithiol molecules, then the low conductance of the molecule would increase the overall resistance and, when the region is just a group of gold particles compiled together, the resistance should mainly be the contact resistance between neighbouring gold particles.

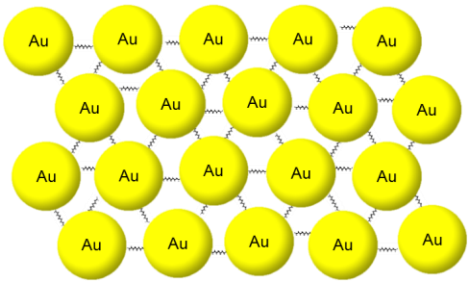

(a)

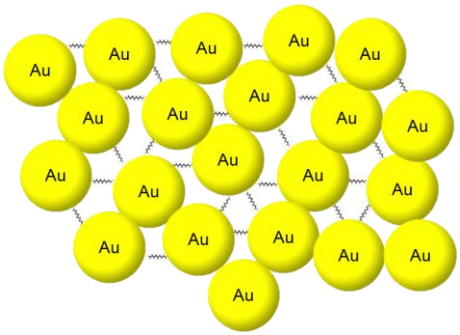

(b)

Figure 3.25 (a) Neighboring gold particles are always bridged by a single molecule; (b) Situation where both molecular contact and direct gold contact exist in the network.

To associate the molecular conductance with the measured current-voltage characteristics of the networks between electrodes. We abstract the molecular contact to a linear resistance element and quantum conductance 12907 Ω for the direct gold-gold particle contact. Then the topology of the network can be simplified to a lattice made of linear resistors. In a simple model the network can be simplified into a group of multiple sequential resistors in parallel, as shown in Figure 3.26. The overall conductance of the network can then be estimated as $\frac{\text{Number of particles in parallel}}{\text{Number of particles in sequence}} \times$ Number of particle layers $\times\, G_{mol} = \frac{WN}{L} G_{mol}$, where L and W are the length and width of the network, N is the number of nanoparticle layers and G_{mol} is the conductance of the single molecule or the quantum conductance for control sample, since the number of particles in sequence = $\frac{\text{Length of network}}{\text{Particle's diameter}}$ and so is the number of particles in parallel. This formula relates the structure dimensions with the dithiol molecules conductance and gives an approximate estimation of the network's conductance. Table 3.2 shows a certain degree of agreement between the estimated and measured conductance.

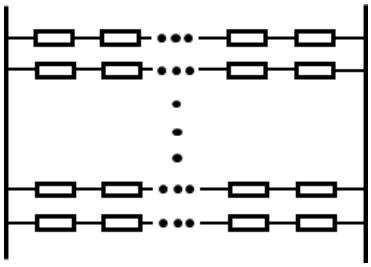

Figure 3.26 Simplified model of multiple sequential resistors in parallel.

Table 3.2 Comparison between estimated and measured conductance of the fabricated nanostructures according to the simplified model in Figure 3.26.

Sample	Dimensions	Estimated conductance (S)	Measured conductance (S)
Nonanedithiol with ratio 1:1 (Figure 3.11)	Length (nm): 200 Width (nm): 1000 Height (nm): 70	1×10^{-8}	2.5×10^{-6}
Nonanedithiol with ratio 5:1 (Figure 3.12)	Length (nm): 200 Width (nm): 1000 Height (nm): 50	1×10^{-8}	1.6×10^{-7}
Nonanedithiol with ratio 5:1 (Figure 3.13)	Length (nm): 150 Width (nm): 3000 Height (nm): 200	1.4×10^{-7}	1.8×10^{-6}
Nonanedithiol with ratio 5:1 (Figure 3.14(b))	Length (nm): 800 nm Width (nm): 1000 nm Height (nm): unknown	1.3×10^{-9}	7.1×10^{-9}
Hexanedithiol with ratio 5:1 (Figure 3.15(b))	Length (nm): 1000 Width (nm): 2500 Height (nm): 50	5×10^{-7}	1.6×10^{-8}
Hexanedithiol with ratio 5:1 (Figure 3.16(b))	Length (nm): 1500 Width (nm): 3500 Height (nm): 150	3×10^{-7}	1.3×10^{-6}
Hexanethiol with ratio 1:1 (Figure 3.17(a))	Length (nm): 1500 Width (nm): 2000 Height (nm): 60	3.1×10^{-8}	4×10^{-12}
Octanethiol with ratio 1:1 (Figure 3.17(b))	Length (nm): 500 Width (nm): 500 Height (nm): unknown	6.7×10^{-9}	3.3×10^{-11}
Benzenedithiol with ratio 1:1 (Figure 3.19(a))	Length (nm): 1000 Width (nm): 1000 Height (nm): 200	9.1×10^{-7}	1.4×10^{-8}
Benzenedithiol with ratio 5:1 (Figure 3.19(b))	Length (nm): 500 Width (nm): 500 Height (nm): 30	1.9×10^{-7}	4.2×10^{-9}
Control (Figure 3.21)	Length (nm): 600 Width (nm): 1000 Height (nm): 200	8.6×10^{-4}	3.2×10^{-7}

3.5 Circuit Modeling

3.5.1 Gold Nanoparticle-Molecular Network Model

The multiple sequential resistors in parallel model discussed in the last section assumed all neighboring gold particles are bridged by a single dithiol molecule in between and omits the lateral coupling between neighbouring particles. For more accurate simulations, we abstract the structure into a general network of interconnected resistors.

The unit cell in the nanoparticle network is a hexagon (Figure 3.27), which is that each particle has six nearest neighbors. By abstracting the nearest contacts into resistors, the total network is converted into a lattice of resistors as shown in Figure 3.27. As for a circuit implementation, the hexagonal unit cell is converted into vertical and horizontal lines, as shown in Figure 3.28. The yellow lines represent nanoparticles and each one has six nearest neighbors.

We used LTspice, a software implementing a SPICE simulator of electronic circuits produced by Linear Technology (LTC)[1], to implement and simulate our circuit model of the nanoparticle networks. We started from building a subsection of the circuit that consisted of 36 resistors as a building unit. Then the whole network was built by copying over the building block until wanted dimensions. The contact resistance between gold electrodes and gold nanoparticles is set as 0.55 Ω assuming that the contact region of particles is deformed to be a cylinder shape. The resistors in the building block were parameterized with unique variables, R_1 to R_{36}, and in this way we were able to tune the

[1] Linear Technology's website: http://www.linear.com/

ratio of the number of molecule contacts versus gold contact. In the beginning, all the variables were as gold contact (12907 Ω) and we wrote a python program (see in Appendix D random variable generator) for generating a random set of variables to be changed. The random variable generator will assign a resistor in the unit cell to be set as one of two values – either gold contact resistance (12907 Ω) or the molecule's resistance in a random manner for each ratio (number of molecular contacts versus gold contacts). Thus for each ratio (molecular contact versus gold contact) the configuration (or position) of the resistors are randomized within the unit cell so as to reduce the influence of the resistor configuration in calculating the whole network's resistance. Since the specific combination of random variables affects the resistance of network simulated, we calculate the resistance of the network three times for each ratio point (i.e., three random configurations). In this way, we could observe the correspondence between the resistance of the whole network and the percentage of the molecular resistance in the network statistically. The resistances of molecule used in the circuit modelling are listed in Table 3.1.

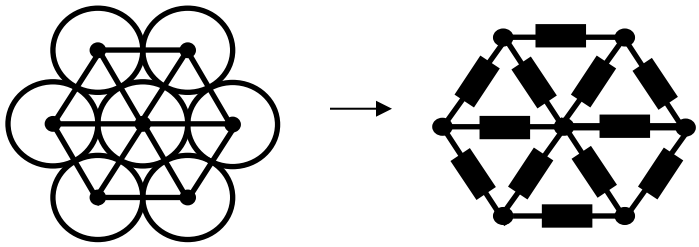

Figure 3.27 Abstraction of particle connections to linear resistive elements.

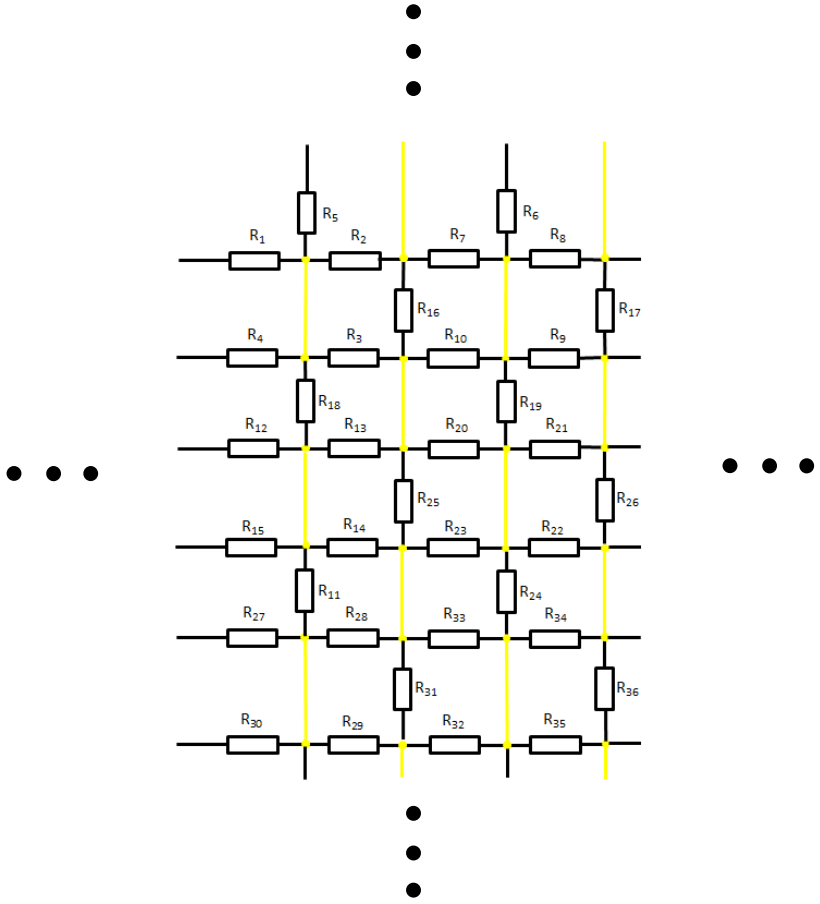

Figure 3.28 Building block of the circuit model. The yellow lines represent nanoparticles and each one has six nearest neighbors.

3.5.2 Results of LTspice Simulations

The AFM image of Figure 3.16 (b) shows a hexanedithiol network ($N_{dithiol}$: $N_{particle}$=5:1) with length 1500 nm, width 3500 nm and height 150 nm. Hexanedithiol's resistance is set as 10^7 Ω and the calculated resistances of the whole network ranges from 3.2×10^3 Ω with only gold contact resistance to 2.5×10^6 where all the contacts between particles are treated as hexanedithiol molecule's resistance. The plot of network's total resistance versus the percentage of molecular contact is presented in Figure 3.29 and each ratio point is sampled three times with randomly generated variables set as gold contact

resistance. The actual resistance of the network is measured to be $7.6\times10^5\,\Omega$, which falls around 60-70% of molecular contact in the network.

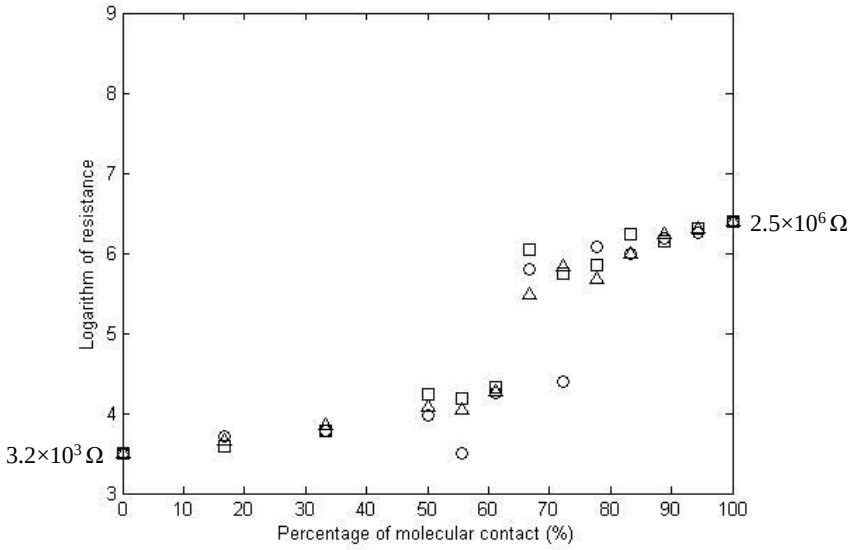

Figure 3.29 Logarithm base 10 of resistance of hexanedithiol network (Figure 3.16(b)) versus percentage of molecular contact in the network. Circle, triangle, and square correspond to three trials of simulation.

One issue important to mention is that this circuit model is assuming that all the nanoparticles are closely packed, i.e. all neighboring particles are either connected by a molecular contact or gold contact. However, the real situation is complicated: in the nanoparticle network, “defects” can exist where neighboring particles are not connected at all or for certain region there are no particles. As shown in Figure 3.30, the nanoparticles can be seen clearly and there several gaps existing in the network (the darker regions), which means the network is only partially connected (the bright region in the middle). These defects should be considered as large values for resistance variables and will increase the overall resistance of the network greatly, which will discussed with details in the following.

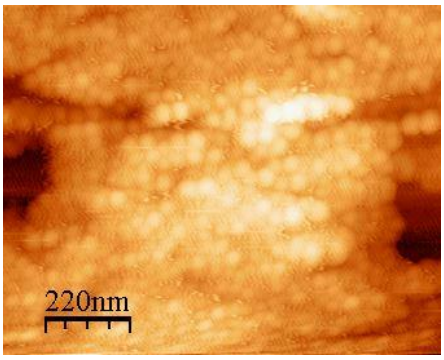

Figure 3.30 Nanoparticle network with several defect regions.

For the benzenedithiol samples in Figure 3.19, the dimension of Figure 3.19 (a) is 1000 nm both in length and width and 150 nm in height. Since the dimension of 1000 nm × 1000 nm is close to the calculation limit of the normal computer we used, we roughly reduced the dimension to 500 nm × 500 nm for circuit modeling. However, for Figure 3.19 (b), from the AFM image it is seen that there are several defect regions near the contact with electrodes, so the effective width of the network is actually much narrower than shown in the image, which we estimated as 500 nm. The length is also estimated to be 500 nm and the structure is one layer of particle thick on average, which is 30 nm in height. Thus one circuit model of 500 nm × 500 nm is used to simulate both samples and plot of network's total resistance versus the percentage of molecular contact is presented in Figure 3.31. The resistance of benzenedithiol used in the modeling is $5.3\times10^{6}\,\Omega$.

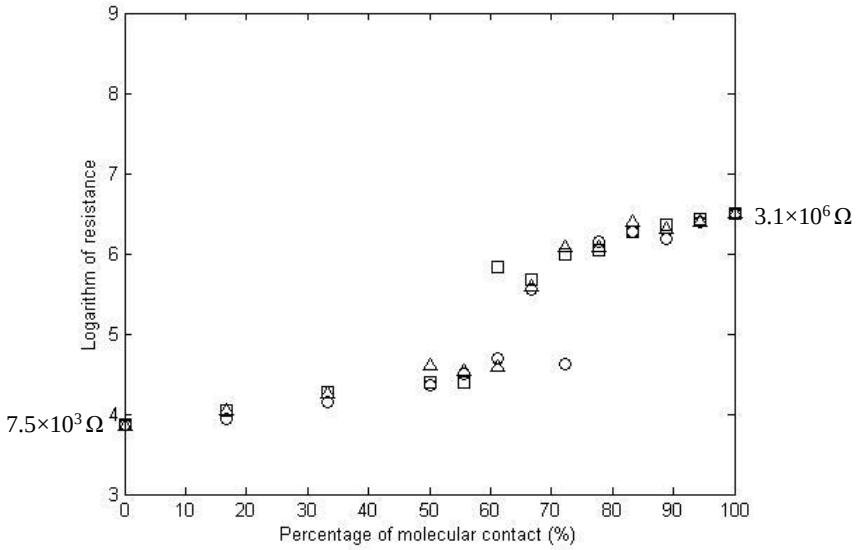

Figure 3.31 Logarithm base 10 of resistance of benzenedithiol networks (Figure3.19) versus percentage of molecular contact in the network. Circle, triangle, and square correspond to three trials of simulation.

The measured resistance of Figure 3.19 (a) is $7.1\times10^7\ \Omega$ and for Figure 3.19 (b) it is $2.4\times10^8\ \Omega$: both of them are above the upper bound of simulated resistances $3.1\times10^6\ \Omega$. There are several factors that can explain this offset. First of all, the resistance of benzenedithiol molecule used $5.3\times10^6\ \Omega$, which is a value usually measured a low temperature. Since our measurement is conducted at room temperature, the actual resistance of benzenedithiol molecule can be higher [113], which is probably caused by scattering effect at higher temperature, and this contributes to an higher overall resistance of the network. A contact resistance between benzenedithiol molecule and gold nanoparticle is likely to exist in our measurement but is omitted in our circuit model due to the difficulty to estimate its effect. Thirdly, the circuit model is actually simulating networks of one single layer in height but actually for sample of Figure 3.19 (a) the structure is about 5 layers of particles thick, which is another uncertainty in the modeling.

Lastly, as shown Figure 3.19 (b), it is quite possible that there are several defects inside the network. The defects should be modeled as very large resistances in the circuit model and their presence will increase the overall resistance of the network. All of these uncertainties can explain the 20 to 100 times off between measured values and simulated values.

One more thing worth mentioning is that sample of Figure 3.19 (a) has $N_{dithiol}$: $N_{particle}$ ratio 1:1 and Figure 3.19 (b) has $N_{dithiol}$: $N_{particle}$ ratio 5:1, and the measured resistance of Figure 3.19 (b) is around 5 times higher than Figure 3.19 (a) although they have the same ratio of length to width. This can be associated with the different $N_{dithiol}$: $N_{particle}$ ratios of both samples – Figure 3.19 (b) (5:1) contains more molecules than Figure 3.19 (a) (1:1), which again illustrates the applicability of our circuit model and the ability to effectively tune the network's electrical properties.

Although there are uncertainties in the circuit model, generally speaking the circuit modelling is consistent with the measured data. The nonanedithiol sample ($N_{dithiol}$: $N_{particle}$=5:1) measured as shown in Figure 3.14 (b) is an example: The dimension of the network is estimated to be 800 nm long and 1000 nm wide. The measured resistance 1.4×10^8 Ω is very close to the calculated resistance 1.5×10^8 Ω (averaged value by sampling three times) at molecular percentage of around 70%. By comparing with the hexanedithiol sample ($N_{dithiol}$: $N_{particle}$ ratio 5:1) in Figure 3.16 (b), we can see how the resistance of the type of molecule can affect the overall resistance of the network: Nonanedithiol possesses a higher resistance (10^9 Ω) than hexanedithiol (10^7 Ω). The

hexanedithiol network sample had a much lower measured resistance (7.6×10^5 Ω) compared to the nonanedithiol sample (1.4×10^8 Ω). The measured resistances of both samples lie close to 70% molecular contact within the network according to the spice circuit model (cf. Figure 3.28).

The effect of defects and/or contact resistance in the network can also be surmised in the control samples: The measured resistance of the control samples ranges from 10^6 to 10^9 Ω, while the calculated resistance assuming all neighboring particles connected with gold contact is around 10^4 Ω. If a certain percentage of neighboring particles are not connected at all, the conduction paths for electron transport would be reduced and thus increases the overall resistance. Further measurements are needed in order to accurately determine the resistance of the control samples. Similar behaviour is also observed in the hexanethiol sample of Figure 3.17 (a) and the octanethiol sample of Figure 3.17 (b). The highest calculated resistances (3.5×10^7 Ω for the hexanethiol sample and 8.8×10^7 Ω for the octanethiol sample) assuming 100% molecular contact of both samples are much lower than the measured values (2.5×10^{11} Ω and 3×10^{10} Ω, respectively). For both cases a possible explanation is the existence of network defects and, in particular, the difficulty for alkanethiol molecules to form low-resistance covalent bonds with gold at the end without a sulfur atom, which may also explain why we observe non-linear *I*-*V* curves for plain thiol networks much more often than dithiol networks.

3.6 Conclusion

Self-assembled gold particle networks were fabricated based on a solution-based method and linear current-voltage characteristics are commonly measured on the nanostructure networks, while nonlinear asymmetric *I-V* curves are also occasionally observed. The conducting properties of thiolated molecules was investigated through the analysis of the *I-V* data of the networks. Our method provides a practical way to fabricate gold nanoparticle-molecular networks, which make it possible to study and control molecular network electrical conductivity and dimensions. Such networks hold potential as elements (resistors, diodes, transistors, memory devices, etc.) in future molecular integrated circuits and the self-assembly method is believed to be a promising way for implementing molecular circuitry because of its capability to fabricate nanoscale structures in large numbers cheaply and easily.

A simplified model of sequential resistors in parallel provides an approximate way to associate the network conductivity to dimensions. Although estimation of the network's conductance from this model is consistent with the measured data to a certain extent, an LTspice circuit model takes the nanoparticle interconnections into consideration to give a more accurate estimation. Generally the measured resistance of the network lies within the estimated range, from which the percentage of molecular contacts in the network is estimated. However, there are still some weaknesses in the circuit model – To increase the accuracy of the circuit model, all these factors need to be taken into consideration and a more complicated model might be needed.

The experimental work in this chapter contributed to two conferences [40, 42] and a journal paper [45] is also in preparation..

Chapter 4 Conclusion and Future Work

4.1 Conclusion

4.1.1 Modeling of Molecular Networks

Semi-empirical simulations were performed on isolated benzenedithiol, Al_6 clusters, and several benzenedithiol-Al_6 cluster systems including 1 to 4-unit benzenedithiol-Al_6 cluster chains and Y-shape and H-shape networks as well as 1 to 4-unit dithiol molecule-Al_6 cluster chains built of hexanedithiol, octanedithiol and decanedithiol molecules for comparison. The relaxed geometries of benzenedithiol molecular chains and networks are twisted to certain extent compared to the linear orientations of the alkanedithiol –Al_6 cluster chains. The HOMO-LUMO gap of the benzenedithiol-Al_6 structures decreases several eV compared to the isolated molecule in our calculation accompanied with a decreasing trend of the HOMO-LUMO gap values versus the number of junction units. Besides the HOMO-LUMO gap, the HOMO energies increase versus chain length, while the LUMO energies decrease. Such behaviors are considered similar to the band structure of crystals, e.g., semiconductors. In the energy spectrums it can be seen that the HOMO energy of Al_6 cluster lies within the molecular HOMO-LUMO gap and the energy levels near the HOMO-LUMO gaps for the benzenedithiol-Al_6 chains are getting more closely packed as the chain length increases, which assembles the formation of conducting band. The spatial distributions of the molecular orbitals benzenedithiol-Al_6 structures are either well-delocalized or overlap with close energy levels near the HOMO-LUMO gap, which signifies high transmission probability through the molecular structure and corresponds to peaks in the density of states.

4.1.2 Self-Assembled Molecular Networks

We fabricated nanostructures consisting of thiolate molecules and colloidal gold nanoparticles whose dimensions and the number of molecules contained are between the size of simple gold nanoparticle oligomers and well-organized self-assembled mono or multi layers of gold particles. AFM images of several gold particle oligomers interconnected by thiol molecule confirms the effect of molecules as linkers between gold nanoparticles and the large aggregations formed of networked gold particles.

Linear *I-V* characteristics are commonly measured on samples made of different dithiol and thiol molecules and with different ratios of N_{mol}: $N_{particle}$, number of molecules versus number gold particles, while nonlinear asymmetric *I-V* curves are also observed occasionally. The conducting tip AFM measured two distinct resistance ranges of kΩ or MΩ indicating two types of connections between neighbouring gold particles. A simplified model of multiple sequential resistors in parallel is used to estimate the conductance of networks. To take neighbouring particle interconnections into consideration, the topology of the gold particle network is simplified into a circuit model consisting of interconnected linear resistors and is simulated using LTspice, which shows consistency with the measured data.

Such self-assembled networks are possible to be used to implement several passive and active circuit components, and some more complicated devices consisting of networked particles and molecule like nanocells, memristors, etc. (see below). The electrical

properties of the networks could be tuned by proper choice of molecules and precise control of network's geometry.

4.2 Future work

4.2.1 Modeling of Larger Networks and Density Functional Theory Calculations

Our semi-empirical simulating method can be applied to model larger structures such as the network shown in Figure 4.1. The network is constructed by connecting two branches of neighboring Y-branches and forms a ring-shaped network. This structure can be treated as a unit cell and be repeated to build larger networks. It would be interesting to study the electronic properties of such metal-molecular networks and how electrons transport through the whole structure by switching from one branch to another.

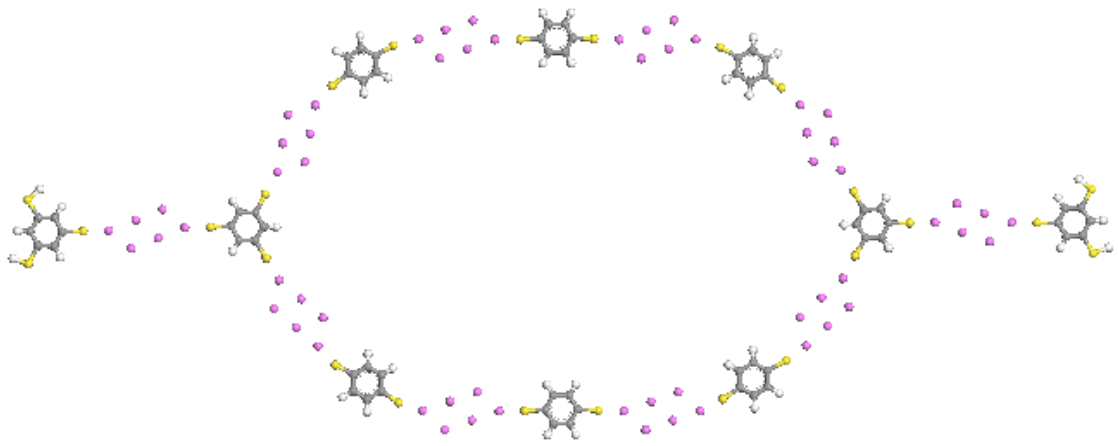

Figure 4.1 Ring-shaped network.

For the isolated dithiol molecules and Al clusters, DFT calculations can be re-performed for comparison with the results obtained with semi-empirical method. In addition, the

energy calculations can be done on the relaxed structures of benzenedithiol-Al_6 chains and networks obtained with VAMP to compare the electronic properties (orbital spatial distribution, density of states etc.).

DFT packages, such as Dmol, support Au atom, which can be used to do calculations on Au clusters and structures built from it. Then one set of dithiol molecule-Au cluster structures can be modeled as an analogous to our dithiol molecule-Al cluster calculations, which allows to investigate the bonding property between dithiol molecules and metallic clusters in depth.

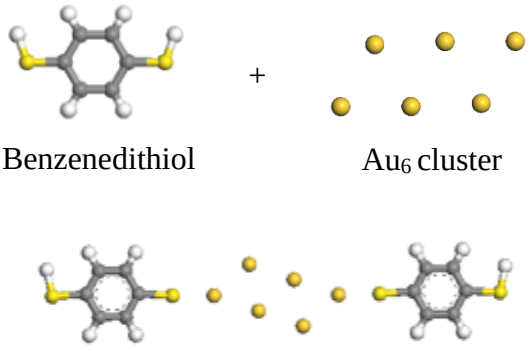

Figure 4.2 Schematic of Au cluster and benzenedithiol-Au cluster junction.

4.2.2 Self-assembled Gold Nanoparticle Networks with Other Thiolate Molecules and Ratios

The work of fabricating self-assembled gold nanoparticle networks can be extended by tuning the N_{mol}: $N_{particle}$ ratios and adopting other dithiolate molecules and metal clusters. By using different N_{mol}: $N_{particle}$ ratios, different conductivity properties should be measured and a transition in the topology of the fabricated nanostructures may be

observed. Besides, with more data, the interconnecting topology within the network can be investigated in more details.

The use of other alkanedithiol molecules with different lengths can help in the study of exponential relation between the molecule's conductance and length. The alkanedithiol molecules can range from ethanedithiol with two methylene units to hexadecanedithiol with sixteen methylene units. Besides, aromatic molecules such as benzenedithiol and biphenyldithiol can also be adapted in the fabrication of self-assembled gold particle network, which would be interesting to compare the conductivity property between saturated alkanedithiol molecules and conjugated aromatic molecules.

Another topic that is worth studying is a third type of network connection where two particles are bridged by two tangled molecules, as illustrated in Figure 4.3. Charge transport through this type of connection is complicated and this may be an explanation to the measured nonlinear asymmetric *I*-*V* characteristics presented in Chapter 3.

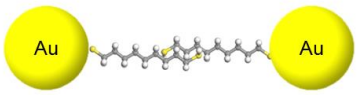

Figure 4.3 Two particles connected by loosely-packed molecules.

The influence of the metallic particles is also worth investigation. The colloidal gold nanoparticles with different sizes, from smaller than 10 nm to over 100 nm in diameter, can used in the synthesis of self-assembled metal-molecular networks. Furthermore, gold

particles of different sizes can also be adapted in the process to fabricate the ”inhomogeneous” structures. Besides gold, dithiol molecules can also form covalent bond with other metals such as Ag, Cu, Pt etc [84, 87]. Thus, using other types of metallic particles in the fabrication is another interesting topic as an extension of this study.

The LTSpice modeling can be improved by using bigger unit cell to provide more variables for generating more accurate plots of resistance versus percentage of molecular contact. Also, the effect of defects should be taken into consideration in circuit modeling, i.e. assign certain variables with extremely high resistance, to achieve more precise simulation.

At last, to test the predicted properties of the benzenedithiol molecular chains and networks from our semi-empirical simulations, there are several methods applicable. Firstly, hopping conduction is the most likely conduction mechanism for molecular linear chains due to their relatively larger length. So the conduction barrier height, which is HOMO-LUMO gap approximately, can be tested by studying the temperature dependent characteristic of the linear chains (see Chapter 1). Secondly, it is possible to use STM/AFM to probe the density of states of the molecular chains and networks to test if the DOS peaks exist around HOMO-LUMO gap as predicted. Finally, optically checking the adsorption of the HOMO-LUMO gap is another method to test the validity of our semi-empirical modeling.

4.2.3 Device Applications

Understanding current flow through molecule stimulates the applications of molecules as basic circuit components. There are attempts at tuning molecule's conductance by increasing the length of saturated molecules in order to provide a set of molecular resistors [34, 37]. Several molecules are measured with significant signal rectification character very similar to semiconductor diodes and therefore can be used as molecular diodes [114]. Experiments involving a few three-terminal gated molecules have demonstrated gate modulation of the molecular *I-V* characteristics, which indicates the possibility of using molecules as electronic transistors [115]. By using molecules as basic components in the circuit, completely novel devices are fabricated and, specifically, our fabrication method of self-assembled gold nanoparticle networks finds applications in several types of nanoscale devices in the use of computing, memory and security purpose.

Our in-solution fabrication method is suitable for building the nanocell device, which is a type of molecular computing component defined as an organization of molecules and metal clusters designed to assemble a programmable electronic device. Within a nanocell, molecules with specific features are interconnected with metallic clusters, as presented in Figure 4.4. The yellow contacts are addressed externally using lithographic technique and are used to program the behaviour of the molecules and clusters in the nanocell. The programming on a nanocell is done by applying high or low bias voltage on the nanocell's contacts until it functions as target logic device. Several simulations and experiment works have proved that nanocell can be programmed to work with functions

as memory and logic gates [116, 117] so, by choosing well-featured molecules and properly functionality programming, the nanocell built of the network of the dithiol molecules and gold particles is possible to be designed with certain computing functionality.

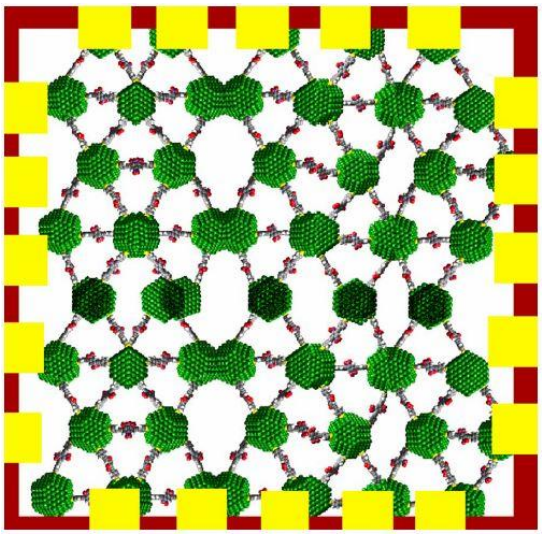

Figure 4.4 Schematic of a nanocell consisting of metallic clusters and molecules (adapted from Ref. 118).

Another type of application for our self-assembled dithiol molecule-metallic particle networks is the memristor devices. Memristors are viewed as two-terminal resistors whose internal resistance state can be modified according to the history of applied voltage or current and their dynamical nonlinear switching characteristic in resistance suggests several computational applications [119, 120]. Thus, using memristors as computational elements, memristive devices are essentially electrical resistance switches retaining a resistance state decided externally by design. One straightforward implementation of our metal-molecular nanonetworks into memristor devices is the crossbar architecture, which is shown in Figure 4.5. By choosing molecules and metallic

particles with proper features, it is possible to fabricate certain nanostructrures with memristor's electrical characteristic. Structures are injected at the crosspoint in the crossbar array and by applying proper voltage bias on the wires the resistance state of the crosspoint can be switched ON or OFF as wanted. Furthermore, combined with conventional CMOS techniques, the memristor crossbar array can be implemented into circuits as memory and logic computing units.

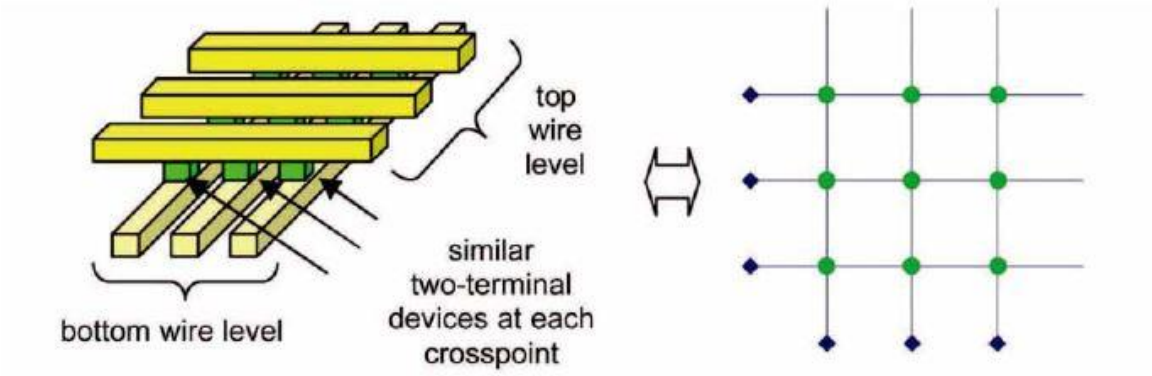

Figure 4.5 Single crossbar memristor array and its equivalent circuit representation (adapted from Ref. 121).

The third type of application is for building cryptographic primitives for information security. Ref. 122 introduces a synthesis process based self-assembled nanotubes to fabricate the unclonable cryptographic primitives. The carbon nanotubes are deposited onto the trenches on the substrate. By careful design of the trench width, the nanotubes are connected with the highest random rate and thus a random binary bit array is fabricated for generating encryption keys. The carbon nanotube can be replaced by our self-assembled particle network. Since the network is formed naturally, random connection could be achieved in the bits array. The exact structure of the bits array might

be different from Ref. 122 but similar ability of generating encryption keys can be obtained.

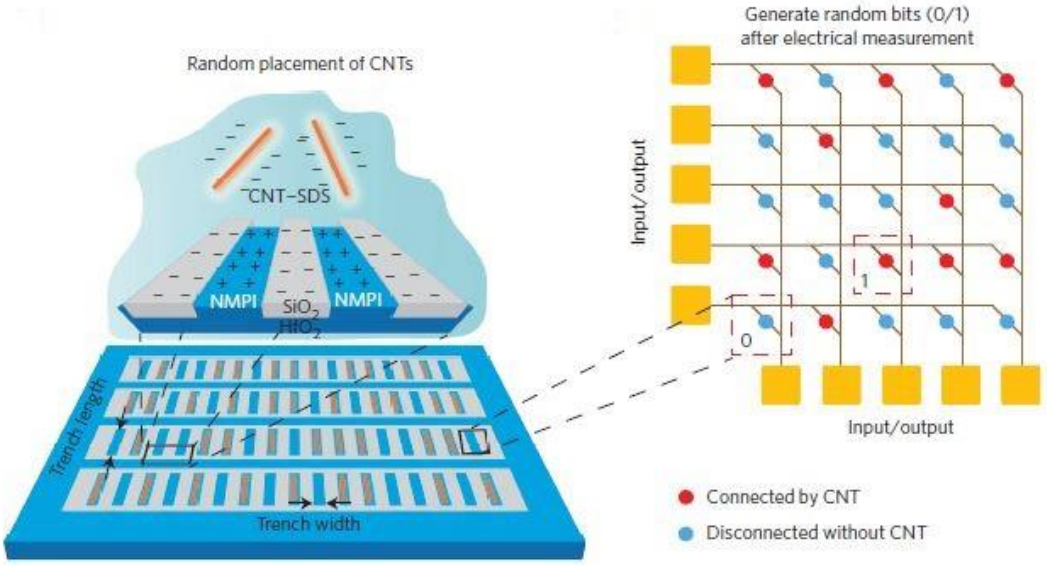

Figure 4.6 Random bits generator based on 2D carbon nanotube array (adapted from Ref. 122).

Finally, the metal-molecular nanoparticle networks could be used as sensors. The principle is straightforward: since the electrical characteristic of the network is well-defined, any factors that affect the property of the linker dithiol molecules can be observed through monitoring the network's electrical characteristic. Sensor devices based on this principle is discussed in Ref. 123 , which is based on negative differential resistance devices, and Ref. 124, which uses nonanedithiol for detection of Cd^{+2} ions.

Bibliography

[1] T. K. Kiong, L. T. Heng, D. Huifang, and H. Sunan, "Overview of Nanotechnology," in *Precision Motion Control*, Springer, 2001, pp. 1–11.

[2] S. Lindsay, *Introduction to nanoscience*. Oxford University Press, 2009.

[3] G. Binnig, H. Rohrer, C. Gerber, and E. Weibel, "Tunneling through a controllable vacuum gap," *Applied Physics Letters*, vol. 40, no. 2, pp. 178–180, 1982.

[4] G. Binnig, C. F. Quate, and C. Gerber, "Atomic force microscope," *Physical review letters*, vol. 56, no. 9, p. 930, 1986.

[5] M. D. Levenson, N. Viswanathan, and R. A. Simpson, "Improving resolution in photolithography with a phase-shifting mask," *IEEE Transactions on electron devices*, vol. 29, no. 12, pp. 1828–1836, 1982.

[6] R. G. Nuzzo and D. L. Allara, "Adsorption of bifunctional organic disulfides on gold surfaces," *Journal of the American Chemical Society*, vol. 105, no. 13, pp. 4481–4483, 1983.

[7] W. Lu, P. Xie, and C. M. Lieber, "Nanowire transistor performance limits and applications," *IEEE transactions on Electron Devices*, vol. 55, no. 11, pp. 2859–2876, 2008.

[8] Cb. Murray, D. J. Norris, and M. G. Bawendi, "Synthesis and characterization of nearly monodisperse CdE (E= sulfur, selenium, tellurium) semiconductor nanocrystallites," *Journal of the American Chemical Society*, vol. 115, no. 19, pp. 8706–8715, 1993.

[9] N. C. Seeman, "Nucleic acid junctions and lattices," *Journal of theoretical biology*, vol. 99, no. 2, pp. 237–247, 1982.

[10] J. Bardeen and W. H. Brattain, "The transistor, a semi-conductor triode," *Physical Review*, vol. 74, no. 2, p. 230, 1948.

[11] J. S. Kilby, "Invention of the integrated circuit," *IEEE Transactions on electron devices*, vol. 23, no. 7, pp. 648–654, 1976.

[12] R. N. Noyce, "Semiconductor device-and-lead structure." Google Patents, 1961.

[13] D. Kahng and M. Atalla, "Silicon-silicon dioxide field induced surface devices," in *IRE Solid-State Device Research Conference*, 1960.

[14] G. E. Moore, "Cramming more components onto integrated circuits, Reprinted from Electronics, volume 38, number 8, April 19, 1965, pp. 114 ff.," *IEEE Solid-State Circuits Newsletter*, vol. 3, no. 20, pp. 33–35, 2006.

[15] G. E. Moore and others, "Progress in digital integrated electronics," in *Electron Devices Meeting*, 1975, vol. 21, pp. 11–13.

[16] S. E. Thompson and S. Parthasarathy, "Moore's law: the future of Si microelectronics," *materials today*, vol. 9, no. 6, pp. 20–25, 2006.

[17] C. Y. Chang and others, *ULSI devices*. John Wiley & Sons, 2000.

[18] Y. Taur, D. A. Buchanan, W. Chen, D. J. Frank, K. E. Ismail, S.-H. Lo, G. A. Sai-Halasz, R. G. Viswanathan, H.-J. C. Wann, S. J. Wind, and others, "CMOS scaling into the nanometer regime," *Proceedings of the IEEE*, vol. 85, no. 4, pp. 486–504, 1997.

[19] D. J. Frank, R. H. Dennard, E. Nowak, P. M. Solomon, Y. Taur, and H.-S. P. Wong, "Device scaling limits of Si MOSFETs and their application dependencies," *Proceedings of the IEEE*, vol. 89, no. 3, pp. 259–288, 2001.
[20] J. Randall and others, "Resonant tunneling devices and logic circuits: Lateral tunneling devices," *unpublished briefing, Texas Instruments Corp., Dallas, TX*, 1995.
[21] U. Meirav and E. Foxman, "Single-electron phenomena in semiconductors," *Semiconductor Science and Technology*, vol. 11, no. 3, p. 255, 1996.
[22] J. Welser, S. Tiwari, S. Rishton, K. Lee, and Y. Lee, "Room temperature operation of a quantum-dot flash memory," *IEEE Electron Device Letters*, vol. 18, no. 6, pp. 278–280, 1997.
[23] L. Zhuang, L. Guo, and S. Y. Chou, "Silicon single-electron quantum-dot transistor switch operating at room temperature," *Applied Physics Letters*, vol. 72, no. 10, pp. 1205–1207, 1998.
[24] R. S. Mulliken, "Intensities of Electronic Transitions in Molecular Spectra II. Charge-Transfer Spectra," *The Journal of Chemical Physics*, vol. 7, no. 1, pp. 20–34, 1939.
[25] A. Aviram and M. A. Ratner, "Molecular rectifiers," *Chemical Physics Letters*, vol. 29, no. 2, pp. 277–283, 1974.
[26] J. McGinness, P. Corry, and P. Proctor, "Amorphous semiconductor switching in melanins," *Science*, vol. 183, no. 4127, pp. 853–855, 1974.
[27] J. Chen, M. Reed, A. Rawlett, and J. Tour, "Large on-off ratios and negative differential resistance in a molecular electronic device," *Science*, vol. 286, no. 5444, pp. 1550–1552, 1999.
[28] F. L. Carter, "The molecular device computer: point of departure for large scale cellular automata," *Physica D: Nonlinear Phenomena*, vol. 10, no. 1–2, pp. 175–194, 1984.
[29] F. L. Carter, "Moleculor Electronic Devices," 1983.
[30] R. Landauer, "Spatial variation of currents and fields due to localized scatterers in metallic conduction," *IBM Journal of Research and Development*, vol. 1, no. 3, pp. 223–231, 1957.
[31] M. Galperin, M. A. Ratner, and A. Nitzan, "Molecular transport junctions: vibrational effects," *Journal of Physics: Condensed Matter*, vol. 19, no. 10, p. 103201, 2007.
[32] W. Wang, T. Lee, and M. A. Reed, "Mechanism of electron conduction in self-assembled alkanethiol monolayer devices," *Physical Review B*, vol. 68, no. 3, p. 035416, 2003.
[33] N. Tao, "Electron transport in molecular junctions," *Nature nanotechnology*, vol. 1, no. 3, pp. 173–181, 2006.
[34] V. B. Engelkes, J. M. Beebe, and C. D. Frisbie, "Length-dependent transport in molecular junctions based on SAMs of alkanethiols and alkanedithiols: effect of metal work function and applied bias on tunneling efficiency and contact resistance," *Journal of the American Chemical Society*, vol. 126, no. 43, pp. 14287–14296, 2004.
[35] P. Wohlfart, J. Weiβ, J. Käshammer, C. Winter, V. Scheumann, R. A. Fischer, and S. Mittler-Neher, "Selective ultrathin gold deposition by organometallic chemical

vapor deposition onto organic self-assembled monolayers (SAMs)," *Thin Solid Films*, vol. 340, no. 1, pp. 274–279, 1999.

[36] M. A. Reed, C. Zhou, M. Deshpande, C. Muller, T. Burgin, L. Jones, and J. M. Tour, "The electrical measurement of molecular junctions," *Annals of the New York Academy of Sciences*, vol. 852, no. 1, pp. 133–144, 1998.

[37] S. Kober, G. Gotesman, and R. Naaman, "Surprising Molecular Length Dependence in Conduction through a Hybrid Organic–Inorganic System," *The journal of physical chemistry letters*, vol. 4, no. 12, pp. 2041–2045, 2013.

[38] T. Dadosh, Y. Gordin, R. Krahne, I. Khivrich, D. Mahalu, V. Frydman, J. Sperling, A. Yacoby, and I. Bar-Joseph, "Measurement of the conductance of single conjugated molecules," *Nature*, vol. 436, no. 7051, pp. 677–680, 2005.

[39] Y. Vardi, A. Guttman, and I. Bar-Joseph, "Random Telegraph Signal in a Metallic Double-Dot System," *Nano letters*, vol. 14, no. 5, pp. 2794–2799, 2014.

[40] P. Zhang and C. Papadopoulos, "Electronic transport in self-assembled gold nanoparticle-molecular networks," in *2016 American Chemical Society Spring Meeting*, 2016.

[41] P. Zhang and C. Papadopoulos, "Electronic properties of metal-molecular nanojunctions and networks," in *IEEE Nanotechnology Materials and Devices Conference (NMDC)*, 2015.

[42] P. Zhang and C. Papadopoulos, "Self-assembly of gold nanoparticle-molecular networks," in *2015 International Conference & Exhibition on Advanced & Nano Materials*, 2015.

[43] P. Zhang and C. Papadopoulos, "Electronic Properties of Metal-molecular Junctions and Network," in *2014 Pacific Center for Advanced Materials and Microstructures Annual Meeting*, 2014.

[44] P. Zhang and C. Papadopoulos, "Electronic properties of metal-molecular nanojunctions and networks," in *2015 IEEE Nanotechnology Materials and Devices Conference (NMDC)*, 2015, pp. 1–5.

[45] A. Venkataraman, P. Zhang, and C. Papadopoulos, "Electronic transport in self-assembled gold nanoparticle-molecular networks.", in preparation.

[46] P. Zhang and C. Papadopoulos, "Metal-Molecular Network as Nanoelectronics Switching Elements and Circuits.", in preparation.

[47] W. Kolos and L. Wolniewicz, "Accurate adiabatic treatment of the ground state of the hydrogen molecule," *Journal of Chemical Physics*, vol. 41, pp. 3663–3673, 1964.

[48] B. Sutcliffe, "The decoupling of electronic and nuclear motions in the isolated molecule Schrodinger Hamiltonian," *Advances in Chemical Physics*, vol. 114, pp. 1–122, 2000.

[49] D. J. Griffiths, *Introduction to quantum mechanics*. Pearson Education India, 2005.

[50] C. F. Fischer, "General hartree-fock program," *Computer physics communications*, vol. 43, no. 3, pp. 355–365, 1987.

[51] J. Pople and R. Nesbet, "Self-consistent orbitals for radicals," *The Journal of Chemical Physics*, vol. 22, no. 3, pp. 571–572, 1954.

[52] P. Hohenberg and W. Kohn, "Inhomogeneous electron gas," *Physical review*, vol. 136, no. 3B, p. B864, 1964.

[53] W. Kohn and L. J. Sham, “Self-consistent equations including exchange and correlation effects,” *Physical review*, vol. 140, no. 4A, p. A1133, 1965.
[54] A. D. Becke, “Perspective: Fifty years of density-functional theory in chemical physics,” *The Journal of chemical physics*, vol. 140, no. 18, p. 18A301, 2014.
[55] J. P. Perdew, J. Chevary, S. Vosko, K. A. Jackson, M. R. Pederson, D. Singh, and C. Fiolhais, “Atoms, molecules, solids, and surfaces: Applications of the generalized gradient approximation for exchange and correlation,” *Physical Review B*, vol. 46, no. 11, p. 6671, 1992.
[56] F. Jensen, *Introduction to computational chemistry*. John Wiley & Sons, 2013.
[57] M. C. Zerner, “Semiempirical molecular orbital methods,” *Reviews in computational chemistry*, vol. 2, pp. 313–365, 1991.
[58] M. J. Dewar and W. Thiel, “Ground states of molecules. 38. The MNDO method. Approximations and parameters,” *Journal of the American Chemical Society*, vol. 99, no. 15, pp. 4899–4907, 1977.
[59] M. J. Dewar, E. G. Zoebisch, E. F. Healy, and J. J. Stewart, “Development and use of quantum mechanical molecular models. 76. AM1: a new general purpose quantum mechanical molecular model,” *Journal of the American Chemical Society*, vol. 107, no. 13, pp. 3902–3909, 1985.
[60] J. J. Stewart, “Semiempirical molecular orbital methods,” *Reviews in computational chemistry*, vol. 1, pp. 45–81, 1990.
[61] J. J. Stewart and P. von R. Schleyer, “Encyclopedia of computational chemistry,” *In Encyclopedia of Computational Chemistry*, vol. 4, 1998.
[62] J. J. Stewart, “Comparison of the accuracy of semiempirical and some DFT methods for predicting heats of formation,” *Journal of molecular modeling*, vol. 10, no. 1, pp. 6–12, 2004.
[63] P. Winget, A. H. Horn, C. Selçuki, B. Martin, and T. Clark, “AM1* parameters for phosphorus, sulfur and chlorine,” *Journal of molecular modeling*, vol. 9, no. 6, pp. 408–414, 2003.
[64] M. J. Dewar, C. Jie, and J. Yu, “SAM1; the first of a new series of general purpose quantum mechanical molecular models,” *Tetrahedron*, vol. 49, no. 23, pp. 5003–5038, 1993.
[65] Z. Ning, J. Chen, S. Hou, J. Zhang, Z. Liang, J. Zhang, and R. Han, “First-principles calculation of the transport properties of molecular wires between Au clusters under equilibrium,” *Physical Review B*, vol. 72, no. 15, p. 155403, 2005.
[66] W. Tian, S. Datta, S. Hong, R. Reifenberger, J. I. Henderson, and C. P. Kubiak, “Conductance spectra of molecular wires,” *The Journal of chemical physics*, vol. 109, no. 7, pp. 2874–2882, 1998.
[67] P. A. Derosa and J. M. Seminario, “Electron transport through single molecules: Scattering treatment using density functional and green function theories,” *The Journal of Physical Chemistry B*, vol. 105, no. 2, pp. 471–481, 2001.
[68] K. Stokbro, J. Taylor, M. Brandbyge, J.-L. Mozos, and P. Ordejon, “Theoretical study of the nonlinear conductance of Di-thiol benzene coupled to Au (111) surfaces via thiol and thiolate bonds,” *Computational Materials Science*, vol. 27, no. 1, pp. 151–160, 2003.
[69] K. S. Thygesen and K. W. Jacobsen, “Molecular transport calculations with Wannier functions,” *Chemical Physics*, vol. 319, no. 1, pp. 111–125, 2005.

[70] Y. Xue, S. Datta, and M. A. Ratner, “Charge transfer and ‘band lineup’ in molecular electronic devices: A chemical and numerical interpretation,” *The Journal of Chemical Physics*, vol. 115, no. 9, pp. 4292–4299, 2001.

[71] Y. Xue and M. A. Ratner, “End group effect on electrical transport through individual molecules: A microscopic study,” *Physical Review B*, vol. 69, no. 8, p. 085403, 2004.

[72] R. Jones, “Simulated annealing study of neutral and charged clusters: Aln and Gan,” *The Journal of chemical physics*, vol. 99, no. 2, pp. 1194–1206, 1993.

[73] T. Upton, “A perturbed electron droplet model for the electronic structure of small aluminum clusters,” *The Journal of chemical physics*, vol. 86, no. 12, pp. 7054–7064, 1987.

[74] S. H. Yang, D. A. Drabold, J. B. Adams, and A. Sachdev, “First-principles local-orbital density-functional study of Al clusters,” *Physical Review B*, vol. 47, no. 3, p. 1567, 1993.

[75] M. Ishitsuka, T. Hiaki, and N. Osaka, “Coadsorption self-assembled monolayers of trithiocyanuric acid and 1, 3, 5-benzenetrithiol on an evaporated silver film,” *Journal of Molecular Structure*, vol. 1002, no. 1, pp. 179–186, 2011.

[76] M. J. Dewar and D. M. Storch, “Development and use of quantum molecular models. 75. Comparative tests of theoretical procedures for studying chemical reactions,” *Journal of the American Chemical Society*, vol. 107, no. 13, pp. 3898–3902, 1985.

[77] J. J. Stewart, “Optimization of parameters for semiempirical methods IV: extension of MNDO, AM1, and PM3 to more main group elements,” *Journal of Molecular Modeling*, vol. 10, no. 2, pp. 155–164, 2004.

[78] P. Winget and T. Clark, “AM1* parameters for aluminum, silicon, titanium and zirconium,” *Journal of molecular modeling*, vol. 11, no. 6, pp. 439–456, 2005.

[79] J. J. Stewart, “Optimization of parameters for semiempirical methods. III Extension of PM3 to Be, Mg, Zn, Ga, Ge, As, Se, Cd, In, Sn, Sb, Te, Hg, Tl, Pb, and Bi,” *Journal of computational chemistry*, vol. 12, no. 3, pp. 320–341, 1991.

[80] J. J. Stewart, “Optimization of parameters for semiempirical methods II. Applications,” *Journal of Computational Chemistry*, vol. 10, no. 2, pp. 221–264, 1989.

[81] M. Guerra, G. Distefano, D. Jones, F. P. Colonna, and A. Modelli, “An MS Xα and ETS study of the influence of ‘d’ orbitals on the electron affinities of thio-substituted benzenes,” *Chemical physics*, vol. 91, no. 3, pp. 383–390, 1984.

[82] A. Scheer, G. Gallup, and P. Burrow, “Unoccupied orbital energies of 1, 4-benzenedithiol and the HOMO–LUMO gap,” *Chemical Physics Letters*, vol. 466, no. 4, pp. 131–135, 2008.

[83] H. C. Nguyen, B. M. Szyja, and N. L. Doltsinis, “Electric conductance of a mechanically strained molecular junction from first principles: Crucial role of structural relaxation and conformation sampling,” *Physical Review B*, vol. 90, no. 11, p. 115440, 2014.

[84] F. Bussolotti, M. G. Betti, and C. Mariani, “Anchoring methane thiol on Cu (100) in different structural configurations: Electronic state dispersion,” *Physical Review B*, vol. 74, no. 12, p. 125422, 2006.

[85] P. J. Feibelman, “Sulfur adsorption near a step on Al,” *Physical Review B*, vol. 49, no. 20, p. 14632, 1994.

[86] K. Jacobi, C. Muschwitz, and K. Kambe, “Angle-resolved UV photoemission studies of the two-dimensional band structures of sulfur, selenium, and tellurium monolayers adsorbed on aluminium (111),” *Surface Science*, vol. 93, no. 1, pp. 310–326, 1980.

[87] B. Kim, S. H. Choi, X.-Y. Zhu, and C. D. Frisbie, “Molecular tunnel junctions based on π-conjugated oligoacene Thiols and Dithiols between Ag, Au, and Pt contacts: Effect of surface linking group and metal work function,” *Journal of the American Chemical Society*, vol. 133, no. 49, pp. 19864–19877, 2011.

[88] W. Shen and G. Nyberg, “The adsorption and bonding of methanethiol on aluminium,” *Surface science*, vol. 296, no. 1, pp. 49–56, 1993.

[89] C. J. Carmalt, J. D. Mileham, A. J. White, D. J. Williams, and S. Rushworth, “Synthetic and structural studies on aluminium thiolate complexes,” *Polyhedron*, vol. 22, no. 18, pp. 2655–2660, 2003.

[90] F. Lips, J. C. Fettinger, and P. P. Power, “Synthesis and characterization of sterically encumbered aluminum thiolato complexes with rare Al/S/halide structural motifs,” *Polyhedron*, vol. 79, pp. 207–212, 2014.

[91] R. Manne and T. Åberg, “Koopmans’ theorem for inner-shell ionization,” *Chemical Physics Letters*, vol. 7, no. 2, pp. 282–284, 1970.

[92] W. Richards, “The use of Koopmans’ Theorem in the interpretation of photoelectron spectra,” *International Journal of Mass Spectrometry and Ion Physics*, vol. 2, no. 6, pp. 419–424, 1969.

[93] P. Burrow and A. Modelli, “On the treatment of LUMO energies for their use as descriptors,” *SAR and QSAR in Environmental Research*, vol. 24, no. 8, pp. 647–659, 2013.

[94] N. Heinrich, W. Koch, and G. Frenking, “On the use of Koopmans’ theorem to estimate negative electron affinities,” *Chemical physics letters*, vol. 124, no. 1, pp. 20–25, 1986.

[95] J. M. Younkin, L. J. Smith, and R. N. Compton, “Semi-empirical calculations of π-electron affinities for some conjugated organic molecules,” *Theoretica chimica acta*, vol. 41, no. 2, pp. 157–176, 1976.

[96] J. M. Seminario, A. G. Zacarias, and J. M. Tour, “Theoretical study of a molecular resonant tunneling diode,” *Journal of the American Chemical Society*, vol. 122, no. 13, pp. 3015–3020, 2000.

[97] J. M. Seminario and L. Yan, “Ab initio analysis of electron currents in thioalkanes,” *International journal of quantum chemistry*, vol. 102, no. 5, pp. 711–723, 2005.

[98] Y.-T. Tao, C.-C. Wu, J.-Y. Eu, W.-L. Lin, K.-C. Wu, and C. Chen, “Structure evolution of aromatic-derivatized thiol monolayers on evaporated gold,” *Langmuir*, vol. 13, no. 15, pp. 4018–4023, 1997.

[99] X. Cui, X. Zarate, J. Tomfohr, O. Sankey, A. Primak, A. L. Moore, T. A. Moore, D. Gust, G. Harris, and S. Lindsay, “Making electrical contacts to molecular monolayers,” *Nanotechnology*, vol. 13, no. 1, p. 5, 2001.

[100] R. Hoft, J. Liu, M. Cortie, and M. Ford, “Electron tunneling through alkanedithiol molecules,” in *Microelectronics, MEMS, and Nanotechnology*, 2005, pp. 603603–603603.

[101] R. Waser, *Nanoelectronics and information technology*. John Wiley & Sons, 2012.

[102] T. Palm, “Self-consistent calculations of an electron-wave Y-branch switch,” *Journal of applied physics*, vol. 74, no. 5, pp. 3551–3557, 1993.

[103] J.-O. J. Wesström, “Self-gating effect in the electron Y-branch switch,” *Physical Review Letters*, vol. 82, no. 12, p. 2564, 1999.

[104] T. Palm and L. Thylen, “Designing logic functions using an electron waveguide Y-branch switch,” *Journal of applied physics*, vol. 79, no. 10, pp. 8076–8081, 1996.

[105] S. Reitzenstein, D. Hartmann, M. Kamp, and L. Worschech, “Sub-kT Switching in Asymmetric Y-Transistors With Internal Feedback Coupling,” *IEEE Journal of the Electron Devices Society*, vol. 3, no. 3, pp. 158–163, 2015.

[106] D. Bethell, M. Brust, D. Schiffrin, and C. Kiely, “From monolayers to nanostructured materials: an organic chemist’s view of self-assembly,” *Journal of Electroanalytical Chemistry*, vol. 409, no. 1, pp. 137–143, 1996.

[107] D. Loss and D. P. DiVincenzo, “Quantum computation with quantum dots,” *Physical Review A*, vol. 57, no. 1, p. 120, 1998.

[108] C. Chu, J.-S. Na, and G. N. Parsons, “Conductivity in alkylamine/gold and alkanethiol/gold molecular junctions measured in molecule/nanoparticle/molecule bridges and conducting probe structures,” *Journal of the American Chemical Society*, vol. 129, no. 8, pp. 2287–2296, 2007.

[109] C.-C. Kaun and H. Guo, “Resistance of alkanethiol molecular wires,” *Nano letters*, vol. 3, no. 11, pp. 1521–1525, 2003.

[110] C. Bruot, J. Hihath, and N. Tao, “Mechanically controlled molecular orbital alignment in single molecule junctions,” *Nature nanotechnology*, vol. 7, no. 1, pp. 35–40, 2012.

[111] D. Kockmann, B. Poelsema, and H. J. Zandvliet, “Transport through a single octanethiol molecule,” *Nano letters*, vol. 9, no. 3, pp. 1147–1151, 2009.

[112] B. Xu and N. J. Tao, “Measurement of single-molecule resistance by repeated formation of molecular junctions,” *Science*, vol. 301, no. 5637, pp. 1221–1223, 2003.

[113] P. S. Yoo, H. Y. Jo, and T. Kim, “Temperature Dependence of Conductance and Plateau Length for Single-Molecule Junctions Formed with Silver Electrodes,” *The Journal of Physical Chemistry C*, vol. 118, no. 51, pp. 29962–29965, 2014.

[114] I. Dıez-Pérez, J. Hihath, Y. Lee, L. Yu, L. Adamska, M. A. Kozhushner, I. I. Oleynik, and N. Tao, “Rectification and stability of a single molecular diode with controlled orientation,” *Nature chemistry*, vol. 1, no. 8, pp. 635–641, 2009.

[115] A. W. Ghosh, T. Rakshit, and S. Datta, “Gating of a molecular transistor: Electrostatic and conformational,” *Nano Letters*, vol. 4, no. 4, pp. 565–568, 2004.

[116] J. M. Tour, L. Cheng, D. P. Nackashi, Y. Yao, A. K. Flatt, S. K. St. Angelo, T. E. Mallouk, and P. D. Franzon, “Nanocell electronic memories,” *Journal of the American Chemical Society*, vol. 125, no. 43, pp. 13279–13283, 2003.

[117] J. M. Tour, W. L. Van Zandt, C. P. Husband, S. M. Husband, L. S. Wilson, P. D. Franzon, and D. P. Nackashi, "Nanocell logic gates for molecular computing," *IEEE transactions on Nanotechnology*, vol. 1, no. 2, pp. 100–109, 2002.

[118] J. M. Seminario, Y. Ma, and V. Tarigopula, "The nanocell: A chemically assembled molecular electronic circuit," *IEEE Sensors Journal*, vol. 6, no. 6, pp. 1614–1626, 2006.

[119] Y. V. Pershin and M. Di Ventra, "Memory effects in complex materials and nanoscale systems," *Advances in Physics*, vol. 60, no. 2, pp. 145–227, 2011.

[120] J. J. Yang, D. B. Strukov, and D. R. Stewart, "Memristive devices for computing," *Nature nanotechnology*, vol. 8, no. 1, pp. 13–24, 2013.

[121] D. B. Strukov and R. S. Williams, "Four-dimensional address topology for circuits with stacked multilayer crossbar arrays," *Proceedings of the National Academy of Sciences*, vol. 106, no. 48, pp. 20155–20158, 2009.

[122] Z. Hu, J. M. M. L. Comeras, H. Park, J. Tang, A. Afzali, G. S. Tulevski, J. B. Hannon, M. Liehr, and S.-J. Han, "Physically unclonable cryptographic primitives using self-assembled carbon nanotubes," *Nature nanotechnology*, vol. 11, no. 6, pp. 559–565, 2016.

[123] A. J. Gimenez, G. Luna-Barcenas, and J. M. Seminario, "Analysis of nano and molecular arrays of negative differential resistance devices for sensing and electronics," *IEEE Sensors Journal*, vol. 9, no. 9, pp. 1136–1141, 2009.

[124] E. Malel, J. K. Sinha, I. Zawisza, G. Wittstock, and D. Mandler, "Electrochemical detection of Cd 2+ ions by a self-assembled monolayer of 1, 9-nonanedithiol on gold," *Electrochimica Acta*, vol. 53, no. 23, pp. 6753–6758, 2008.

Appendix A

Matlab Code for Plotting Energy Level Spectrum

```
figure;

plot([0 1],[energyLevelsOfBenzenedithiol; energyLevelsOfBenzenedithiol
],'k',[2 3],[energyLevelsOfAlCluster; energyLevelsOfAlCluster],'k',[4
5],[energyLevelsOfJunction; energyLevelsOfJunction],'k')

ylabel('energy/eV')
title('benzenedithiol         Al cluster        dithiolbenzene
junction')
```

Appendix B

Matlab Code for Calculating Density of States

```
ene=[energyLevelsOfJunction];
preden=gradient(ene);
den=preden.^-1;
figure;
plot(ene,den,[0],[250]);

title('dithiolbenzene 1-unit chain')
xlabel('Energy/eV')
ylabel('Density of states')
%dithiolbenzene junction
```

Appendix C

Python code for preprocessing Dmol output data

```
import sys

def main():
        path = r"FilePathofOutputData"
        str = path.split('\\')
        target = path.replace(str[-1], 'target.txt')
        file = open(path, 'rU')
        targetFile = open(target, 'w')
        lastValue = 0
        for line in file:
                cont = line.split()
                value = float(cont[5])
                if value >= -15 and value <= 0:
                        if value != lastValue:
                                targetFile.write(cont[5])
                                targetFile.write(' ')
                        lastValue = value
        print "target file created."
        file.close()
        sys.exit()

if __name__ == '__main__':
    main()
```

Appendix D

Python code for generating random set of resistance variables (random variable generator)

```
import sys
import random

def main():
        i = 1
        while(i<=18):
                nums = [1, 2, 3, 4, 5, 6, 7, 8, 9, 10, 11, 12, 13, 14, 15, 16, 17, 18, 19, 20,
                21, 22, 23, 24, 25, 26, 27, 28, 29, 30, 31, 32, 33, 34, 35, 36]
                random.shuffle(nums)
                 j = 0
                print "random varialbes: " + str(18-i) + ":" + str(i) + " =============="
                var = " "
                cho = range(i*2)
                while(j<=(i*2-1)):
                        cho[j] = nums[j]
                         j=j+1
                        cho.sort()
                 j=0
                 while(j<=(i*2-1)):
                         var = var + str(cho[j]) + " "
                        j=j+1
                print var
                print "\n"
                i=i+1
    sys.exit()

if __name__ == '__main__':
main()
```